

Russian Original Vol. 56, No. 3, March, 1984

September, 1984

SATEAZ 56(3) 133-206 (1984)

SOVIET ATOMIC ENERGY

АТОМНАЯ ЭНЕРГИЯ
(ATOMNAYA ÉNERGIYA)

TRANSLATED FROM RUSSIAN



CONSULTANTS BUREAU, NEW YORK

SOVIET ATOMIC ENERGY

Soviet Atomic Energy is abstracted or indexed in *Chemical Abstracts*, *Chemical Titles*, *Pollution Abstracts*, *Science Research Abstracts*, *Parts A and B*, *Safety Science Abstracts Journal*, *Current Contents*, *Energy Research Abstracts*, and *Engineering Index*.

Soviet Atomic Energy is a translation of *Atomnaya Énergiya*, a publication of the Academy of Sciences of the USSR.

An agreement with the Copyright Agency of the USSR (VAAP) makes available both advance copies of the Russian journal and original glossy photographs and artwork. This serves to decrease the necessary time lag between publication of the original and publication of the translation and helps to improve the quality of the latter. The translation began with the first issue of the Russian journal.

Editorial Board of *Atomnaya Énergiya*:

Editor: O. D. Kazachkovskii

Associate Editors: N. A. Vlasov and N. N. Ponomarev-Stepnoi

Secretary: A. I. Artemov

I. N. Golovin	V. V. Matveev
V. I. Il'ichev	I. D. Morokhov
V. F. Kalinin	A. A. Naumov
P. L. Kirillov	A. S. Nikiforov
Yu. I. Koryakin	A. S. Shtan'
E. V. Kulov	B. A. Sidorenko
B. N. Laskorin	M. F. Troyanov
E. I. Vorob'ev	

Copyright © 1984, Plenum Publishing Corporation. *Soviet Atomic Energy* participates in the Copyright Clearance Center (CCC) Transactional Reporting Service. The appearance of a code line at the bottom of the first page of an article in this journal indicates the copyright owner's consent that copies of the article may be made for personal or internal use. However, this consent is given on the condition that the copier pay the flat fee of \$8.50 per article (no additional per-page fees) directly to the Copyright Clearance Center, Inc., 21 Congress Street, Salem, Massachusetts 01970, for all copying not explicitly permitted by Sections 107 or 108 of the U.S. Copyright Law. The CCC is a nonprofit clearinghouse for the payment of photocopying fees by libraries and other users registered with the CCC. Therefore, this consent does not extend to other kinds of copying, such as copying for general distribution, for advertising or promotional purposes, for creating new collective works, or for resale, nor to the reprinting of figures, tables, and text excerpts. 0038-531X/84 \$8.50

Consultants Bureau journals appear about six months after the publication of the original Russian issue. For bibliographic accuracy, the English issue published by Consultants Bureau carries the same number and date as the original Russian from which it was translated. For example, a Russian issue published in December will appear in a Consultants Bureau English translation about the following June, but the translation issue will carry the December date. When ordering any volume or particular issue of a Consultants Bureau journal, please specify the date and, where applicable, the volume and issue numbers of the original Russian. The material you will receive will be a translation of that Russian volume or issue.

Subscription (2 volumes per year)

Vols. 54 & 55: \$500 (domestic); \$555 (foreign)

Single Issue: \$100

Vols. 56 & 57: \$560 (domestic); \$621 (foreign)

Single Article: \$8.50

CONSULTANTS BUREAU, NEW YORK AND LONDON



233 Spring Street
New York, New York 10013

Published monthly. Second-class postage paid at Jamaica, New York 11431.

Mailed in the USA by Publications Expediting, Inc., 200 Meacham Avenue, Elmont, NY 11003.

POSTMASTER: Send address changes to *Soviet Atomic Energy*, Plenum Publishing Corporation, 233 Spring Street, New York, NY 10013.

SOVIET ATOMIC ENERGY

A translation of *Atomnaya Énergiya*

September, 1984

Volume 56, Number 3

March, 1984

CONTENTS

Engl./Russ.

ARTICLES

Material Behavior Investigations of the VK-50 Reactor Fuel Element Assemblies — V. A. Tsykanov, V. K. Shamardin, A. B. Andreeva, G. P. Kobylanskii, G. I. Maershina, Yu. D. Goncharenko, R. E. Fedyakin, and V. P. Sadulin.	133	131
Determining the Frictional Characteristics of Reactor Materials — V. M. Shchavelin, A. V. Kostochka, A. M. Bolobolichiev, A. A. Kuznetsov, I. S. Golovnin, and Yu. K. Bibilashvili	138	134
Modeling the Gaseous Swelling of Fuel Elements — Yu. G. Degal'tsev, V. F. Kuznetsov, and N. N. Ponomarev-Stepnoi.	141	137
Neutron Cross Sections for the Calculation of the Damaging Dose in Reactor Materials — V. I. Avramenko, Yu. V. Konobeev, and A. M. Strokova	144	139
<i>In Situ</i> Examination of Radiation-Induced Internal Stress Relaxation in the Column of a High-Voltage Electron Microscope — I. I. Novikov, V. A. Ermishkin, V. G. Zharkov, E. N. Samoilov, I. S. Lupakov, and B. S. Rodchenkov.	147	142
Occurrence of Gas Porosity of Annealing Nickel Containing Helium — É. Ya. Mikhlin, V. F. Chkuaseli, Yu. N. Sokurskii, and G. A. Arutyunova	150	144
Small Induction Motors for Nuclear Power Stations — K. A. Alikhanyan	155	148
Automated System for Making Observations, Evaluations, and Forecasts: a Foundation for Comprehensive Protection of the Environment and of the Public Health — E. I. Vorob'ev, V. M. Prusakov, and V. A. Minchenko.	157	149
Radioactive Contamination of the Sea Environment Near the Leningrad Atomic Energy Plant in 1982 — S. M. Vakulovskii and A. I. Nikitin.	162	153
Neutron Inspection of Moisture in Slightly Enriched UO_2 — V. V. Frolov, V. I. Bulanenko, and V. V. Charychanskii	165	155
Average Characteristics of the Slowing Down of Low-Energy Electrons in a Tissue-Equivalent Material — V. A. Pitkevich.	168	158
Measurement of the Ratio of the Fission Cross Sections of ^{238}U and ^{235}U for Neutron Energies in the Range 5.4–10.4 MeV — A. A. Goverdovskii, B. D. Kuz'minov, V. F. Mitrofanov, A. I. Sergachev, S. M. Solov'ev, P. S. Soloshenkov, and A. K. Gordyushin	173	162
Measurement of the Fission Cross Section of ^{238}U and ^{235}U Nuclei by 14 MeV Neutrons — A. A. Goverdovskii, A. K. Gordyushin, B. D. Kuz'minov, A. I. Sergachev, S. M. Solov'ev, and P. S. Soloshenkov.	176	164
"Gas Target" in the Divertor of a Tokamak — M. Z. Tokar'.	178	165

CONTENTS(continued)
Engl./Russ.

LETTERS TO THE EDITOR

γ Radiation Field Generated by Neutrons in an Unbounded Uniform Air Medium — A. V. Zhemerev.	188	173
Determining the Density of Pyrocarbon Coatings on Micropins by Gasification in a Glow Discharge — A. A. Babad-Zakhryapin and I. S. Alekseeva	192	175
Graphite Capsules for Accommodating Indicators of the Temperature and the Neutron Flux in Irradiation Units — T. N. Shurshakova, V. V. Gundorov, and K. V. Grigor'eva.	194	177
Radiation-Induced Changes in the Thermal Conductivity and the Electrical Resistivity of Pyrolytic Graphite — Yu. S. Virgil'ev and I. A. Dmitriev.	196	177
Preliminary Filtering of the Results of Measurements Performed in Exploratory Gamma-Logging — I. M. Khaikovich and V. N. Popov.	198	179
Calibration of Individual Dosimeters by the Absorbed Dose of Photon Radiation — Yu. P. Bakulin, V. P. Bashmakov, E. A. Bogdanov, T. I. Gimadova, N. I. Muratov, and A. V. Tultaev	201	180
Comparative Investigation of the Process of Defect Formation in SiO_2 under Gamma and Gamma-Neutron Irradiation — I. Kh. Abdukadyrova.	203	182

The Russian press date (podpisano k pechati) of this issue was 2/24/1984.
Publication therefore did not occur prior to this date, but must be assumed
to have taken place reasonably soon thereafter.

MATERIAL BEHAVIOR INVESTIGATIONS OF THE VK-50 REACTOR FUEL ELEMENT ASSEMBLIES

V. A. Tsykanov, V. K. Shamardin,
A. B. Andreeva, G. P. Kobylanskii,
G. I. Maershina, Yu. D. Goncharenko,
R. E. Fedyakin, and V. P. Sadulin

UDC 621.039.548.3

In proportion with the increased duration of operation of fuel elements, the probability of their failure due to the radiation environment and corrosion damage of the cans from the coolant side also increases [1]. A study of these phenomena on fuel element cans of the alloy Zr + 1% Nb, most widely used in power reactors, is of great interest. In the present paper, the results of material behavior investigations of fuel element cans and the sheaths of fuel element assemblies (FEA) of the VK-50 reactor after 6 (FEA 1) and 8 (FEA 2) years of operation are considered. Each FEA contains 162 fuel elements and 6 breeder elements, the claddings of which are made from tubes with a diameter of 9.15×0.65 mm (alloy Zr + 1% Nb), annealed at 580°C during 3 h. The hexagonal sheaths are made of Zr + 2.5% Nb alloy. The fuel consists of pellets of 3%-enriched uranium dioxide. The length of the active section of a fuel element is 1980 mm. The coolant flow rate (boiling water) at the fuel element assembly inlet is (0.9 ± 0.1) m/sec, the pressure is 6.9 MPa, and the temperature at the core outlet is 287°C .

The distribution of the density and bulk steam content of the coolant over the height of the core (Fig. 1) is obtained on the basis of measurement of the power distribution and the thermohydraulic characteristics of the reactor. During 5.2 yrs of operation of the fuel elements, the water-chemical cycle of the VK-50 reactor was neutral uncorrected, then a neutral-oxygen cycle was introduced [2], after which the water-chemical indexes of the coolant were improved markedly (Table 1). The oxygen content in the coolant in the upper part of the core is higher by approximately a factor of 100 than at the FEA inlet.

FEA 1 and 2, loaded simultaneously, were operated with variable reactor power (Fig. 2). In this case, the average thermal flux density for an average reactor power value for all the time of the investigations amounted to 240 kW/m^2 , and the maximum thermal flux density for a reactor power of 200 MW attained 680 kW/m^2 . In all, for different reasons, 50 shutdowns occurred during this time, including those due to operation of the scram system approximately 4 times per year; the time of power decrease in this case amounted to 50 sec. Cooling and heating up with planned shutdowns were effected with a rate of 15°C/h . The coolant temperature in the case of prolonged shutdowns was 50°C and in the case of short-time shutdowns it was $\sim 100^\circ\text{C}$. Both FEA in the initial period of time functioned in the peripheral and then in the central regions of the core, and FEA 1 was located at the center $\sim 13\%$ and FEA 2 $\sim 43\%$ of the total duration of their operation.

The fast neutron ($E \geq 0.8 \text{ MeV}$) fluence distribution over the height of the fuel elements is obtained by a numerical method [3], taking into account the distribution of the fuel burn-up and the steam content of the coolant (see Fig. 1). Cooling of FEA 1 and 2 in the cooling pond took place over 2.5 yrs and 5 months, respectively. Fuel elements of the outer row were withdrawn for the investigations of the assemblies.

The absence of damage was established by external examination of the fuel elements of FEA 1 and 2. The deposits on the surface of the fuel elements of FEA 1 are compact but those of FEA 2 are loose, flaky, and easily peeled off (Fig. 3). During separation and transportation the deposits flaked off, and underneath were revealed white sections covered with zirconium oxide. The most intense deposition peeled off at the section between ~ 650 mm from the bottom and ~ 750 mm from the top (FEA 1), but for FEA 2 it was between 100–150 mm from the bottom and 400–450 mm from the top of the fuel elements. The thickness of the deposits was determined by measuring the diameters of the fuel elements with a micrometer with an error of $10 \mu\text{m}$ before and after chemical dissolution of the deposits. The results of these measurements

Translated from Atomnaya Énergiya, Vol. 56, No. 3, pp. 131–134, March, 1984. Original article submitted June 3, 1983.

TABLE 1. Water-Chemical Indexes of the Coolant of the VK-50 Reactor

Operating period of FEA, yrs	Coolant	Concn. of impurities, $\mu\text{g/kg}$				pH	Hardness, $\mu\text{equiv./kg}$
		O ₂	Fe	Cu	Zn		
up to 5,2	Feed water	25	10-30	5-10	5-20	6,0	0,5
	Reactor water	160	20-50	5-20	5-20	6,2	2,5
above 5,2	Feed water	200	5	5	2	6,0	0,5
	Reactor water	200-250	10	20	3	6,2	up to 3

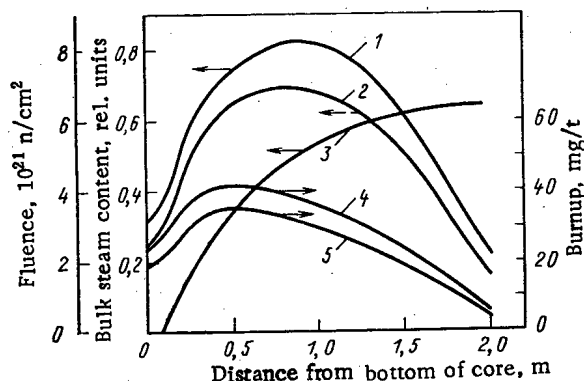


Fig. 1. Variation of the bulk steam content of coolant (3), the fast neutron ($E > 0.8$ MeV) fluence (1, 2) and the fuel burnup (4, 5) in the fuel elements of FEA 1 and 2 respectively over the height of the VK-50 reactor core.

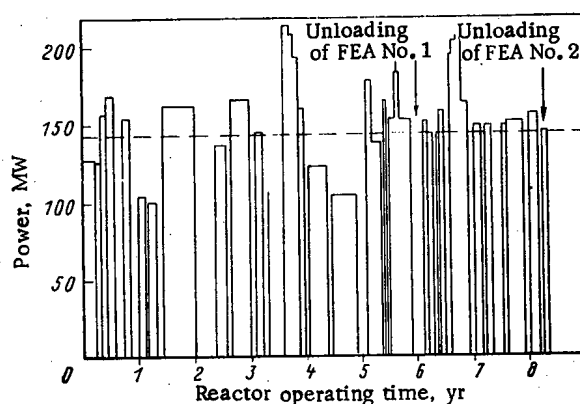


Fig. 2. Graph of the power variation of the VK-50 reactor in the operating period of FEA 1 and 2.

for sections with unpeeled deposits are presented in Table 2. The thickness of the deposits above on more energy-stressed sections of the fuel elements also increases with increase of the residence time of the fuel elements in the reactor.

Radiographic analysis of the deposits was conducted on the DARD remote-controlled diffractometer using the characteristic $\text{CuK}\alpha$ -emission. It was established that the deposits consist mainly of oxides of iron (Fe_2O_3) and copper (CuO). The presence was detected also of manganese oxides (Mn_2O_4). The oxide film is zirconium dioxide with monoclinic modification,

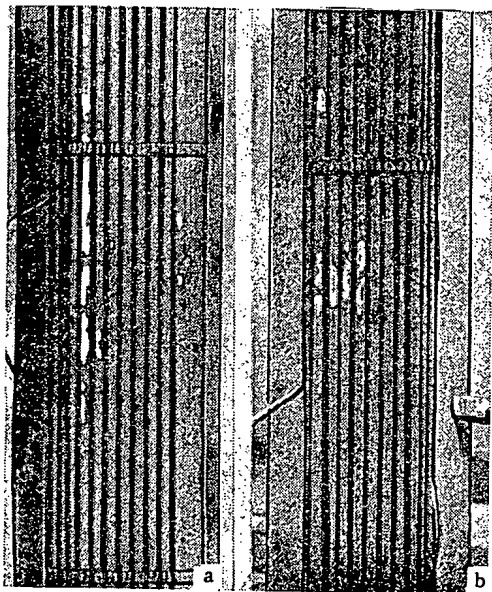


Fig. 3. External view of the fuel elements of FEA 1 (a) and 2 (b).

TABLE 2. Thickness of Deposits on Different Sections of Fuel Elements, μm

Distance from bottom of active zone, mm	FEA 1	FEA 2
100	10	20
600	50-60	75-100
1600	25	50
2000	10	15

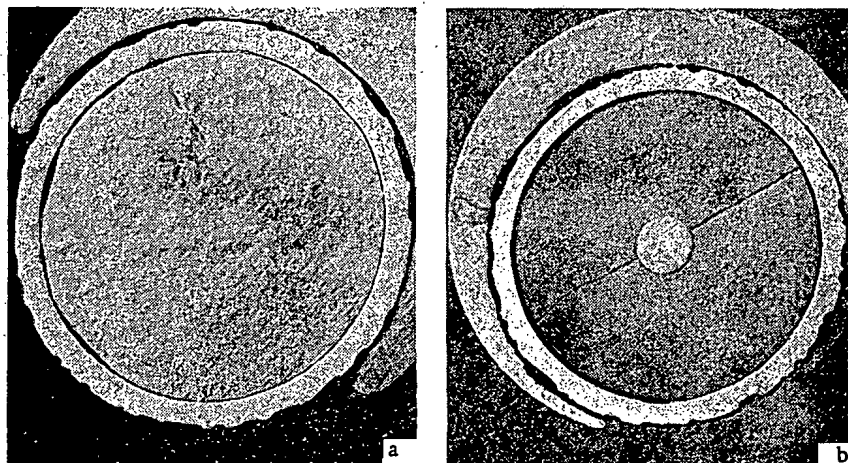


Fig. 4. Macrostructure of transverse thin sections of fuel elements of FEA 1 (a) and 2 (b) in the upper part of the active zone - 1920 mm from the bottom of the active zone ($\times 9$).

The differences in the values of the diameter of the fuel elements in the original state and after residence in the reactor are small and are due mainly to oxidation of the external surface of the fuel element cans. The internal and external surfaces of the sheath tubes of both FEA were covered with a nonuniform thickness of oxide film, somewhat more for FEA 2, the maximum thickness of which amounts to 200 μm at the fins. The formation of the thickest oxide films on these sections obviously is caused by the presence of residual stresses, stimulating corrosion [4].

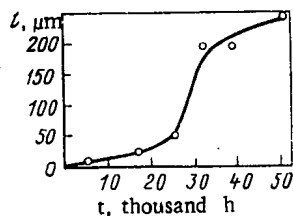


Fig. 5. Kinetics of the variation of the maximum thickness of the oxide films l on fuel elements of the VK-50 reactor.

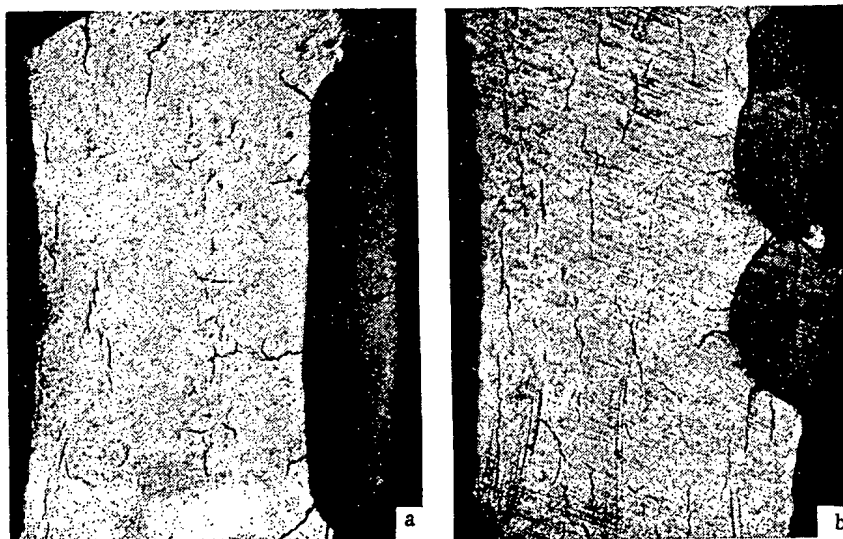


Fig. 6. Microstructure of transverse thin sections of the cans of fuel element assemblies 1 (a) and 2 (b) in the upper part of the core (1920 mm from the bottom of the core).

No appreciable deformation of the cladding, impairment of its intactness and squeezing of the fuel was observed during metallographic examinations of FEA 1 and 2. A strong pitting of the outer surface of the claddings was observed in the cladding material in the zone of the fuel column and had a focal nature (Fig. 4). The foci, together with the continuous oxide film, are distributed over the whole of the outer surface of the cans, and corrosion damage of the FEA 2 cans is expressed to a large degree. It should be noted that for both FEA the intensity of oxidation of the outer surface varies as a function of the height of the fuel elements. On sections distant from the active zone by 1500-1800 mm, an increased amount of foci with a length of less than 800 μm is observed, having moreover maximum depth. It should be noted that in the zone of compensating volume, where there is almost no energy release during operation of the fuel elements, the corrosion of the outer surface of the claddings has a uniform nature and proceeds with the formation of thin ($\sim 10 \mu\text{m}$) oxide films. On the power-stressed sections of the fuel element claddings, the origination of more intense boiling is possible, which can lead to increased corrosion. Using the published data [5], a curve was constructed of the maximum thickness of the oxide films on the fuel element claddings vs their residence time (Fig. 5). The nature and intensity of the corrosion vary in proportion to the increase of operating time. In the initial stage, a predominantly continuous corrosion is observed, accompanied by the formation of oxide films with a thickness of up to 50 μm ; in the next stage, an acceleration of the corrosion foci develops, after which a stage of gradual increase of thickness of the foci starts with approximately the same speed as for the continuous corrosion. A marked difference in the state of the outer surface of the fuel element claddings is detected in the region of the spacer grids of stainless steel and far from them. Thus, for FEA 2, the thickness of the layered oxide films below the spacer grids attained $\sim 500 \mu\text{m}$, and between them $\sim 250 \mu\text{m}$.

The orientation of hydrides over the perimeter of the claddings is predominantly annular, and only on sections adjacent to points of local oxidation are radially oriented hydrides observed (Fig. 6). The hydrogen content in the fuel element claddings was estimated by the

TABLE 3. Transient mechanical properties
of the Material of the FEA Fuel Element
Claddings

FEA	Section of ele- ment	Fluence, neutrons/ cm ²	T _{test} = 20 °C				T _{test} = 300 °C			
			σ_h , MPa	$\sigma_{0.2}$, MPa	δ_{tot} , %	δ_p , %	σ_h , MPa	$\sigma_{0.2}$, MPa	δ_{tot} , %	δ_p , %
1	Top	$3 \cdot 10^{21}$	460	420	10,6	5,7	320	260	11,7	5,1
	Middle	$7 \cdot 10^{21}$	400	370	11,6	5,7	285	250	18,7	6,5
	Bottom	$2 \cdot 10^{21}$	520	475	13,1	4,6	370	340	10,0	4,0
2	Top	$3,5 \cdot 10^{21}$	520	480	10,7	4,5	400	360	13,8	4,6
	Middle	$8,5 \cdot 10^{21}$	465	435	15,7	5,9	300	240	14,0	5,2
	Bottom	$3 \cdot 10^{21}$	515	450	16,7	4,2	360	310	8,7	3,7

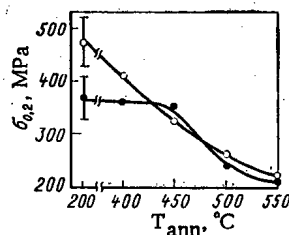


Fig. 7. Dependence of the yield point of annular samples sectioned from the middle (●) and lower (○) parts of the fuel element claddings of FEA 1 on the temperature of isochronic annealing.

method of spectral-isotopic balancing [6]. The content of hydrogen in the fuel element claddings of FEA 1 (A) and 2 (B) in different sections of the fuel element is shown below, 10^{-2} mass %:

	A	B
Top	1.3	2.4
Middle	5.0	7.3
Bottom	4.1	4.3

The amount of hydrogen in the fuel element claddings with larger burnup (FEA 2) is somewhat higher than for the fuel elements of FEA 1. The fuel element claddings in the middle section of the active zone were subjected to the maximum hydrogenation, and those in the upper section to the minimum hydrogenation.

The average values of the mechanical properties in the case of short-time tensile strength tests of 5-6 annular samples cut off from different sections of FEA fuel element claddings are shown in Table 3. The spread of the values attained 10%. No significant difference is observed in the mechanical properties of the fuel element cladding material of the FEA investigated in identical sections over the height of the active zone, which may be due to their weak dependence on the fluence in excess of $5 \cdot 10^{20}$ neutrons/cm² [7].

For the middle section of the fuel element claddings of both FEA, a reduction of σ_h and $\sigma_{0.2}$ is found, by comparison with those observed for the upper and lower sections. The reason for this may be an increase of temperature of the fuel element claddings on sections with high thermal loadings (middle part of the fuel elements) when operating the reactor at maximum power (see Fig. 2), as a result of which annealing of the radiation defects takes place [8]. Obviously, this is the consequence of the formation on these sections of thick deposits and an oxide film, which considerably impair the heat transfer. The results of the experiment, in the course of which isochronic (2 h) annealings of annular samples from the fuel elements of FEA 1 (Fig. 7) were carried out, showed that the yield point of samples sectioned from the

middle part of the fuel elements is reduced appreciably with an annealing temperature in excess of 450°C, and from the lower section from 400°C. These data confirm the supposition made. The results of post-reactor investigations of the fuel elements after operation during 6 and 8 years in the VK-50 reactor confirmed the quite high efficiency of the alloy Zr + 1% Nb.

LITERATURE CITED

1. V. V. Kalashnikov and V. I. Solyany, *At. Energ.*, 44, 6, 499 (1978).
2. A. I. Zabelin, Preprint NIIAR-23(538) [in Russian], Dimitrovgrad (1982).
3. V. D. Sidorenko, Preprint IAE-1434 [in Russian], Moscow (1967).
4. B. G. Parfenov et al., *Corrosion of Zirconium and Its Alloys* [in Russian], Atomizdat, Moscow (1967), p. 50.
5. V. A. Tsykanov et al., Preprint NIIAR-20(535) [in Russian], Dimitrovgrad (1982).
6. V. S. Belokopytov and T. A. Nazarenko, Preprint NIIARP-246 [in Russian], Dimitrovgrad (1974).
7. E. Yu. Rivkin, B. S. Rodchenkov, and V. M. Filatov, *Strength of Zirconium Alloys* [in Russian], Atomizdat, Moscow (1974), p. 57.
8. V. S. Belokopytov, A. S. Pokrovskii, and G. P. Kobylanskii, *Problems of Nuclear Science and Technology. Series Radiation Material Behavior, Procedures and Techniques of Irradiation* [in Russian], No. 6 (1975), p. 13.

DETERMINING THE FRICTIONAL CHARACTERISTICS OF REACTOR MATERIALS

V. M. Shchavelin, A. V. Kostochka,
A. M. Bolobolichiev, A. A. Kuznetsov,
I. S. Golovnin, and Yu. K. Bibilashvili

UDC 621.039.548:621.891

Study of the frictional characteristics of reactor materials is associated with the solution of the problem of mechanical interaction of the fuel and the shell in the fuel elements of water-water power reactors. In particular, these characteristics are necessary for the evaluation of the stress-strain state of fuel-element shells in transient conditions of reactor use [1].

Data on the frictional coefficients between the fuel and the shell are very scarce and pertain to nonreactor conditions [2]. Therefore, the development of methods and means for studying the friction directly in in-reactor conditions remains a pressing need.

In the present work, a method and apparatus for investigating the frictional characteristics of the fuel-shell frictional pair in laboratory conditions are described, and results of determining the frictional coefficients between uranium dioxide and zirconium alloy as a function of slip path, temperature, contact pressure, surrounding medium (air and helium), and hardness of the metallic sample are given. These developments are the preliminary stage in creating an analogous apparatus for in-reactor investigations.

Method and Samples. The conditions of frictional contact correspond to slip over a plane. The motionless fuel samples are attached at their ends to a plane mobile metallic sample, which lies between them and performs reciprocating translational motion. The chosen scheme is more suitable for in-reactor measurements in conditions where the space inside the experimental channel is extremely limited, offers the possibility of dispensing with supporting bearings in the active zone, and imposes no constraints on the choice of moving sample, which must simply have longitudinal rigidity. Provision is made for determining the coefficients of static and dynamic friction and also, where necessary, the degree of wear of the samples and the state of their working surface by means of weighing and profile recording. In the experiments, the dependence of the frictional coefficients on the slip path was determined, the rate of slip remaining constant. In addition, the influence of the contact pressure, temperature, and medium on the frictional characteristics of the pairs investigated was studied.

The fuel-material samples used were uranium-dioxide pellets with a roughness of the end working surface in the range $R_a = 0.9-1.8 \mu\text{m}$. The pellets were preliminarily checked for the

Translated from *Atomnaya Energiya*, Vol. 56, No. 3, pp. 134-136, March, 1984. Original article submitted April 22, 1983.

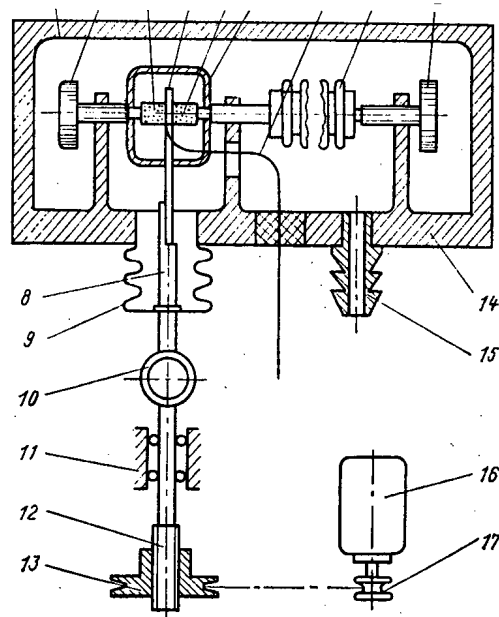


Fig. 1. TREK-1 apparatus for nonreactor investigations.

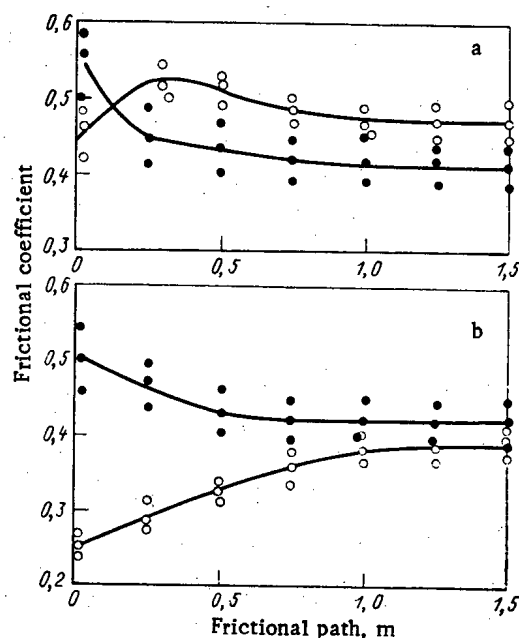


Fig. 2. Dependence of the frictional coefficient of the uranium-dioxide-zirconium-alloy pair on the slip path in a helium medium at 293 (open circles) and 573°K (filled circles) for zirconium-alloy samples with a chemically treated surface (a) and with an oxide film (b).

absence of visible cracks, chips, and internal defects [3]. Plane samples of the alloy Zr + 1% Nb were used, in the form of plates of dimensions 80 × 12 mm and thickness 2 mm. Such a thickness completely ensures the required longitudinal rigidity, allowing not only pulling but also pushing of the bracket-fixed samples with change in the direction of motion in the course of the experiment.

The metallic samples chosen for the experiment had a Vickers hardness $HV = 1300-2300$ MPa and a working-surface roughness of 0.2-0.3 μm .

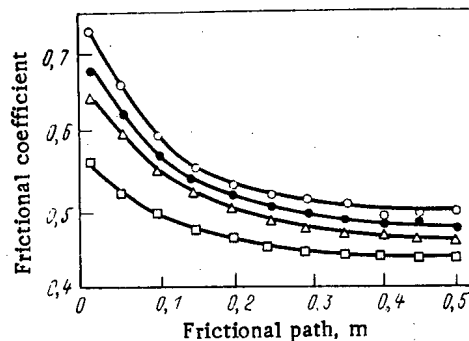


Fig. 3. Dependence of the frictional coefficient of the uranium-dioxide-zirconium-alloy pair for zirconium samples (with a chemically treated surface) at a contact pressure of 5 MPa on the Vickers hardness: 1300 (open circles), 1500 (filled circles), 1700 (triangles), and 2300 MPa (squares).

TREK-1 Apparatus for Nonreactor Experiments. The apparatus is shown in Fig. 1. On the baseplate 14 of vacuum chamber 1, a loading system with adjusting screws 2 is placed; this system ensures, with the assistance of the bellows 7, the application of the required compressive force to the cylindrical fuel samples 3. The plane mobile metallic sample 4 is fixed to coupling rod 8, which is introduced into the chamber through bellows 9 and impelled into reciprocal translational motion by a motor located outside the chamber. The region of frictional contact of the sample is surrounded by heater 5. The temperature of the metallic sample is measured by thermocouple 6, placed in a drilled chamber running from the side surface of the sample to the center of the working zone. Thermocouples are also applied to each fuel sample (through the central cavity). Outlet 15 is used to pump out the chamber and fill it with helium to atmospheric pressure.

The frictional force between the samples is measured using tensometric ring 10, inserted in connecting rod 8. The drive system includes the reversing electric motor 16, the belt transmission 17, the helical pair 13, and the supporting guide 11 of coupling rod 12 fitted with roller bearings. The supports provided with shock absorbers and the use of a belt transmission allows the influence of electric-motor vibrations on the frictional-pair sample to be eliminated.

The course and velocity of the moving sample may be varied in the limits from 8 to 50 mm and from 200 to 2000 $\mu\text{m}/\text{sec}$, respectively. The bellows mechanism permits loading by a force of up to 1300 N.

Experimental Results. The characteristics of the frictional interaction are influenced by the temperature, contact pressure, gaseous medium, slip path, and hardness of the samples.

The influence of high temperature was determined for two metallic samples: with a chemically treated working surface and with an oxide-film coating. Experiments were conducted at 293 and 573°K in a helium medium. The variation in the frictional coefficient for a uranium-dioxide-zirconium-alloy pair is shown in Fig. 2. In both cases, the contact pressure was 5 MPa and the slip velocity 200 $\mu\text{m}/\text{sec}$. It is evident that the relative stabilization of the frictional coefficient occurs on a slip path of 0.5-1 m. At high temperature, the spread of the results usually increases, but for samples with an oxide film the frictional coefficient is markedly less than for chemically treated samples.

Inspection of the zirconium samples after the experiments reveals scratching and gouge tracks, as well as adhering uranium-dioxide particles; the roughness of the working surface increases sharply. At 573°K, the slip path is 0.6 m and the mean wear depth of the zirconium samples, determined by profile recording, is $\sim 15 \mu\text{m}$. The wear of the uranium-dioxide pellets is slight.

To determine the influence of a helium medium on the frictional coefficient at 293°K, with a contact pressure of 5 or 10 MPa, experiments were performed first in air and then in helium and, conversely, first in helium and then in air. The chamber was filled with high-purity helium, without special purification from water vapor and oxygen. From the obtained data it follows that the variation of the gas medium has no effect on the frictional coefficient.

It is of undoubted interest to study the dependence of the frictional coefficient of the pair on the hardness of the metallic sample. Experimental results obtained at 573°K in a helium medium for four batches of zirconium samples with different Vickers hardness are shown in Fig. 3. Deviation of the hardness within each batch was no more than 3%. Each point represents the mean value of the frictional coefficient over the results of ten measurements. The given data indicate that the initial hardness of the zirconium samples has a marked influence on the frictional coefficient of the fuel-shell pair.

The method developed here and the apparatus which has been constructed provide the basis for the development of apparatus for the in-reactor investigation of friction in fuel-shell-material pairs.

LITERATURE CITED

1. G. I. Sukhanov, At. Tekh. Rub., No. 8, 3 (1979).
2. J. Wood et al., J. Nucl. Mater., 88, 81 (1980).
3. V. T. Gevondyan et al., in: Techniques of Radiational Experiments [in Russian], No. 9, Énergiya, Moscow (1980), p. 46.

MODELING THE GASEOUS SWELLING OF FUEL ELEMENTS

Yu. G. Degal'tsev, V. F. Kuznetsov,
and N. N. Ponomarev-Stepnoi'

UDC 621.039.548.343

Ensuring the reliable operation of power-reactor fuel elements entails studying diverse and complex problems; important among these is the gaseous swelling of fuel materials, which has considerable influence on the efficiency of the fuel elements.

Radiational gas swelling of the fuel depends on many factors: the rate and depth of burn-up, the temperature distribution, the structure of the fuel core, the shell strength, etc., which means that theoretical models must be used in the calculations. Accurate calculation of gaseous swelling is practically impossible at present, because the model concepts adopted are imperfect and even contradictory. In addition, the models most commonly describe local swelling of the fuel, which is unrelated to the stress-strain state of the fuel element as a whole.

Therefore, the most natural means of developing engineering modeling is to use approximate models with a small number of basic parameters to describe the physical processes making a determining contribution to the swelling. The correctness of the model is confirmed by analysis of the results of experimental investigations of the given fuel elements and comparison with data obtained by numerical modeling on a computer using the given model.

In accordance with the currently available theoretical concepts and experimental data, the processes of gas liberation and swelling of high-temperature oxide fuel are based on the following mechanisms, in our view.

1. The basic reason for swelling of the oxide film at high temperature is the formation of large (diameter more than 1 μm) intergrain bubbles with a low pressure of gaseous fission products.
2. In the course of irradiation, delivery of gaseous fission products from the grain body to the boundaries occurs by diffusion of gas atoms, the high concentration of which maintains the process of radiational resolution from small internal bubbles with a high pressure.
3. The population of low-mobility intragrain bubbles is stabilized in the course of irradiation, and makes practically no contribution to the gaseous swelling of the fuel [1].
4. Irradiation at high temperature changes the structure of the fuel, which influences the gas migration and the character of the swelling: There is an increase in equiaxial grains; columnar grains are formed as a result of the motion of lenticular pores and directed recrystallization in the temperature gradient [2]; recondensation of the fuel occurs on the intern-

Translated from Atomnaya Énergiya, Vol. 56, No. 3, pp. 137-138, March, 1984. Original article submitted November 4, 1983.

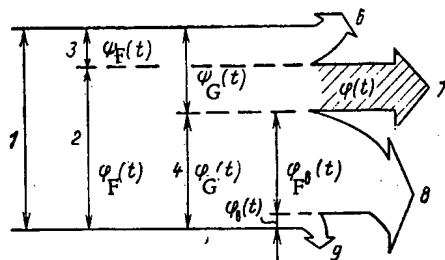


Fig. 1

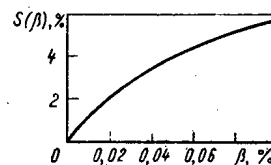


Fig. 2

Fig. 1. Model of the behavior of gaseous fission products in oxide fuel on irradiation: 1) gas produced; 2, 3) gas inside and outside fuel matrix; 4, 5) gas inside and outside grain; 6) gas outside fuel; 7, 8) gas in intergrain and intra-grain bubbles and solid solution, respectively.

Fig. 2. Dependence of the mean bulk swelling $S(\beta)$ of a UO_2 sample on the burnup β : the curve corresponds to calculation and the point to experiment.

al surface of the shell, as well as transformation of the pore and bubble system in the non-uniform temperature field on account of the accumulation of gaseous fission products (e.g., the formation of interconnected channels [3], the conversion of closed porosity into open porosity, etc.).

According to the model adopted, the behavior of the gaseous fission products (Xe and Kr) is illustrated in Fig. 1. At each moment of time t , the gas formed is in a fuel matrix in the form of a supersaturated solid solution in a uranium-dioxide lattice, $\varphi_{sol}(t)$; in the form of large (diameter more than $1 \mu m$) intergrain bubbles, $\varphi(t)$; and in the form of small intragrain bubbles, $\varphi_I(t)$. It is assumed that the fraction of gas formed which is outside the fuel matrix makes no contribution to the swelling. In this case, the fraction of gas in the intergrain bubbles may be determined:

$$\varphi(t) = \psi_G(t) - \psi_F(t),$$

where $\psi_G(t)$ is the relative proportion of gas diffusing from the grain to its boundaries, and is determined by the equivalent-sphere model [4], taking account of the temperature dependence of the diffusion coefficient; $\psi_F(t)$ is the relative leakage of gaseous fission products from the fuel, which also depends on the temperature and is calculated on the basis of experimental data [5].

In describing the space-time deformational behavior of a fuel element in the case of swelling fuel and restraining action of the shell, the model employs an equation obtained on the basis of [6], relating the hydrostatic stress in the fuel $\sigma_A(t)$ resulting from the accumulation of gaseous fission products in the intergrain bubbles to the swelling $S(t)$:

$$\sigma_A(t) = \frac{T}{273[S(t) + \epsilon_0]} \left[24.7 \int_0^t \beta_G(t) dt \varphi(t) + \epsilon_0 \right],$$

where T is the local fuel temperature, $^{\circ}K$; $\beta_G(t)$ is the rate of burnup, $g U \cdot cm^{-3} \cdot h^{-1}$; ϵ_0 is the initial porosity of the fuel (it is assumed that the pores are filled with a technological gas under normal conditions). The fuel element is regarded as a multilayer cylinder consisting of rigidly interconnected layers with different (but constant within the limits of each layer) properties, corresponding to the local parameters of the fuel element. This approach allows the features of the spatial (over the core radius) energy distribution [7], temperature [8], and structure in the fuel core to be taken into account.

To obtain specific results on the basis of the given model, the OVERAT program is written in FORTRAN [9] for use on a BESM-6 computer. Results obtained with this program are given below. The efficiency of the given model was verified on the basis of a comparison of the calculated results with experimental data. Experimental investigations were conducted with dense ($>95\%$ of the theoretical density) pellets of small-grain uranium dioxide in the shell, on the universal loop apparatus of a water-water reactor of the type considered in [10]. The

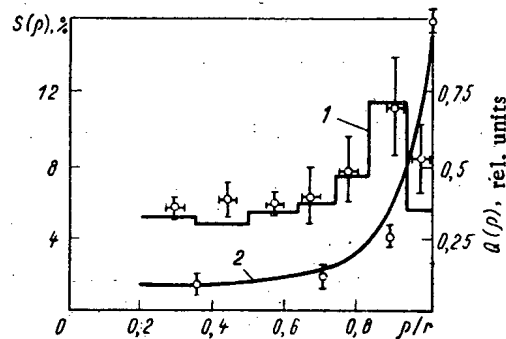


Fig. 3. Distribution of the local gas swelling $S(\rho)$ (1) and the relative energy distribution $Q(\rho)$ (2) on the radius of a cylindrical UO_2 sample: the curves correspond to calculation and the points to experiment (r , sample radius).

experimental conditions were close to those in [11] ($T = 1750^\circ\text{C}$, burnup $\sim 10^{20}$ fissions/ cm^3), the only difference being that the temperature gradient for the given samples was $\sim 200^\circ\text{C}\cdot\text{cm}^{-1}$. The theoretical curve and experimental value of the mean bulk swelling of UO_2 (initial grain size $10\ \mu\text{m}$) after irradiation to $\sim 0.1\%$ burnup are shown in Fig. 2. The swelling was determined by the method of hydrostatic weighing with an error of no more than 10%.

The spatial distribution of local gas swelling over the radius of the UO_2 pellets was studied metallographically with analysis of the results on the Kvantimet-720 apparatus. Experimental and theoretical radial distributions of the gaseous swelling of the fuel over the cross section of a cylindrical sample irradiated to a burnup of $\sim 3 \cdot 10^{19}$ fission/ cm^3 are shown in Fig. 3, together with the relative energy distribution [7].

As follows from the given comparison, the space-time distribution of the gaseous swelling of UO_2 under irradiation obtained by calculation on the basis of the given method is in satisfactory agreement, within the limits of experimental error ($\sim 10\text{--}15\%$), with the results of measurements; this is acceptable for practical purposes.

LITERATURE CITED

1. J. Turnbull, J. Nucl. Mater., **38**, 212 (1972).
2. W. Chubb, V. Storhok, and D. Keller, J. Nucl. Mater., **44**, 136 (1972).
3. J. Turnbull and C. Friskney, J. Nucl. Mater., **71**, 238 (1978).
4. A. Booth, GRDC-721 (September, 1957).
5. N. N. Ponomarev-Stepnoy and A. A. Khroulev, in: Proc. of TEPG Conference, Jülich, Session E129 (1972).
6. Yu. I. Likhachev and V. Ya. Pupko, Strength of Heat-Liberating Elements of Nuclear Reactors [in Russian], Atomizdat, Moscow (1975).
7. N. N. Ponomarev-Stepnoi et al., At. Energ., **34**, No. 3, 197 (1973).
8. V. F. Kuznetsov, At. Energ., **47**, No. 6, 410 (1979).
9. V. F. Kuznetsov, Preprint of the Institute of Atomic Energy, IAE-3275/5 [in Russian], Moscow (1980).
10. Yu. G. Nikolaev et al., First Geneva Conference, USSR Paper No. R/621 (1955).
11. J. Turnbull, J. Nucl. Mater., **50**, 62 (1974).

NEUTRON CROSS SECTIONS FOR THE CALCULATION OF THE DAMAGING DOSE IN REACTOR MATERIALS

V. I. Avramenko, Yu. V. Konobeev,
and A. M. Stroková

UDC 621.039.53

In comparing the results of irradiating reactor materials and various neutron spectra with data obtained in the irradiation of materials by charged particles, the damaging dose is taken to be characterized by the number of displacements per atom. Calculation of the number of displacements per atom is based on the formula

$$D = \left(\int_0^{\infty} \sigma_{\text{dis}}(E) F(E) dE \right) \Phi, \quad (1)$$

where $\sigma_{\text{dis}}(E)$ is the neutron cross section of displacement of the atoms of the material at a neutron energy E ; $F(E)$ is the energy spectrum of the neutron flux normalized to unity; Φ is the flux of neutrons of all energies ($E > 0$). The cross section $\sigma_{\text{dis}}(E)$ is determined by the sum of the cross sections of elastic and inelastic neutron scattering by nuclei of the material, the cross sections of the nuclear reactions ($n, 2n$) and (n, α), etc., and also the form of the cascade function.

According to recent recommendations [1], calculations of the damaging dose in terms of the displacements per atom may be based on the US data system of ASTM [2] or the DAMSIG-81 data library [3]. In both libraries, the displacement cross section is given in 640-group representation: 620 groups in the energy scale of the SAND II program [4] and 20 additional groups with uniform energy divisions in the range 18-20 MeV. The ASTM data system is based on the ENDF/B IV library of neutron cross sections and the DAMSIG-81 library mainly on the ENDF/B III library. The aim of the present work is to develop a system of group neutron displacement cross sections that is as close as possible to the international standard, for the basic energy scales used in reactor calculations in the USSR.

Tables 1 and 2 show the system of constants developed. The mean (over the neutron group) displacement cross sections have been determined for Al, Si, Cr, Fe, Ni, Cu, Zr, Mo, W, C, V, Nb, Ta, Pb, and also Kh18N8 stainless steel. For the first nine materials, the displacement cross sections obtained in [5] provided the starting point; for graphite, the data of [6], based on the cascade function of [7]. For the first ten chemical elements, the results of [5, 6] were also used in the comparison with the DAMSIG-81 library. For V, Nb, Ta, and Pb, multigroup constants were developed on the basis of the data of [8], recommended by [9]. The group cross sections for steel were obtained by a method described earlier on the basis of the corresponding cross sections for Fe, Cr, and Ni. The effective threshold energy of displacement in the cascade function in the TRN model, as in the DAMSIG-81 library, was taken to be 40 eV for all the materials considered, except graphite, for which it was 60 eV. In averaging the cross sections within the energy groups, the recommended procedure of averaging by means of a standard neutron cross section is of the form

$$\varphi(E) = \begin{cases} 1/E & E \leq 2.5; \\ \exp(-E_0/0.965) \text{sh} \sqrt{2.29E}, & E > 2.5, \end{cases} \quad (2)$$

where E is expressed in MeV. Variation in form of the fission spectrum and the binding energy within finite limits (2.0-2.5 MeV) has no considerable influence on the results of the calculations.

The number of displacements per atom at a specified point of the active zone of the reactor is defined as

$$D = \left(\sum_i \sigma_i F_i \right) \Phi, \quad (3)$$

Translated from *Atomnaya Énergiya*, Vol. 56, No. 3, pp. 139-141, March, 1984. Original article submitted June 29, 1983.

Group No.	Neutron energy	C	Al	Si	V	Cr	Fe	Ni	Cu	Zr	Nb	Mo	Ta	W	Pb	Kh18N8 stainless steel
-1	14.5-14.0 MeV	619,4	1444	1683	2592	2417	1913	2055	2511	3088	2590	2938	2227	2387	2028	2015
0	14,0-10,5	619,4	1316	1353	2329	2115	1913	1761	2208	2438	2246	2461	1892	2024	1847	1937
1	10,5-6,5	620,4	1298	1049	1966	1846	1767	1487	1899	1661	1863	1798	1350	1337	1343	1759
2	6,5-4,0	702,0	1340	1132	1750	1577	1535	1297	1557	1276	1426	1453	997,0	973,3	1149	1524
3	4,0-2,5	810,3	1349	998,0	1515	1344	1323	1148	1145	976,5	1090	1143	761,0	832,0	1034	1313
4	2,5-1,4	688,5	1104	1100	1054	1010	911,3	924,6	812,7	811,8	817,5	836,3	570,8	615,7	596,2	930,2
5	1,4-0,8	768,3	893,5	849,2	714,1	640,8	474,9	665,2	635,7	709,9	614,7	651,9	377,3	388,1	300,8	519,9
6	0,8-0,4	772,1	728,9	578,4	421,8	385,4	343,9	409,3	455,3	619,9	513,3	433,1	234,2	262,3	185,2	356,6
7	0,4-0,2	650,4	451,7	453,1	335,8	191,1	207,3	323,6	292,4	376,6	352,6	353,0	137,5	168,2	158,6	213,7
8	0,2-0,1	453,3	400,5	214,4	249,0	226,1	143,4	210,8	168,1	205,3	200,8	212,3	84,00	104,1	104,9	163,7
9	100-46,5 KeV	258,4	180,1	40,53	156,3	98,71	103,0	151,0	130,9	110,1	73,30	117,5	50,13	62,68	62,62	106,1
10	46,5-21,5	139,0	116,4	17,84	92,11	38,58	119,4	91,71	66,78	54,13	34,72	53,67	24,30	33,46	28,92	102,6
11	21,5-10,0	70,16	7,774	10,05	234,2	19,77	10,95	170,5	43,77	25,77	16,70	23,86	9,596	17,58	13,53	25,30
12	10,0-4,65	32,97	5,782	6,232	164,7	35,76	21,38	29,21	30,80	13,36	8,920	10,94	2,743	10,78	6,356	24,59
13	4,65-2,15	15,93	2,728	3,223	76,45	13,88	7,089	20,79	17,00	9,914	3,321	6,336	0,126	10,56	2,171	9,407
14	2,15-1,0	5,704	1,439	1,634	2,534	2,892	5,977	8,643	8,296	2,818	0,332	4,939	0	10,93	0,356	5,635
15	1000-465 eV	3,475	0,747	0,811	0,398	0,954	1,818	2,276	7,969	0,240	0	1,937	—	11,93	0,003	1,699
16	465-215	0	0,334	0,128	0,006	0,107	0,075	0,195	1,281	1,066	—	5,724	—	38,82	0	0,090
17	215-100	—	0,144	0,008	0	0,135	0,109	0,288	0,101	0,196	—	8,519	—	164,9	—	0,128
18	100-46,5	—	0,085	0,012	—	0,193	0,160	0,420	0,129	0,007	—	2,959	—	26,96	—	0,187
19	46,5-21,5	—	0,085	0,018	—	0,288	0,237	0,619	0,245	0,010	—	38,21	—	530,3	—	0,277
20	21,5-10,0	—	0,086	0,026	—	0,430	0,348	0,913	0,435	0,014	—	1,009	—	1835	—	0,408
21	10,0-4,65	—	0,131	0,030	—	0,616	0,509	1,330	0,678	0,020	—	2,231	—	44,85	—	0,594
22	4,65-2,15	—	0,188	0,057	—	0,908	0,749	1,958	1,052	0,030	—	0,360	—	63,88	—	0,874
23	2,15-1,0	—	0,217	0,083	—	1,361	1,101	2,885	1,613	0,044	—	0,505	—	3,472	—	1,291
24	1,0-0,465	—	0,382	0,120	—	1,942	1,604	4,209	2,375	0,064	—	0,637	—	3,709	—	—
25	0,465-0,215	—	—	—	—	—	—	—	—	—	—	—	—	—	—	—
T		0,020	1,470	1,170	19,20	18,30	10,70	23,50	14,40	0,260	1,120	2,650	0,940	2,410	0,240	13,09

TABLE 2. Group Displacement Cross Sections for the WIMS and DLC-23/CASK Energy Divisions

Group No.	neutron energy	WIMS				DLC-23/CASK		
		cross section, 10^{-28} m^2				neutron energy	cross sec., 10^{-28} m^2	
		Fe	Zr	C	Kh18N8 stainless steel		Fe	Kh18N8 stainless steel
1	10,0-6,066 MeV	1755	1588	615,2	1742	15,0-12,2 MeV	1913	1980
2	6,066-3,679	1519	1230	741,3	1502	12,2-10,0	1913	1923
3	3,769-2,231	1256	928,6	770,7	1256	10,0-8,18	1877	1863
4	2,231-1,353	843,1	795,7	694,8	864,0	8,18-6,36	1732	1729
5	1,353-0,821	452,4	707,3	771,1	502,3	6,36-4,96	1633	1612
6	0,821-0,500	357,0	648,6	786,8	374,6	4,96-4,06	1459	1458
7	0,500-0,3025	296,5	496,1	719,9	297,9	4,06-3,01	1442	1413
8	0,3025-0,183	190,9	321,9	607,7	194,4	3,01-2,46	1180	1198
9	0,183-0,111	127,5	206,5	455,1	154,3	2,46-2,35	1147	1154
10	111-67,34 keV	131,6	133,9	313,0	135,4	2,35-1,83	1024	1055
11	67,34-40,85	65,57	85,42	208,2	72,13	1,83-1,11	663,4	691,4
12	40,85-24,78	165,9	53,45	135,7	136,5	1,11-0,5	384,4	414,0
13	24,78-15,03	7,194	32,99	87,86	23,96	0,5-0,111	209,2	220,4
14	15,03-9,118	13,71	20,26	54,59	22,79	111-3,35 keV	59,97	61,94
15	9,118-5,53	27,12	12,98	33,48	28,88	3,35-0,583	5,235	5,132
16	5,53-3,519	8,349	12,01	19,77	13,83	583-101 eV	0,091	0,111
17	3,519-2,239	6,449	9,145	13,87	7,505	101-29,0	0,182	0,212
18	2,239-1,425	5,522	3,720	7,262	5,506	29,0-10,7	0,318	0,373
19	1,425-0,907	6,178	1,545	4,586	5,505	10,7-3,06	0,560	0,654
20	907,5-367,3 eV	1,034	0,168	2,100	0,994			
21	367,3-148,7	0,087	1,000	0	0,102			

where σ_i and F_i are the neutron cross section of displacement and the normalized energy spectrum of the neutrons for the i -th group, respectively.

For alloys, the group displacement cross section may be found from the expression

$$\sigma_d = \sum_i \sigma_i^{(j)} \rho^{(j)}, \quad (4)$$

TABLE 3. Number of Displacements per Atom (DPA) Produced by a Flux of 10^{22} neutron/cm² in Kh18N8 Stainless Steel for Reactors of Various Types

Reactor	DPA			Source of data on neutron spectrum
	$E > 0$	$E > 0.1$ MeV	$E > 0.4$ MeV	
BOR-60 (CAZ*)	4.84	5.43	8.14	[11]
BN-600 (ZHE†)	3.03	4.50	8.96	[11]
BN-1600 (ZHE)	2.45	4.30	9.90	[11]
EBR II (CSZ)	4.81	5.45	8.19	[11]
ETR	—	7.01	9.36	[12]
GTR	—	7.61	9.51	[12]
VVER-440	—	6.50	9.66‡	[12]
MR	—	5.65—7.1	8.45—9.0	Present work
RBMK	—	5.0—7.1	8.3—8.5	Present work
Inner wall of VVER body	—	6.63	9.45	[13]

*CAZ, center of active zone.

†ZHE, zone of high enrichment.

‡E > 0.5 MeV.

where $\sigma_i^{(j)}$ and $\rho^{(j)}$ are the group displacement cross section and atomic fraction of the j -th chemical element in the alloy. It is supposed that, at the current level of knowledge of the cascade function, it is sufficient to take account solely of the basic components of the alloy. Thus, for stainless steel and other alloys of the system Fe-Cr-Ni, only the three principal components need be taken into account. The neutron cross sections shown in Tables 1 and 2 for Kh18N8 steel are obtained in this approximation. It is assumed here that the atomic fractions of Fe, Cr, and Ni do not differ from their mass content (for steel Kh18N8, values of 0.74, 0.18, and 0.08, respectively, are taken). For 15Kh2MFA steel, from which the body of water-water reactors is made, it is sufficient to use the displacement cross sections for Fe, since the content of alloying components is small (note that this is as in the US standard [2]); for zirconium alloys, the constructional material of the active zones of thermal-neutron reactors, it is sufficient to use the displacement cross section of pure Zr.

Tables 1 and 2 give the multigroup constants of the displacement cross sections of materials for the 26-group representation, for the energy scale of the WIMS program, and for the energy divisions of the DLC-23/CASK program used in the calculation programs (ANISN, DOT) for neutron fluxes in the body and indicator samples of water-water reactors. Table 1 also gives the neutron displacement cross sections for thermal neutrons [10]. Note that, in reactor spectra, as a rule, ~98% of the total number of displacements per atom are the result of neutrons of energy >0.01 MeV. The contribution of thermal neutrons to the formation of displacements need only be taken into account in those cases where the flux intensity of thermal neutrons exceeds the intensity of the fast-neutron flux by a factor of ten or more. Comparison of the number of displacements per atom obtained from Eq. (3) with the result given by Eq. (1), on the basis of initial data on the displacement cross sections, shows that, for the neutron spectra in the active zone of fast, water-water, graphite, heavy-water, and certain other reactors, the discrepancy in the results is no more than 1%.

Table 3 compares the damaging dose produced by a flux of 10^{22} neutron/cm² in various reactors. It follows from these data that the damaging power of neutrons in various reactors (and at various points within the active zones of several reactors) is different. In connection with this, the use of the neutron cross sections in Tables 1 and 2 is recommended. The damaging doses, expressed in numbers of displacements per atom, for Kh18N8 stainless steel according to the data of Tables 1 and 2 are approximately 10% less than those calculated on the basis of the damage cross sections recommended in [14].

LITERATURE CITED

1. Proceedings of Advisory Group Meeting on Nuclear Data for Radiation Damage Assessment and Related Safety Aspects, IAEA-TECDOC-263, Vienna (1982), p. 329.
2. Standard Practice for Characterizing Neutron Exposures in Ferritic Steels in Terms of Displacements per Atom, ASTM E693-79, USA (1980).

3. W. Zijp et al., Damage Cross Sections Library DAMSIG-81, Netherlands, ECN-104 (1980).
4. E. McElroy et al., A Computer Automated Iterative Method for Neutron Flux Spectra Determination by Foil Activation AFWL-TR-67-41, USA (1967).
5. M. Lott et al., in: Proceedings on Applications of Nuclear Data in Science and Technology, Vol. 1, IAEA, Vienna (1973), p. 89.
6. D. Reed, The Comparison of Carbon Atom Displacement Rate in Graphite in the Dragon Reactor, the Petten HFR and Low Enrichment HTR. Dragon Project Report, DP-559, Great Britain (1967).
7. M. Thompson and S. Wright, J. Nucl. Mater., 16, 146 (1965).
8. D. Doran and N. Graves, in: Irradiation Effects on the Microstructure and Properties of Metals, ASTM STP 611, American Society for Testing and Materials (1976), p. 463.
9. "Recommendations for the calculation of materials irradiation exposures," Nucl. Technol., 37, 358 (1978).
10. L. Greenwood and R. Smither, Displacement Damage Calculations with ENDF/B V, IAEA-TECDOC-263, IAEA, Vienna (1982), p. 185.
11. V. V. Orlov, A. A. Proshkin, and A. N. Tuzov, in: Collected Papers of COMECON Conference on the Exchange of Experience on the Development and Introduction of Apparatus with Fast Reactors Based on the BOR-60 Reactor [in Russian], Dimitrovgrad (1972), p. 30.
12. R. D. Vasil'ev et al., in: Metrology of Neutron Measurements at Nuclear-Physics Installations. Proceedings of the First All-Union School [in Russian], Vol. 1, Izd. TsNIIatom-inform, Moscow (1976), p. 226.
13. É. B. Brodtkin et al., in: Collected Abstracts of the Proceedings of the Third All-Union Scientific Conference on the Protection of Nuclear-Engineering Installations from Ionizing Radiation [in Russian], Tbilisi (1981), p. 67.
14. V. N. Bykov and Yu. V. Konobeev, At. Energ., 43, No. 1, 20 (1977).

IN SITU EXAMINATION OF RADIATION-INDUCED INTERNAL STRESS RELAXATION
IN THE COLUMN OF A HIGH-VOLTAGE ELECTRON MICROSCOPE

I. I. Novikov, V. A. Ermishkin,
V. G. Zharkov, E. N. Samoilov,
I. S. Lupakov, and B. S. Rodchenkov

UDC 621.039.531

Internal stresses produced mechanically or thermally in metals have substantial effects on physical processes, in particular on recovery during annealing [1], fast-electron scattering [2], radiation growth [3], and so on.

Size change occurs in a deformed body on annealing on account of thermally activated motion of lattice defects produced by internal stresses. The deformation rate for a crystal is determined by the activation energy (if a single mechanism applies) and is exponentially dependent on temperature. It is also proportional to the bulk density of the defects whose motion produces the deformation. Therefore, by varying the defect density (for example, by irradiation) one can alter the components of the deformation rate due to the motion of these defects, in particular point ones.

This made it of interest to examine the internal-stress relaxation under irradiation in a material exposed to high-energy electrons. We used specimens of Zr + 1% Nb, Zr + 2.5% Nb alloys and aluminum. The zirconium-based alloys were deformed by rolling followed by annealing at 550°C for 5 h. The aluminum specimens were prepared from rolled foil of thickness 10 μm .

The specimens were irradiated with electrons in the column of a JEM-1000 high-voltage electron microscope HVEM at an electron flux density of $1 \cdot 10^{19} \text{ cm}^{-2} \cdot \text{sec}^{-1}$ and an accelerating voltage of 1 MV. We measured the distances between a series of reference points rigidly linked to the matrix to determine the tensor for the deformation arising during irradiation by the use of the negative images. These reference points for the zirconium alloys were small spherical deposits of a second phase that did not alter during irradiation. The refer-

Translated from *Atomnaya Énergiya*, Vol. 56, No. 3, pp. 142-144, March, 1984. Original article submitted December 14, 1982.

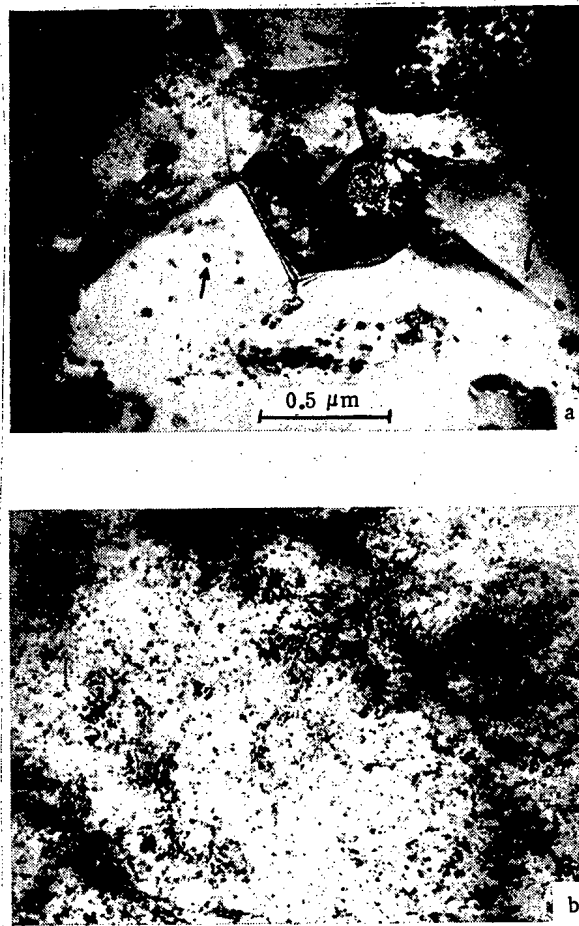


Fig. 1. Irradiated parts of specimens of Zr + 2.5% Nb (a) and aluminum (b). The arrows indicate the reference markers.

ence points for the aluminum specimens were small copper particles previously deposited under vacuum (Fig. 1a and b), which were firmly attached to the surfaces. The deformation in a given part of the structure was determined from the change in distance between the reference markers.

To correct for possible change in microscope magnification during the experiment, an unirradiated part of the specimen was photographed almost at the same time as the irradiated part. Any change in distance between the reference markers in this part was due to change in magnification and was correspondingly incorporated in deriving the deformation tensor. This method of determining the local deformation provided an overall accuracy of about 0.05% when we used an 1818 stereometer made by Carl Zeiss (Jena) with standard negatives of size 6×9 cm.

No substantial changes in the phase distributions in the zirconium alloys under irradiation were observed. After irradiation for ~ 1.5 h, there were also no resolved dislocation loops. The defect structure was not altered in the zirconium alloys or in the aluminum.

In the case of Zr + 1% Nb, measurement of the distances between the reference points in the irradiated areas showed that there was no deformation. In the aluminum, the irradiated region expanded. On the other hand, the sizes of the parts of the Zr + 2.5% Nb alloy on irradiation either decreased or increased along both axes in the plane of the foil (i.e., perpendicular to the beam, while the dependence of the absolute deformation on dose or time was the same (Fig. 2). This planar expansion or contraction of the irradiated areas is difficult to explain in terms of point-defect condensation in particular crystallographic planes [4]. Also, the deformation did not alter on subsequent annealing, which distinguishes this effect from radiation growth [5].

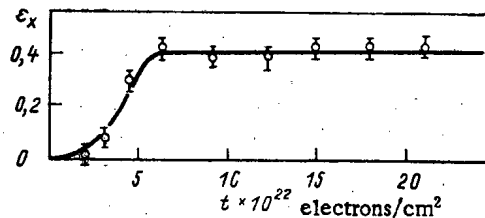


Fig. 2. The observed $\epsilon(t)$ dependence: ϵ_x) one of the principal values in the deformation tensor; —) theoretical relation for $k \approx 10^{-3} \text{ sec}^{-1}$ in (7); O) experiment.

One naturally explains the difference in behavior between the irradiated parts in terms of differences in physical state before irradiation. The state of a part of a crystal at a given instant is completely described by the distributions of mobile defects and potential barriers, together with the stresses in the bulk, which together determine the subsequent behavior. As no qualitative differences were found in the microstructures of the irradiated parts, the differences in behavior under irradiation were ascribed to differences in internal stress.

A simple quantitative description in good agreement with the experiments can be obtained by assuming that the deformation under irradiation is viscous. There are internal tensile or compressive average stresses σ_0 in an irradiated disk region, while the planar surfaces of the disk are free from stresses, and in the relation between the deformation rate $\dot{\epsilon}$ in viscous motion and the stress σ is [6]:

$$\dot{\epsilon}(t) = B\sigma(t), \quad (1)$$

where $B = B(t)$ is a coefficient defining the capacity of the material for plastic flow and which is proportional to the point-defect concentration $n(t)$ at a given instant. Then

$$B(t) = k_B n(t), \quad (2)$$

where k_B is a quantity dependent on the diffusion characteristics. We assume that the point-defect concentration was linearly dependent on the irradiation time (we neglected point-defect annihilation and escape from the boundary of the region):

$$n(t) = k_n t, \quad (3)$$

where k_n is dependent on the irradiation intensity and the inelastic scattering cross section related to the formation of Frenkel pairs.

The stresses acting in a given region were taken also as linearly dependent on the deformation in the radial direction:

$$\sigma(t) = \sigma_0 - k_\sigma \epsilon(t), \quad (4)$$

where k_σ is the elastic characteristic of the material.

From (1)-(4) we get an integral equation for σ :

$$\sigma(t) = \sigma_0 - k \int_0^t \sigma(t) dt, \quad (5)$$

where $k = k_B k_n k_\sigma$; the solution to (5) is

$$\sigma(t) = \sigma_0 \exp \left[-\frac{k}{2} t^2 \right], \quad (6)$$

and then from (4) we have

$$\epsilon(t) = \frac{\sigma_0}{k_\sigma} \left[1 - \exp \left(-\frac{k}{2} t^2 \right) \right]. \quad (7)$$

Formula (7) describes the experimental curves for Zr + 2.5% Nb with $k \approx 10^{-3} \text{ sec}^{-1}$.

We note that the character of these curves and the dose corresponding to the inflection region are the same as those for the dependence of radiation growth of this alloy on dose

(expressed in displacements/atom) on neutron irradiation. However, in the saturation region, the effect is larger in magnitude by a factor 2-4 than the radiation growth [5].

The following conclusions are therefore drawn. A deformed material has internal stresses whose absolute value and sign may vary from one part to another. These stresses may locally exceed the macroscopic yield point. The principal values ϵ_x and ϵ_y in the deformation tensor are equal in each particular case (within the limits of the errors). The shear components of the stress tensor, which provide dislocation movement, are practically zero, which indicates that the internal stresses are of hydrostatic type, and that they relax only by point-defect motion, i.e., by a diffusion mechanism. The relaxation rate is proportional to the point-defect concentration or the radiation intensity at a given internal stress. The ratio of the number of stretched regions to the number of compressed ones is evidently determined by the character of the thermomechanical treatment, and this ratio is less than one for treatments that on average produce compressive stresses (it is about 0.2 as indicated by the experiments for Zr + 2.5% Nb). The initial internal stresses determine the deformation at saturation.

LITERATURE CITED

1. T. Hasegawa et al., *Acta Metall.*, **30**, 235 (1982).
2. S. Amelinckx, *The Direct Observation of Dislocations*, Academic Press (1964).
3. P. Kelly, "Irradiation growth in Zr," in: *Proc. Int. Conf. on Physical Metallurgy of Reactor Fuel Elements*, Berkeley (1973).
4. *J. Nucl. Mater.*, **90**, 1 (1980).
5. R. Adamson, *Am. Soc. Test. Mater.*, 326 (1977).
6. J. G. Loitsyanskii, *Mechanics of Liquids and Gases* [in Russian], Nauka, Moscow (1970), p. 450.

OCCURRENCE OF GAS POROSITY ON ANNEALING NICKEL CONTAINING HELIUM

É. Ya. Mikhlin, V. F. Chkuaseli,
Yu. N. Sokurskii, and G. A. Arutyunova

UDC 621.039.531

Introduction. There are many theoretical and experimental studies on gas porosity, which has a considerable effect on the behavior of materials under irradiation. However, at present there is no agreed view on which mechanisms play the decisive part in the development of gas porosity and gas release. The observed mobility of gas bubbles [1] is the starting point in concepts in which the porosity growth is determined by the collision and fusion of such bubbles (pores) [2, 3]. These concepts have been used in kinetic models for gas swelling [4-7] and gas release [4, 5], where it is assumed that the pore motion is produced mainly by surface diffusion, with the diffusion coefficient for a pore related to the radius r by an expression of the type

$$D_b^{(s)}(r) = \frac{3}{2\pi} D_s \frac{\Omega^{4/3}}{r^4}. \quad (1)$$

There are, however, numerous papers in which the pore evolution is related to the diffusion of single atoms [8-10].

One can eliminate the uncertainty on the roles of these mechanisms only on the basis of new and revised concepts on the pore mobility as affected by radius [11, 12]. On these concepts, the diffusion coefficient for equilibrium gas pores, which is related to surface diffusion, is defined by

$$D_b^{(s)} = \frac{3}{2\pi} D_s \frac{\Omega^{4/3}}{r^4} W(r), \quad (2)$$

where $W(r)$ is a factor describing the suppression of the mobility because the gas density increases as r decreases. It should be noted that $W(r)$ decreases from 1 at large r to 0 at $r \approx 1$ nm [11, 12]. Then $D_b^{(s)}(r)$ at first increases as r decreases, but after the maximum falls

Translated from *Atomnaya Énergiya*, Vol. 56, No. 3, pp. 144-148, March, 1984. Original article submitted February 17, 1983.

Declassified and Approved For Release 2013/09/14 : CIA-RDP10-02196R000300040003-5
 rapidly to 0. For $r \leq 1$ nm, $D_b(r) \approx D_b^{(v)}(r)$; since the diffusion coefficient for not very large pores is made up of contributions from surface diffusion $D_b^{(s)}$ and bulk diffusion $D_b^{(v)}$:

$$D_b(r) = D_b^{(s)}(r) + D_b^{(v)}(r). \quad (3)$$

The contribution from $D_b^{(v)}$ decreases rapidly (as r^{-3}) as r increases. The detailed values of D_v and D_s (volume and surface diffusion) determine whether the mobility is a nonmonotone function of r and has a minimum (sometimes deeper) at $r \approx 1$ nm. These concepts agree with the experimental data available for some materials, according to which the mobilities of small pores are quite small [13-15]. Equations (2) and (3) describe these data satisfactorily. Also, (2) and (3) imply that a marked reduction in mobility occurs only in a comparatively narrow size range, outside of which it remains fairly high, which disposes of the assumption that the porosity evolution is due to collision and fusion of moving pores. The contribution to the porosity from the diffusion of single gas atoms can be incorporated within the framework of this approach as a particular case of the diffusion of pores containing single gas atoms.

This, however, is not the only significance of (2). One usually employs (1) in models, which greatly overestimates the mobilities of small pores, and therefore such models are hardly reliable in predicting fuel behavior. Therefore, a quantitative model for gas porosity and gas release has been devised [16] in which the pore mobility is defined by (2) and (3). Calculations from this agree well with the available data on swelling and gas release for oxide fuel, and also with the pore-size distribution within grains. This model [16] also provides quantitative description of details of the gas porosity such as the size distribution for pores in defect-free parts of the grains and at dislocations and grain boundaries and edges. We examine below how well the model describes these details by comparing the distributions calculated separately for pores in defect-free parts of grains and pores at dislocations with the corresponding distributions obtained by electron microscopy of helium-irradiated nickel specimens after annealing.

Experiment. Nickel foils of thickness about 10 μ m were bombarded at 100°C with helium ions to a concentration of 0.15 at.%. Then these foils were annealed at 700°C for 1, 3, 6, 12, 100, and 1000 h. At the end of annealing, the foils were thinned down and an electron microscope was used to examine the gas porosity. We processed the electron micrographs for various parts to derive 33 histograms for the size distributions at various annealing times. Some of the photographs provided separate histograms for pores at dislocations and away from them. These 17 paired histograms are particularly informative in interpreting porosity development. There were variations within fairly wide limits in the pore density and size distribution even for pictures relating to the same annealing time, which may be due to physical inhomogeneity (for example, in the diffusion parameters or thickness), but which also may be of purely statistical character. Therefore, the comparison with the calculations was based on histograms for 3 and 100 h of annealing, since these were statistically the most representative (6 and 5 correspondingly). We then added the numbers of pores in a given size range from all the primary histograms with a given annealing time to derive the resultant histogram, which was normalized to the total number of pores (Figs. 1 and 2).

Basic Model Concepts. These have been presented previously [16] and amount to the following:

1. Porosity develops because of the collision and fusion of moving gas pores [2, 3]. The motion of the pores may be due, for example, to a temperature gradient. Also, there is random wandering.
2. All the pores are spherical and equilibrium ones, while the gas they contain is described by the equation of state for a nonideal gas.
3. Even the smallest gas-vacancy clusters down through complexes containing only one atom of gas each may be considered as pores, which enables one to incorporate the diffusion of single gas atoms into the general scheme. Any pore can then be considered as due to fusion of n one-atom pores (pores of the initial size).

Structural defects such as dislocations and grain boundaries or edges retard the displacement of the pores they trap and thus act as sites for more rapid pore enlargement. Therefore, there are distinctive regions associated with each type of defect, and there are also defect-free regions, for each of which the porosity development is described separately.

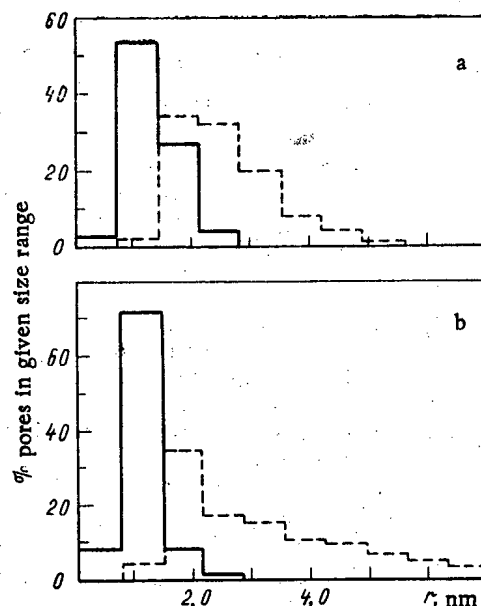


Fig. 1. Size histograms after 3 h of annealing at $D_v = 10^{-14}$ $\text{cm}^2 \cdot \text{sec}^{-1}$ in both regions: a) for pores in the defect-free part of the grains ($F_{\text{exp}}^{(1)} = 3.0 \cdot 10^{16} \text{ cm}^{-3}$; $F_{\text{calc}}^{(1)} = 5.5 \cdot 10^{17} \text{ cm}^{-3}$); b) for pores at dislocations ($F_{\text{exp}}^{(2)} = 1.1 \cdot 10^{16} \text{ cm}^{-3}$; $F_{\text{calc}}^{(2)} = 4.0 \cdot 10^{16} \text{ cm}^{-3}$); here and in the subsequent figures, each histogram has been normalized to the corresponding total number of pores; —) calculation; ----) experiment.

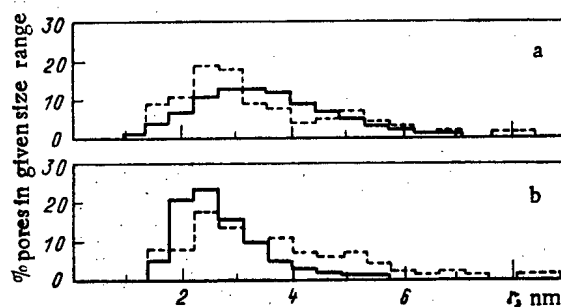


Fig. 2. Size histograms after 100 h of annealing with $D_v = 10^{-14}$ $\text{cm}^2 \cdot \text{sec}^{-1}$ in both regions: a) for pores in the defect-free part of the grains ($F_{\text{exp}}^{(1)} = 3.5 \cdot 10^{15} \text{ cm}^{-3}$, $F_{\text{calc}}^{(1)} = 2.4 \cdot 10^{16} \text{ cm}^{-3}$); b) for pores at dislocations ($F_{\text{exp}}^{(2)} = 2.9 \cdot 10^{15} \text{ cm}^{-3}$, $F_{\text{calc}}^{(2)} = 1.5 \cdot 10^{16} \text{ cm}^{-3}$).

In our experiments, the annealing was performed in the absence of temperature gradients, so the pores moved only on account of their Brownian motion. The concentration $F_i^{(1)}$ of pores of size i in the defect-free region (first region) is described [16] by

$$\frac{dF_i^{(1)}}{dt} = \sum_{j=1}^J v_{j,i-1}^{(1,1)} F_j^{(1)} F_{i-1}^{(1)} - F_i^{(1)} \sum_{j=1}^N v_{ij}^{(1,1)} F_j^{(1)} - F_i^{(1)} \sum_{\beta=2}^4 \sum_{j=1}^N v_{ij}^{(1,\beta)} F_j^{(\beta)} - \sum_{\beta=2}^4 \Phi_i^{(1,\beta)}. \quad (4)$$

Here the first sum characterizes the increase in $F_i^{(1)}$ due to collisions between pores in region 1 of size less than i . The second and third sums describe the decrease in $F_i^{(1)}$ due to collisions of pores of size i from the first region with pores of other sizes from the first region and from all other regions correspondingly ($\beta = 2$ for dislocations, $\beta = 3$ for boundaries, and $\beta = 4$ for grain edges). The last sum describes the flow of pores of size i to free parts of dislocations, boundaries, and edges. In the case of isothermal annealing,

$$v_{ij}^{(1,2)} = 4\pi [D_b(r_i) + D_b(r_j)](r_i + r_j), \quad (5)$$

where $D_b(r)$ is given by (3), in which $D_b^{(s)}(r)$ is defined by (2) and

$$D_b^{(v)}(r) = \frac{3}{4\pi} D_v \left(\frac{\Omega}{r}\right)^3.$$

The change in the concentration $F_i^{(2)}$ of pores at dislocations (region 2) is defined by

$$\frac{dF_i^{(2)}}{dt} = \sum_{j=1}^{i-1} v_{j,i-j}^{(1,2)} F_j^{(1)} F_{i-j}^{(2)} - F_i^{(2)} \sum_{j=1}^N v_{ij}^{(1,2)} F_j^{(1)} + \sum_{j=1}^J v_{j,i-j}^{(2,2)} F_j^{(2)} F_{i-j}^{(2)} - F_i^{(2)} \sum_{j=1}^N v_{ij}^{(2,2)} F_j^{(2)} + \Phi_i^{(1,2)}, \quad (6)$$

where the first two sums characterize the changes in $F_i^{(2)}$ due to collisions of pores from the first region with pores associated with dislocations and $\Phi_i^{(1,2)}$ is the rate of change in $F_i^{(2)}$ due to diffusion flow of pores of size i to free parts of dislocations. The third and fourth sums describe the changes in $F_i^{(2)}$ due to collision of pores involved in one-dimensional random wandering along dislocations. Consideration of the contributions of these processes to the porosity kinetics [7] gives

$$v_{ij}^{(2,2)} = \frac{l(t)}{hd} \int_0^h q[l(t) - r_{ij}, t'] dt'. \quad (7)$$

Results and Discussion. Figures 1 and 2 show the size histograms for pores from the first and second regions obtained from calculations for annealing for 3 and 100 h together with the observed histograms. The calculations were performed for 700°C with the following values for the parameters: atomic volume $\Omega = 11 \cdot 10^{-24}$ cm³, dislocation density $d = 3 \cdot 10^{10}$ cm⁻², grain size $L = 20$ μm, surface energy $\gamma = 2400$ erg/cm² (1 erg = $1 \cdot 10^{-7}$ J), van der Waals constant $b = 40 \cdot 10^{-24}$ cm³ (for helium), suppression factor W determined for $q = 400 \cdot 10^{-24}$ cm³ [11, 12], surface self-diffusion coefficient $D_s = 5.8 \cdot 10^{-9}$ cm²·sec⁻¹,* and volume self-diffusion coefficient $D_v = 10^{-14}$ cm²·sec⁻¹.†

The histograms show that the model calculations for both regions give size distributions close to the observed ones. There is good agreement, particularly for the first region, for specimens annealed for 100 h. However, on annealing for three hours the calculated distribution is somewhat to the left of the experimental one. Also, the calculated distribution for pores at dislocations is somewhat displaced to smaller sizes by comparison with that for the defect-free parts of the grains, whereas the observed one is slightly displaced towards larger dimensions.

The latter feature indicates that the mobility of the pores along the dislocations (at least for small ones) is somewhat higher than in the defect-free part of the grain. This is fairly reasonable, since point defects diffuse near the core of a dislocation much more rapidly than far from it [22]. Therefore, the pore displacement along dislocations may be somewhat more rapid, at least by the self-diffusion mechanism. Of course, this applies to small pores, whose displacement is associated with volume self-diffusion and whose dimensions do not exceed the cross section of the area of elevated mobility near the core.

On this basis we performed the calculation in which it was assumed that in the second region (dislocations) $D_v = 3 \cdot 10^{-13}$ cm²·sec⁻¹; Figs. 3 and 4 show the results, which indicate that the size distribution for pores at dislocations is displaced to the right, while the distribution for the defect-free part is virtually unaltered. This confirms the above assumption about increased mobility of small pores along dislocations.

Conclusions. When helium-saturated nickel is annealed, the gas porosity is closely described by the model, as in various cases considered previously [16], if the mobility is described by expressions (2) and (3). There is fairly good agreement between the calculated and

*The value of D_s for 700°C according to [17] lies in the range $1.6 \cdot 10^{-10}$ – $1.2 \cdot 10^{-8}$ cm²·sec⁻¹, while according to [18] it is in the range $4 \cdot 10^{-9}$ – $9.3 \cdot 10^{-8}$ cm²·sec⁻¹. The value used is approximately in the middle of the range in D_s common to these two papers.

† D_v at 700°C may have a value from 10^{-15} to $2 \cdot 10^{-14}$ cm²·sec⁻¹ [19–21].

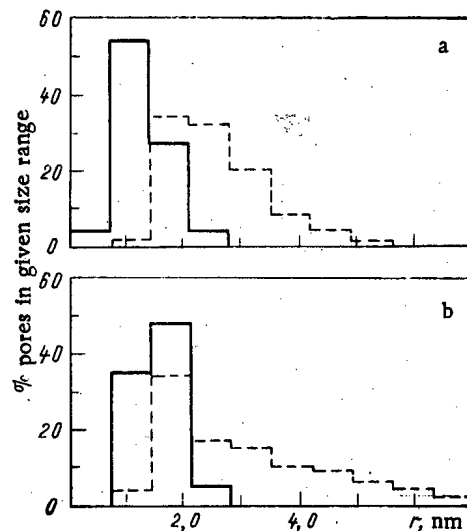


Fig. 3. Size histograms after 3 h of annealing when D_v is increased for pores at dislocations ($D_v = 3 \cdot 10^{-13} \text{ cm}^2 \cdot \text{sec}^{-1}$): a) for the defect-free parts of grains ($F_{\text{exp}}^{(1)} = 3.0 \cdot 10^{16} \text{ cm}^{-3}$, $F_{\text{calc}}^{(1)} = 5.5 \cdot 10^{17} \text{ cm}^{-3}$); b) for pores at dislocations ($F_{\text{exp}}^{(2)} = 1.1 \cdot 10^{16} \text{ cm}^{-3}$, $F_{\text{calc}}^{(2)} = 1.8 \cdot 10^{16} \text{ cm}^{-3}$).

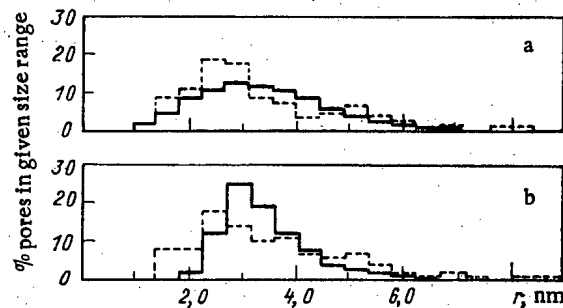


Fig. 4. Size histograms after 100 h of annealing when D_v is increased for pores at dislocations ($D_v = 3 \cdot 10^{-13} \text{ cm}^2 \cdot \text{sec}^{-1}$): a) for pores in the defect-free parts of grains ($F_{\text{exp}}^{(1)} = 3.5 \cdot 10^{15} \text{ cm}^{-3}$, $F_{\text{calc}}^{(1)} = 2.2 \cdot 10^{16} \text{ cm}^{-3}$); b) for pores at dislocations ($F_{\text{exp}}^{(2)} = 2.9 \cdot 10^{15} \text{ cm}^{-3}$, $F_{\text{calc}}^{(2)} = 1.3 \cdot 10^{16} \text{ cm}^{-3}$).

observed size distributions for the defect-free region and for pores at dislocations. The calculations from the model also confirm the assumption that there is elevated mobility for small pores along dislocations.

LITERATURE CITED

1. R. Barnes and D. Mazey, *Proc. R. Soc. A*, **275**, 47 (1963).
2. R. Barnes, *J. Nucl. Mater.*, **11**, 35 (1964).
3. V. M. Agranovich, E. Ya. Mikhlin, and L. P. Semenov, Third Geneva Conference 1964, USSR Paper No. 338a.
4. H. Warner and F. Nichols, *Nucl. Appl. Technol.*, **9**, 148 (1970).
5. C. Dollins and F. Nichols, *J. Nucl. Mater.*, **66**, 143 (1977).
6. E. Mikhlin and V. Chkuaseli, *Phys. Status Solidi, A*, **29**, 331 (1975).
7. E. Ya. Mikhlin and V. F. Chkuaseli, in: *Reactor Material Sciences (Proceedings of the Conference on Reactor Material Science, Alushta, 29 May-1 June 1978)* [in Russian], Vol. 2, Izd. TsNIIatominform, Moscow (1978), p. 124.
8. P. Prajoto, A. Wazzan, and D. Okrent, *Nucl. Eng. Des.*, **48**, 461 (1978).
9. J. Turnbull, *J. Nucl. Mater.*, **62**, 325 (1976).
10. M. Wood, *ibid.*, **82**, 257 (1979).
11. E. Mikhlin, *Phys. Status Solidi, A*, **56**, 763 (1979).

12. E. Mikhlin, J. Nucl. Mater., 87, 405 (1979).
13. R. Cornell and G. Bannister, Proc. Brit. Ceram. Soc., 7, 855 (1967).
14. M. Gulden, J. Nucl. Mater., 23, 30 (1967).
15. L. Willertz and P. Schewmon, Metall. Trans., 1, 2217 (1970).
16. E. Mikhlin and V. Chkuaseli, J. Nucl. Mater., 105, 223 (1982).
17. Yu. S. Kaganovskii and Do Van Hai, Fiz. Met. Metalloved., 39, 828 (1975).
18. P. Maiya and J. Blakely, J. Appl. Phys., 38, 6981 (1967).
19. M. Feller-Kniepmeier, M. Grundler, and H. Helfmeier, Z. Metallk., 67, 533 (1976).
20. A. Wazzan, J. Appl. Phys., 36, 3596 (1965).
21. A. Messner, R. Benson, and J. Dorn, Trans Am. Soc. Met., 53, 227 (1961).
22. R. Balluffi, Phys. Status Solidi, 42, 11 (1970).

SMALL INDUCTION MOTORS FOR NUCLEAR POWER STATIONS

K. A. Alikhanyan

UDC 621.313.13+621.311.2:621.039

Nuclear power engineering in the Soviet Union is a field of industry requiring induction motors for various mechanisms, in company with a wide range of other components. Improvements in the structural schemes of nuclear power stations and experience in their operation are dependent upon the creation of new motors for use under nuclear-power conditions. Small (fractional horsepower) induction motors are used to drive various mechanisms involved in the functioning of a number of systems under both normal and fault conditions. These motors are principally used for driving slide valves and stop valves on water lines in the reactor and for various actuator mechanisms. It is not possible to use ordinary general-purpose motors in these applications.

The first series-A4 motors were developed in three structural designs and installed on the Lovisa nuclear power station in Finland. They were installed in clean reactor buildings and in contamination boxes (0.12-0.55 kW) in the upper (0.18 kW) and lower (0.12, 0.18 kW) levels of the reactor hall. The motors are continually subjected to high ambient temperatures and humidities at high pressures and at significant levels of radiation. The highest doses of radiation (100 rad/h) are to be found at the lower level of the reactor hall. These conditions, plus the demand for high reliability under all conditions of operation, including fault conditions, dictate the choice of structural and insulating materials.

Studies have shown that despite the high temperature (120°C) and humidity (saturated steam), they can have the same power ratings as their parent machines.

Motors with ratings of 0.18 and 0.25 kW, developed and brought into mass production for power stations equipped with the VVER-1000 reactor, are also intended for driving slide and stop valves. The development of new motors is called for by the specific features of operation of the power stations furnished with VVER-1000s: elevated temperatures (70°C), relative humidities (up to 100%), pressures (up to 1 kPa), radiation effects ($5 \cdot 10^5$ mrad/h), serviceability under all fault conditions, characterized by sharp increases in temperature (up to 150°C), pressure (490 kPa), and radiation ($5 \cdot 10^7$ mrad/h). There are also severe restrictions relating to reliability, earthquake resistance, hermetic sealing, operation without servicing and repair for sustained periods (up to 2 years).

For use inside the motors of insulating materials of heat stability class F, conductors, coatings, and varnishes for impregnation have to be selected bearing in mind their subsequent use on a nuclear power station. Tests and operating trials have confirmed their quality.

These machines were developed in 1979-1981 and unified as far as possible with machines created earlier for nuclear power stations in Cuba and Libya. These were subject to even more rigorous demands on earthquake resistance.

The motors for experimental mechanisms comprise a special group in themselves. They have relatively low electromechanical time constants ($t_M = 0.03$ sec) for rapid operation of ac-

Translated from Atomnaya Energiya, Vol. 56, No. 3, pp. 148-149, March, 1984. Original article submitted August 30, 1983.

Induction motor, screened protected		Induction motor, totally enclosed: $t = 60^{\circ}\text{C}$, $n = 90\%$, $p = 0.085 - 0.1008 \text{ MPa}$				
Clean enclosure with contamination boxes		Upper level of reactor hall	Lower level of reactor hall	Shut-off valve VVÉR-1000	Shut-off valve VVÉR-440	Actuator drive
I	$r = 0.5 \text{ rad/h}$, $t = 45^{\circ}\text{C}$, $n = 90\%$	$r = 0.5 \text{ rad/h}$, $t = 40^{\circ}\text{C}$, $n = 90\%$	$r = 100 \text{ rad/h}$, $t = 50^{\circ}\text{C}$, $n = 90\%$	$r = 5 \cdot 10^5 \text{ mrad/h}$, $c = \text{force } 9$	$r = 5 \cdot 10^4 \text{ mrad/h}$, $c = \text{force } 9$	$r = 5 \cdot 10^4 \text{ mrad/h}$, $c = \text{force } 9$
		$t = 60-120^{\circ}\text{C}$, $p = (1.56 - 2.27) \cdot 10^{-4} \text{ Pa G}$	$t = 60-120^{\circ}\text{C}$, $p = (1.56 - 2.27) \cdot 10^{-4} \text{ Pa G}$	$t = 70-150^{\circ}\text{C}$, $p = 0.12-0.5 \text{ MPa A}$	$t = 70-127^{\circ}\text{C}$, $p = 0.12-0.25 \text{ MPa G}$	$t = 70-90^{\circ}\text{C}$, $p = 0.17 \text{ MPa G}$
P, kW	0,025					
	0,06					
	0,12					
	0,18					
	0,25					
	0,37					
	0,55					
v , r.p.m.	1000; 1500 3000	1500			1500; 1800	750; 900
f , Hz		50			50, 60	
L		1	2			3

Fig. 1. Classification of conditions of use of induction motors and their parametric series. Induction motor; t) temperature; n) relative humidity; p) pressure; r) radiation; c) earthquake resistance; P) power; v) speed; f) frequency; G) steam-gas mixture; A) steam-air mixture; I, II) rated and fault conditions of operation; L1, 2, 3) are operating conditions: S1) continuous, S2) intermittent; S4) continuous-intermittent.

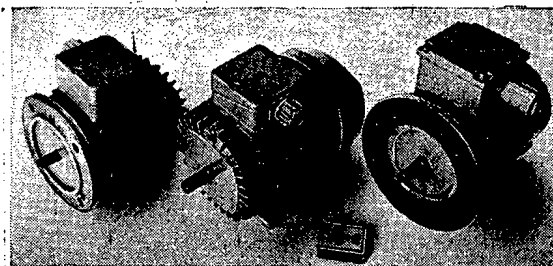


Fig. 2. Small induction motors for nuclear power stations.

tuators (particularly shut-off valves). The electromechanical time constant is found by means of expression

$$t_M = J (\omega_0 / M_k),$$

where J is the moment of inertia of the rotor, ω_0 is the angular velocity of the rotor, M_k is the starting torque of the motor.

A batch of motors has been manufactured and brought into operation on unit 5 at the Novovoronezh nuclear power station. Mass production has been organized by the Soyuzélektromash production association.

Analysis of the contract shows that the motors have been used on all power stations equipped with types VVER-440 and 1000 reactors. The demand for new types of motors is being studied. The stabilization of types ordered for nuclear power stations has enabled them to be classified according to their conditions of use and their basic size and parameter series (Fig. 1). Last, but by no means least, we have been able to unify all previously developed machines, thus reducing the number of different types in production to a minimum as far as is practicable. The design of the motors is illustrated in Fig. 2.

AUTOMATED SYSTEM FOR MAKING OBSERVATIONS, EVALUATIONS, AND FORECASTS: A FOUNDATION FOR COMPREHENSIVE PROTECTION OF THE ENVIRONMENT AND OF THE PUBLIC HEALTH

E. I. Vorob'ev, V. M. Prusakov,
and V. A. Minchenko

UDC 339

At the present stage of development of environmental protection and some related areas of this science, one of the most important problems is further development of the theoretical and scientific foundations of the system for controlling the quality of the environment in the interests of public health and maintenance of labor resources. Here, the problem of creating automated systems for protecting the environment in regions of large-scale industrial-power complexes becomes very important [1]. An analysis of the status of this problem shows that a great deal of attention is directed in this country and abroad [2-5] toward automating the observations and evaluations of the state of the environment on the one hand and of public health on the other. Most existing systems and most systems under development reflect only some one aspect of the interaction of man (or the source of the perturbation) with the environment. The problems involved in making comprehensive evaluations and forecasts of the action of industrial emissions on the environment, including the working environment and the state of public health, are solved extremely slowly. The methodological and conceptual foundations required for the solution of this problem have not yet been formulated.

In this connection, a special-purpose program for creating scientific (medical-health, technological, and mathematical) foundations of an automated system for protecting labor personnel, the environment, and public health in regions of large-scale industrial-power complexes ("Angara" program) has been developed and is being realized for one of the industrial cities of Siberia.

An analysis of domestic concepts of monitoring [6] permits representing the automated system for making observations, evaluations, and forecasts together with the organs and the object of control as one of the variants of the most advanced system for protecting the environment and the public health. In this respect, the system for making observations, evaluations, and forecasts is viewed as a means for providing the required reliable data to control organs in order to make decisions concerning regulation of the sources of environmental disturbance, the state of the environment, and the level of public health.

The object of the investigation and of control is a complicated system of interacting elements: production (source of action)-environment-public health. In its general form such a system must include the interacting elements mentioned above (A_1 , A_2 , and A_3 , respectively), the subsystems of factors determining the conditions of formation of the disturbance of the environment (B_1) and of man (B_2) and, finally, the factors affecting (controlling) the state and nature of the interaction of the basic elements of the system (C).

The distinguishing features of the automated information system (AIS) must be as follows: comprehensiveness of the estimates of the past, present, and future state of the sources of the disturbance of the environment and of the public health in developing solutions to problems;

Translated from Atomnaya Énergiya, Vol. 56, No. 3, pp. 149-153, March, 1984. Original article submitted April 8, 1983.

functional completeness of the AIS, including dynamic observation, evaluation, and forecasting of the state of the object of control;

availability of the required complex of technological and programmed means for performing the investigatory functions (data bank, software, and family of models);

orientation of the system toward revealing the possible spectrum of responses and, primarily, the primary (initial) diversions in the population under the action of harmful factors in the environment.

This constantly operating system must raise the effectiveness and validity of the control decisions adopted for protecting the living conditions and health of the population from undesirable actions of chemical pollution of the environment and other factors in regions of large-scale industrial-power complexes. To create such an AIS, a system for collecting data, data banks, and the means for analyzing and evaluating information as well as for modeling and forecasting is currently being actively developed (Fig. 1).

The main principle of information support in creating the data collection system is referral to stations for obtaining and concentrating information on the state of the public health, on the environment, on the work place, on the sources of environmental disturbance, and on social factors. This comprises a constantly operating subdivision of medical, analytical, and monitoring services of the city, factory, administrative and statistical institutions, etc. Plans are being made for obtaining information through the efforts of scientific-research subdivisions in performing experiments and for adjusting separate elements and problems of the system as well as the methodology. The required documentation is developed, adapted, and disseminated and the points of observation, population quotas, and periodicity of the data collection are selected.

The greatest difficulties in developing the system arose in formulating the indicators for observing the state of the public health. To overcome these difficulties we proposed a comprehensive approach, characterized by two basic features. First, our approach includes a wide spectrum of indicators, which presumes that judgements concerning the dependence of the state of the public health on environmental factors will be based on objective information on such characteristics as reproductive function, physical development, and functional activity of the organism, morbidity and mortality, and longevity in representative groups. In determining the indicators we used the recommendations and documentation from the N. A. Semashko All-Union Scientific-Research Institute of Public Health, the Institute of Medical Genetics of the USSR Academy of Medical Science, the Central Institute for Improving Doctors, and other organizations. Second, we combine the selection of already available indicators with the search for and development of new indicators, including fine indicators of changes in the health of the population, at both the individual and collective levels.

Thus a procedure for genetic monitoring is being developed following a special program together with the Institute of Medical Genetics of the USSR Academy of Medical Science. Based on a retrospective analysis of the dynamics of the frequencies of inherited pathology, a new method has been proposed for monitoring the process of mutation in man: observation of the dynamics of "units" of the inherited pathology, which reflect the contribution of new mutations and are easily incorporated into practical work [7].

Special attention is being devoted, in the system, to the development of a method for evaluating the state of individual health. For this purpose, a variant of the automated system of mass predactor examinations using a special automated complex is being introduced. A new scheme for medical examination, based on data obtained from questionnaires (anamnesis), inclusion of the frequency of consultation of doctors, and chronic pathology as well as instrumental examinations has been proposed. The system will permit estimating in a differentiated manner the state of health not only for the individual but also for separate groups of workers and will give a considerable economic savings due to a reduction of the time spent on medical examinations and the numbers of workers visiting a clinic. This will raise the functional level of the AIS under development up to the level of discovery of prepathological states as a foundation for requirements on the need for improvement of sanitary conditions. Other investigations, in particular immunological, are performed in order to search for informative tests of the state of adaptive-compensatory mechanisms.

An important element of the system under development is the data bank. The data bank of the Angara program, the composition of the integrated bases of which is shown in Fig. 2, is being designed to accept 60-270 million characters of diverse information per year. The

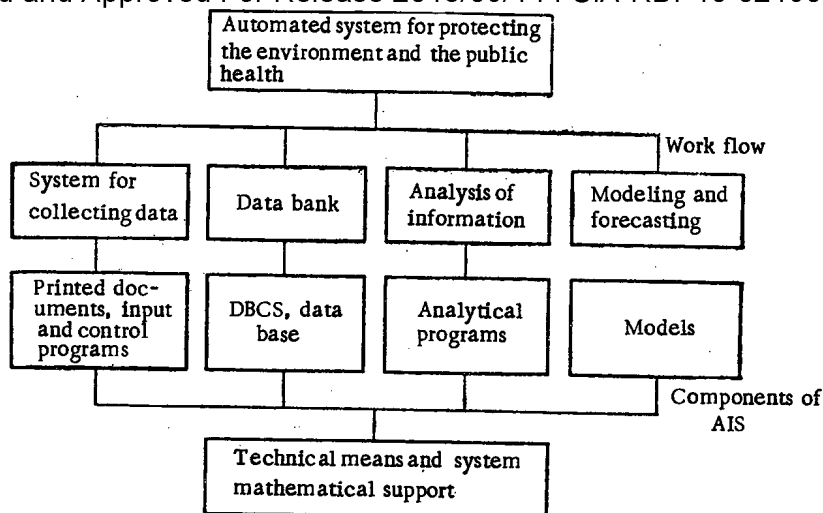


Fig. 1. Special-purpose structure of the mathematical and technical aspects of the "Angara" program: DBCS is the Data Base Control System.

bank presently includes the data base for sources of disturbance (sanitary-technical, chemical, physical, biological, nervous-emotional, and psychological); for the state of the working environment and of the atmosphere, water reservoirs, the quality of drinking water, and weather conditions; for social-economic (and food) factors, state of health of individuals and groups of individuals from data obtained by massive medical examinations and special physiological clinical examinations, stationary and dispensary observations, turnover, and demographic statistics as well as from data characterizing the reproductive function of the population. Information on the technological equipment and process, degree of heaviness, work stress and work regime, content of chemical and biological impurities in the air, in the working area, and on the skin of workers, physical and microclimatic factors, content of chemical and biological pollutants in the atmosphere and water, meteorological factors, living conditions, education, level of medical service, wages, professional course, duration and location of residents in the city, functional state of separate systems and of the organism as a whole, morbidity (including oncological), duration and termination of pregnancy, birth defects, physical and functional state of newborns and children, mortality, birth rate, migration, and other factors are incorporated as primary information into the data bank.

Based on the primary information, a large number of the so-called secondary indicators, which increase the working efficiency of data bank users, is formed. For example, based on printed documentation for taking into account the frequency with which workers seek medical help, more than 100 secondary indicators, which will become the primary hierarchy of the data bases required for solving practical and scientific problems, will be obtained. At the first stage, the health of twenty thousand workers in the leading industrial complex and forty thousand residents of all ages in two regions of the city (twenty-two thousand individuals in each region) with different content of pollutants in the air is monitored.

By virtue of the particularity of the problem being solved, related to the accumulation of a large amount of information, which is constantly being added to and changed, as well as to the structure of this information, a hierarchical model of data bases was chosen, and on this basis the hierarchical type system of control of data bases (DBCS) INES was chosen. In the system under development, the means of analysis and evaluation include software, matched with the technical, information, and program means, and a collection of solved problems and criteria for evaluating the information obtained and the results of the analysis. It is not useful to create a special program-algorithmic support for this type of system. It can be equated to the development of a special computer for such purposes. For this reason, the main path is to adapt existing software to the requirements of the specific system.

The process of developing the means for analyzing the program data is characterized by the need to perform the work with an incomplete determination of the list of problems to be solved. In other words, means must be provided for investigating any fragment of the data bases and any set of the data bases using all of the modern tools of mathematical statistics. For this reason, the determination and systematization of the basic types of problems is of fundamental importance in selecting the mathematical support based on classification of the starting data.

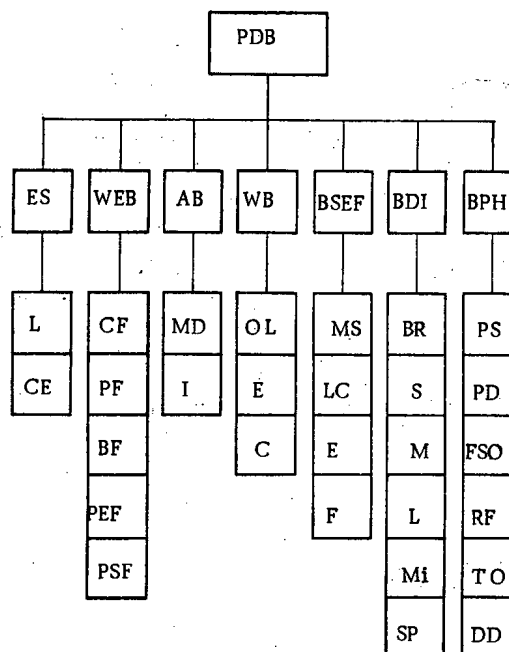


Fig. 2. System of data bases of the data bank for the Angara program: program data bank (PDB); data base for emission sources (ES); location (L); characteristics of emissions (CE); data base for working environment (WEB); chemical, physical, biological, psychoemotional, and psychosocial factors (CF, PF, BF, PEF, and PSF, respectively); atmospheric data base (AB); meteorological data (MD); content of impurities (I); data base for water (WB); organoleptic properties (OL); epidemiological danger (E); chemical impurities (C); base of social-economic factors (BSEF); level of medical service (MS); living conditions (LC); education (E); food (F); base of demographic indicators (BDI); birth rate (BR); still births (S); mortality (M); longevity (L); migration (Mi); structure of population (SP); base for data on the public health (BPH); passport-social information (PS); physical development (PD); functional state of the organism (FSO); reproductive function (RF); turnover (TO); data on deaths (DD).

According to their significance, all data can be referred to quantity, frequency, and grouping factors. Thus the indicators of the atmosphere, water, and working environment bases are the concentration levels, noise level, etc. The morbidity of population groups during a particular period of time is the frequency indicator; sex, place of work, and age are the grouping indicators. But this is not unique. In determining the chemical load on a person, the concentration of impurities is viewed as a quantity, but in characterizing the quality of work at the factory, from the point of view of protecting the environment, the same data over a definite period of time can be represented as the distribution of the frequency with which the measured quantities fall in the range up to 1 MPC (maximum permissible concentration), 1-5 MPC, 5-10 MPC, etc. Analogously, the grouping indicator can be used in some problems as a parameter. According to established ideas, the dynamic and statistical data are distinguished according to the forms of observation and the characteristics of the short-time or chronic phenomena, referred to different time intervals, are distinguished according to duration, etc.

In order to make possible a combined analysis of diverse data, the data are tied to the location and time of sampling with unified coding of the data for the Angara bank. The main means for performing the analysis is a packet of applied programs for processing biomedical information. Blocks are partially formed with the help of DBCS INES. The unification of blocks for combined analysis is provided for by the original program, which permits combining into a single realization the data from several blocks according to a set of coinciding indicators or indicators shifted by a constant number of digits. An example of such a problem is the search for a relation between morbidity and the state of the atmosphere during a particular period of time.

Based on the means indicated above, the set of problems that can be solved in the automatic regime on a computer is being investigated. Criteria are being formulated for evaluating the results. Since one of the main purposes of the system is to obtain differentiated estimates of indicators of the health and of the state of the environment, a complex of criteria for the health estimates is being created. It will include the following indicators (in order of decreasing significance): the actual danger, the potential danger, the special or objective indicators. The criteria of the actual danger are indicators of the changes in the state of health. The criteria of the potential danger are the experimentally established MPC and the indicators based on them. The special, or objective, criteria are the usual indicators.

The theoretical foundation of this proposal consists of presently established characteristics of low intensity: nonspecific nature of the actions due to a decrease in the resistance of the organism to different pathogenic factors; manifestation of such action on the population in a wide range of responses (from primary shifts to distinct harm) depending on the strength of the harmful effect.

The model which permits studying and evaluating the processes and consequences of the solutions adopted to various problems concerning the protection of the environment and of the public health in the production-environment-public health system must be the main element of the system. It is evidently now possible to develop a simulation model comprising a collection of different types of models, each of which realizes a specific goal: It demonstrates the behavior of separate aspects of the real system under the action of changes introduced into it. On the whole, they will reflect to some degree of completeness our knowledge of the entire system under study. This collection of models is being developed using a different language for expressing the models (block diagrams, matrices, mathematical and algorithmic description in the form of equations, mathematical operations, program description). The modeling is based on the conceptual model of the production (source of action)-environment-public-health system. The general structure of the model for computer realization, the general algorithm for forecasting public health, and the working model for forecasting in the pollution-source-air-basin-public-health (children) system has been developed.

During use of the AIS the models will be improved and enriched due to the internal content of separate subsystems and blocks. Analysis of the modeling has indicated the paths of development and improvement of the models. Based on the achievements of forecasting in science and technology, a series of assumptions for public health forecasting in the pollution-source-air-basin-public-health system have been developed.

Experience has shown that the guiding principle for carrying out the program is the use of modern concepts in the area of environmental protection and public health and their development; large-scale use and testing of the latest means for recording, collecting, storing, and analyzing information; practical application of the results obtained at the development stages, transmission, and dissemination of the elements of the system after they have been tested and used commercially (adoption).

Thus an automated information system for protecting the environment and public health is being developed. It is intended for studying the general and particular characteristics of the interaction of man and environment (adaptive-compensatory processes) at the system, individual, collective, and population levels, as well as for studying the relation between the environment and sources of pollution.

The development of a reasonable and efficient system requires that comprehensive medical-hygienic, social-hygienic, technical-mathematical and other forms of investigations be performed on both methodological and theoretical levels.

LITERATURE CITED

1. E. I. Vorob'ev and V. Yu. Reznichenko, *At. Energ.*, 50, No. 4, 234 (1981).
2. A. V. Primak and A. N. Shcherban', *Methods and Means for Monitoring Atmospheric Pollution* [in Russian], Naukova Dumka, Kiev (1980).
3. M. A. Murov and R. A. Uklonskaya, *Experience in a Number of Foreign Countries on the Application of Automated Systems for Controlling Hospitals and Mass Examinations of the Population* [in Russian], VNIIMI, Moscow (1974).
4. B. Mikhov et al., in: *Problems of Providing a Dispensary System for the Population* [in Russian], *Meditcina i Fizkul'tura*, Sofiya (1982), p. 171.

5. T. Schneider, in: Handbook on Monitoring Air Quality in Cities [in Russian], VOZ, Copenhagen (1980), p. 241.
6. Yu. A. Izrael', Ecology and Monitoring of the State of the Environment [in Russian], Gidrometeoizdat, Leningrad (1979), p. 375.
7. N. P. Bochkov et al., Tsitol. Genet., 16, No. 6, 33 (1982).

RADIOACTIVE CONTAMINATION OF THE SEA ENVIRONMENT NEAR THE LENINGRAD ATOMIC ENERGY PLANT IN 1982

S. M. Vakulovskii and A. I. Nikitin

UDC 551.464.6.02

The Baltic countries are utilizing on a large scale the coastal waters of the Baltic Sea for cooling the turbine condensers of atomic energy stations and for the disposal of liquid waste with low specific activity [1, 2]. In the USSR, the coastal waters of Kopor Bay in the Gulf of Finland are used as the cooling reservoir for the V. I. Lenin Leningrad Atomic Energy Plant (LAEP). The low-activity disbalance water from the plant is also discharged here [2]. The first unit of the plant incorporating an RBMK-1000 reactor was put into service in 1973, and three additional similar units were made operational in 1981 [1]. Thus, a considerable time interval has elapsed since the plant was put into operation, which permits us to draw conclusions concerning the effect of radioactive waste from LAEP on the radioactivity conditions in Kopor Bay.

Information on the radioactive contamination of biometers, mainly brown *Fucus* algae, caused by the operation of atomic energy plants was published recently [3, 4]. According to data from [5], the zone of contamination produced by waste from LAEP and detected by means of modern radiometry methods is limited to a radius of a few kilometers, while the contamination zone pertaining to algae of the biometer type has a radius of up to 15-20 km.

The Institute of Experimental Meteorology completed a field investigation of Kopor Bay in June 1982 in order to obtain data on the contamination level and the distribution of radionuclides from LAEP waste in the sea environment components. During the investigation, radionuclides were concentrated from samples taken from the coastal waters and from the open water area of Kopor Bay, and samples of bottom deposits and biometers (brown and green algae) were taken at points located at distances of up to 5.5 km from the LAEP. The position of the sampling points is shown in Fig. 1. Water samples were taken by means of the equipment described in [6, 7] with simultaneous separation of weighed matter and concentration of the radioactive impurity by means of a selective sorbent. A fibrous sorbent based on copper ferrocyanide was used for extracting the dissolved fraction [6]. The water was filtered through a combination filter consisting of FPP-15-1.5 fabric (first layer) and a "blue-ribbon" paper filter. After calcination at 350°C, the algae specimens, the sorbents, and the filters were measured by means of a semiconductor gamma-spectrometer incorporating a DGDK-80 detector. Samples of bottom deposits were measured in a similar manner after drying at 100°C.

The results obtained in determining the percentage of artificial γ -radiators in sea environment samples from Kopor Bay are given in Tables 1-3. It has been found that neutron activation products from LAEP waste are present in virtually all sea environment constituents in the samples taken. The observed level of contamination indicates that the plant has been operating in a normal manner during the period of time under consideration, which is readily seen by comparing the level of biometer contamination near the LAEP with the data pertaining to some of the atomic energy stations in other Baltic countries. Thus, at a distance of 1-2 km from the Lovisa atomic energy station, the concentration of induced radionuclides ^{60}Co and ^{54}Mn in brown *Fucus* algae amounted to 23-39 and 15-22 Bq/kg, respectively [4]. These values are only slightly below the level of contamination of similar biometers near the LAEP. It should be taken into account that the Lovisa atomic energy plant incorporates two units with VVER-440 reactors, which contaminate the environment to a lesser extent than channel-type reactors. The contamination level of brown *Fucus* algae at a distance of 1-2 km from the Swedish

Translated from Atomnaya Energiya, Vol. 56, No. 3, pp. 153-155, March, 1984. Original article submitted June 29, 1983.

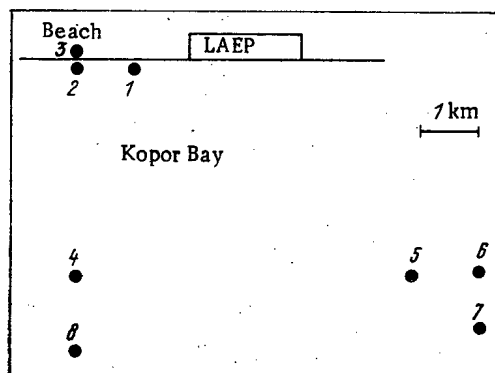


Fig. 1. Position of the sampling points near the LAEP.

TABLE 1. Percentages of ^{137}Cs and Neutron Activation Products in Biometers from Kopor Bay (samples taken on June 16, 1982), Bq/kg dry weight

Point No.	Distance from LAEP, km	Biometer type	$\frac{M_1}{M_2}$	^{54}Mn	^{60}Co	^{137}Cs
1	1	Green algae	0,12	12	54	22
2	2	Same	0,16	14	36	19
2	2	Brown algae	0,27	34	93	16

* M_1 and M_2 are the masses of dry and wet algae, respectively.

TABLE 2. Percentages of ^{60}Co and ^{137}Cs in Seawater from Kopor Bay, Bq/m

Point No.	Distance from LAEP, km	Sampling date	Type of sample	Vol. of sample, liters	^{60}Co	^{137}Cs
2	2	16.06.82	Suspension	1250	0,5	0,6
			Dissolved part	750	0,7	6,0
4	5	19.06.82	Suspension	2310	0,08	0,1
			Dissolved part	2170		4,0
5	5	20.06.82	Suspension	1720	<0,07	0,1
			Dissolved part	1720		4,0

Barsebeck atomic energy plant (two units with BWR-580 reactors) is higher: In 1977, it amounted to 200-500 and 30-80 Bq/kg for ^{60}Co and ^{54}Mn , respectively [3].

At the present time, the LAEP has produced no noticeable effect on ^{137}Cs contamination of the water and bottom deposits against the background of the existing global contamination. The concentration of ^{137}Cs in the bottom deposits of Kopor Bay does not exceed the radionuclide concentration in the bottom deposits of the open Baltic Sea and the Gulf of Finland, which, according to our data, amounts to 2-24 Bq/kg. The ^{137}Cs concentration in the algae which we measured is comparable to the radionuclide concentration in algae sampled in the Baltic at locations remote from the atomic energy station [8]. We have not observed a reduction in the ^{137}Cs concentration in the coastal bottom deposits with increasing distance from the LAEP, while the ^{60}Co percentage diminishes by a factor of 4 when the distance from the plant increases to 2 km.

TABLE 3. Content of ^{137}Cs and ^{60}Co in the Beach Sand and the Bottom Deposits of Kopor Bay

Point No.	Distance from LAEP, km	Sampling date	Depth, m	Bottom sampling depth, cm	Type of bottom	^{137}Cs		^{60}Co , Bk/m ²
						Bk/kg	Bk/m ²	
1	1	16.06.82	0,5	Surface layer	Sand	5	Not determined	6
2	2	16.06.82	0,5	Same	Same	4	Same	1,5
3	2	16.06.82	Beach	" "	" "	5	" "	1,6
5	5	20.06.82		" "	" "	<1,5	" "	<1,5
6	5	20.06.82	10	" "	Sand, gravel	<1,5	" "	<1,5
7	5,5	20.06.82	10	0-2	Sand	1,8	80	<1,5
				2-4	Silty sand	<1,5	30	<1,5
8	5,5	20.06.82	10	0-2	Same	7	230	<1,5
				2-4		4	110	<1,5

The contamination of the bottom deposits is concentrated within a 2-km radius from the LAEP. No ^{60}Co was detected in the bottom deposits of the open water area of Kopor Bay. The data obtained on the ^{60}Co distribution between water and suspended matter indicate that this radionuclide probably spreads at locations remote from the plant, mainly with suspended matter. Thus, the dissolved ^{60}Co fraction was not found at a distance of 5 km from the LAEP in the open part of Kopor Bay (point 4). Unfortunately, the degree to which ^{60}Co is sorbed by our sorbent, which has been developed mainly for cesium extraction from seawater, has not been investigated to a sufficient extent. The simulator experiments that have been carried out have shown that the sorbent extracts not more than 50% of the amount of radionuclide introduced. We used this value in calculations, and the thus-determined concentration of ^{60}Co dissolved in coastal waters should be considered as a minimum value.

The measured concentrations in the aqueous phase were used for determining the ^{137}Cs accumulation factor and estimating the ^{60}Co accumulation factor for sea algae. The ^{137}Cs accumulation factor amounts to 450-510 for green and 700 for brown, algae; the ^{60}Co accumulation factor does not exceed 8700 and 35,000 for green and brown algae, respectively.

LITERATURE CITED

1. A. M. Petros'yants, Nuclear Power Engineering [in Russian], Nauka, Moscow (1981).
2. L. A. Buldakov et al., Radiation Safety in Atomic Power Engineering [in Russian], Atomizdat, Moscow (1981).
3. S. Mattsson, R. Finck, and M. Nilsson, Environ. Pollut., B1, No. 2, 105 (1980).
4. E. Ilus et al., *Fucus vesiculosus* as Bioindicator of Radioactivity in Finnish Coastal Waters. Part 1, Gulf of Finland, STL-B-TUTO 14, Institute of Radiation Protection, Helsinki (1981).
5. D. I. Gusev et al., in: Abstracts of Reports at the Second International Conference of Member Countries of the Council of Mutual Economic Aid on Ensuring Radiation Safety in the Operation of Atomic Power Plants. Vilnius, May 18-23, 1982 [in Russian], p. 93.
6. S. M. Vakulovskii et al., in: Abstracts of Reports at the Second International Conference of Member Countries of the Council of Mutual Economic Aid on Ensuring Radiation Safety in the Operation of Atomic Power Plants, Vilnius, May 18-23, 1982 [in Russian], p. 61.
7. E. G. Tertyshnik et al., Tr. Inst. Eksp. Meteorol., No. 5(94), 65 (1980).
8. R. Boyanovski and Ch. Pémpoviyak, in: Interaction between Water and Living Matter (Transactions of an International Symposium, Odessa, 1975) [in Russian], Vol. 2, Moscow (1979), p. 193.

NEUTRON INSPECTION OF MOISTURE IN SLIGHTLY ENRICHED UO_2

V. V. Frolov, V. I. Bulanenko,
and V. V. Charychanskii

UDC 539.1.074.8

One of the conditions of successful operation of enterprises producing fuel for atomic power plants is to ensure nuclear safety. If enrichment with ^{235}U amounts to less than 5-6%, the critical mass of anhydrous uranium compounds is infinite. However, in practice, media containing hydrogen, which is an efficient neutron moderator, are used for producing UO_2 from UF_6 , so that the criticality conditions are potentially attainable. The presence of hydrogen in UO_2 powder is due to various causes: sorption of air moisture, addition of a hydrogen-containing plasticizer before cake pressing, or deviation from the technological conditions. The probability of breaks in the water supply lines used for UO_2 cooling in certain technological operations must also be taken into account in providing for nuclear safety.

If the degree of enrichment and the density of UO_2 are known, one can readily determine the constraints to be imposed on the equipment geometry or the moisture percentage in order to ensure nuclear safety. The geometric constraints (a volume of not more than 50 liters or a form of equipment providing a large neutron leakage surface) can readily be effected and checked. However, they are often unacceptable for economic reasons or because of technological factors (for instance, using moist UO_2 in filling or emptying tubular or flat apparatus is extremely difficult, in contrast to similar operations with liquid media). In certain cases, it is more advisable to use equipment with nuclear-hazardous geometry and limit the hydrogen concentration in UO_2 , using an inspection method satisfying the main requirements: sufficient sensitivity and accuracy, rapidity, possibility of automation, and elimination of contact between the data unit and UO_2 . These requirements are satisfied by the method presented below, which is based on moderating fast neutrons with hydrogen nuclei.

Figure 1 shows the theoretical value of the critical mass M_{cr} of a sphere with a complete aqueous reflector as a function of the moisture W in UO_2 with a density of 3 g/cm^3 , enriched with ^{235}U by 2, 3, and 5% [1]. According to these data, if $W \leq 3\%$, the criticality conditions cannot be achieved by using industrial equipment and UO_2 with a density $\leq 3 \text{ g/cm}^3$ and enrichment $\leq 5\%$ with respect to ^{235}U , since $M_{\text{cr}} > 20$ tons. Thus, in order to ensure nuclear safety, it is sufficient that the lower moisture measurement limit W_{min} be equal to 0.5% and that the warning signal threshold $W_{\text{thr}} \sim 2-3\%$. At the same time, the volume (or diameter) of the measuring container must be chosen so that it can be charged with UO_2 containing any percentage of moisture. According to nuclear safety rules, the neutron multiplication factor K_n in the measuring container filled with UO_2 powder must be smaller than 10-20 for the highest moisture content; however, in the range of actual moisture values, 0.5-3%, it was found that $K \leq 1.5-2$. The method developed is based on the irradiation of the inspected medium with high-speed neutron radioisotope sources (Pu-Be , ^{252}Cf) and recording the moderated neutrons.

It has been found experimentally that the sensitivity of the method is the same for diverse sources, such as Pu-Li and Pu-Be . Sources with a yield of $\sim (1-5) \cdot 10^5$ neutrons/sec and high-efficiency detectors with ^{10}B (two SNM-11 counters; Fig. 2a) or with ^3He (four SNM-18 counters; Fig. 2b) were used to ensure the required count statistics and limit irradiation of the personnel.

The other parameters affecting the sensitivity and accuracy of the method are the density of UO_2 powder, the reflector type and thickness, nonuniformity of moisture distribution in the measuring container, the geometry of the source and neutron detector arrangement, and the temperature. Experimental and theoretical data confirming the efficiency of the method for solving problems of moisture inspection in UO_2 were obtained for most of these parameters.

The secondary measuring equipment includes a mass-produced RPS2-01 radiometer or an industrial Neutron-3M hygrometer. For enrichment with ^{235}U of less than 2%, the safe diameter

Translated from *Atomnaya Energiya*, Vol. 56, No. 3, pp. 155-157, March, 1984. Original article submitted June 20, 1983.

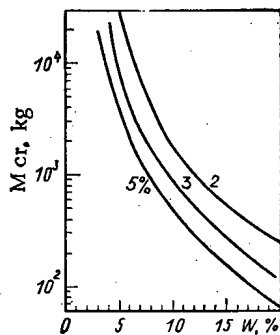


Fig. 1

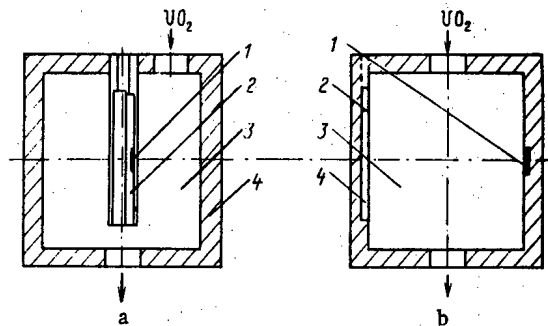


Fig. 2

Fig. 1. Critical mass of UO_2 in the form of a ball with a complete aqueous reflector as a function of the moisture percentage. The figures at the curves pertain to enrichment with respect to ^{235}U .

Fig. 2. Schematic diagrams of two experimental devices. 1) Pu-Be source; 2) SNM detectors; 3) uranium dioxide; 4) nickel reflector.

of the cylindrical container is equal to 40 cm. The height of the UO_2 specimen with which the device is charged must be comparable to the container diameter, but not smaller than the length of the neutron counters used. The measuring container is surrounded with a nickel or steel reflector, provided with the necessary technological through passages.

Standard specimens with UO_2 containing moisture in the $0 \leq W \leq 10\%$ range are prepared by careful mixing of known amounts of UO_2 and H_2O and are then analyzed by drying the samples taken before and after an experiment. The error in determining the moisture percentage in a sample does not exceed $\pm 1-2$ rel.% for $W = 1\%$. Throughout the investigated moisture range, the measuring equipment based on the method of sample drying has an accuracy exceeding by more than one order of magnitude the accuracy of neutron inspection equipment, which makes it possible to use the former as standard equipment in relation to the latter. This condition is necessary, but it may be insufficient if representativeness of the samples is not assured. Therefore, the samples with UO_2 are taken from different places in the measuring container, representing both radial and azimuthal moisture distributions. Each sample is subsequently divided into three parts, which are analyzed independently of each other.

Figure 3 shows the counting rate of two SNM-11 detectors as a function of the moisture in UO_2 for the geometry shown in Fig. 2a. The density of UO_2 is equal to 3 g/cm^3 , while the nickel or steel reflectors have different thicknesses. These data lead to important conclusions: The use of reflectors is a necessary condition for utilizing successfully the moisture inspection method in the $0.5 \leq W \leq 3\%$ range; the efficiency of a nickel reflector is higher than that of a steel reflector, which has also been confirmed by theoretical estimates. A nickel reflector thickness of $\sim 5 \text{ cm}$ is sufficient with regard to the required sensitivity and economic considerations.

We represent the counting rate of the detector N as a function of the moisture W in the following form:

$$N = N_b + S_w W,$$

where N_b is the detector's background counting rate, and S_w is the sensitivity of the equipment used.

Assuming that the relative inspection error is $\Delta W_{\min}/W_{\min} = \pm 100\%$ for a confidence interval of 99.7% (3σ test) and $N_b t_{\text{mea}} \gg 1$, where W_{\min} is the lowest measured value of moisture, and t_{mea} is the measurement duration, we obtain

$$W_{\min} \approx \frac{3.2 \sqrt{N_b t_{\text{mea}}}}{S_w t_{\text{mea}}}.$$

On the basis of the data in Fig. 3 (curve 6), we have for $W = 1\%$ the values $S_w \approx 15 \text{ pulses} \cdot \text{sec}^{-1}/1\%$ and $N_b \approx 30 \text{ pulses/sec}$. Thus, for $t_{\text{mea}} = 10 \text{ sec}$, $W_{\min} \approx 0.3\%$.

Figure 4 shows the relationships obtained for the geometry shown in Fig. 2b. The height of the measuring container in the form of a rectangular prism is equal to 60 cm, the size of

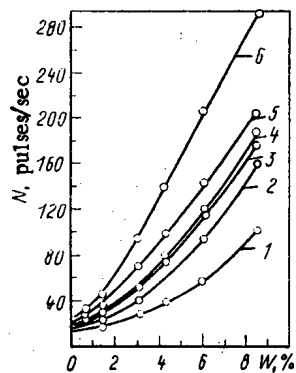


Fig. 3

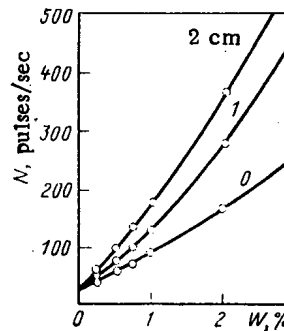


Fig. 4

Fig. 3. Neutron counting rate as a function of the moisture in UO_2 for different reflectors. 1) Without reflector; 2, 4) stainless steel, thickness 2.5 and 5 cm, respectively; 3, 5, and 6) nickel, thickness 2.5, 5, and 10 cm, respectively.

Fig. 4. Counting rate of SNM-18 counters as a function of the moisture percentage. The figures at the curves pertain to the thickness of the nickel reflector behind the counters.

the base is 26×26 cm, while the thickness of the nickel reflector is equal to 4.5 cm; however, on the side where the counters were located, the thickness was varied from 0 to 2 cm. The results show the considerable advantages of the geometry where the source and the detectors are separated by the UO_2 specimen to be inspected: For equal thicknesses of the nickel reflector, the sensitivity of the method increases by more than one order of magnitude; the effect of possible nonuniformities in the moisture distribution becomes negligible; the possibility of placing a large number of counters on the sides of the measuring container makes it possible to obtain a large number of readings and ensure analog tapping of data from the radiometer with a small integration constant.

It is of interest to consider the effect of the density γ on the results of measurements of moisture in UO_2 . The size of particles and the density of bulk UO_2 vary, depending on the production technology (wet or dry method). The range of actual γ values is equal to 2-3 g/cm³ [2]. Relative density fluctuations amounting to $\Delta\gamma/\gamma = \pm 10\%$ have been observed in practice. It has been found experimentally that $(\Delta N/N)/(\Delta\gamma/\gamma) \leq 1$ for the geometry shown in Fig. 2b and a container diameter of 10 cm. This error component of the method can be taken into account by an independent density check, for instance, using a radioisotope densimeter. As the diameter of the measuring container increases from 10 to 30 cm, the error $(\Delta N/N)/(\Delta\gamma/\gamma) = 0.3$ becomes comparable to that of gamma-densimeters. Therefore, it can be neglected for purposes of nuclear safety if we introduce a suitable margin with respect to the actuation threshold of warning signals. The following expression is used for determining the lower value of the actuation threshold Π_{act} :

$$\Pi_{\text{act}} = \Pi_{\text{all}} / [1 + (\Delta/100)],$$

where Π_{all} is the actuation threshold corresponding to the allowable moisture percentage based on nuclear safety norms (%), and Δ is the total relative error of moisture inspection corresponding to Π_{all} (%).

Under actual, stable operating conditions of measuring devices, the temperature does not greatly affect the inspection error.

In conclusion, the authors are grateful to L. V. Diev, B. G. Ryazanov, V. N. Gurin, V. S. Vnukov, V. A. Lapshin, and L. V. Zhilin for their interest in this project and their support.

LITERATURE CITED

1. L. V. Diev et al., Critical Parameters of Fissionable Materials and Nuclear Safety. Manual [in Russian], Énergoatomizdat, Moscow (1984).
2. A. K. Kruglov and Yu. V. Smirnov (eds.), Atomic Industry in Foreign Countries [in Russian], Atomizdat, Moscow (1980).

AVERAGE CHARACTERISTICS OF THE SLOWING DOWN OF LOW-ENERGY ELECTRONS IN A TISSUE-EQUIVALENT MATERIAL

V. A. Pitkevich

UDC 577.3:539.12.04

Studies of the characteristics of the stochastic process of electron slowing down in matter are not only of independent interest, but also are widely applicable, since the secondary electrons shape the spatial distribution of absorbed energy of ionizing radiations in matter. The transmission of electrons can be considered a random branching process where a set of "trees" at whose branch points secondary, tertiary, etc., electrons are created in ionization processes. By employing information on total and differential cross sections for the interaction of electrons with the atoms comprising a tissue-equivalent material ($C_{1.5}N_{0.43}O_{4.06}H_{10}$ [1]), the Monte Carlo method can be used to describe in detail all the characteristics of the process under study. Grosswendt [2] studied the slowing down of 30 eV-5 keV electrons in a tissue-equivalent gas (64.4 vol.% CH_4 , 32.4 vol.% CO_2 , 3.2 vol.% N_2). The transmission of electrons in nitrogen and oxygen was studied in [3-5], and the transmission of electrons with $E > 2$ keV in [6-8]. Slowing down in water vapor, nitrogen, and air was studied in [9-11], in water in the condensed state for $E < 30$ keV in [12], and in a tissue-equivalent material for $20 \text{ eV} < E < 30 \text{ keV}$. The accuracy of the cross sections used and the modeling method were tested by comparing the calculated average values of the characteristics of the slowing down process with experimental data. There are few such data for low-energy electrons. For this reason an estimate of the quality of the modeling algorithm is closely related to the quality of the cross sections used. The rather complete set of cross sections proposed in [13] permits a satisfactory description of the spatial, angular, and energy characteristics of elastic and inelastic interactions of slow electrons with a tissue-equivalent material.

In the present article we calculate the average characteristics of the slowing down of electrons in a tissue-equivalent material, compare them with experimental data, and analyze the possibility of employing the concepts of "range" and "average loss of energy" per unit path length in problems involving the transmission of low-energy electrons through matter. The parameters of the "tree" describing the transmission of an electron of energy E in a tissue-equivalent material were modeled by the Monte Carlo method in accordance with data in [13].

Suppose a narrow beam of N_0 electrons per cm^2 per sec is incident normally along the z axis on a plane layer of material of thickness Δz . For any value of Δz , N_{ref} of the electrons are reflected from the layer, N_{abs} are absorbed in the layer, and N_{tr} are transmitted through the layer. Because of branching, the sum $N_{ref} + N_{abs} + N_{tr}$ may be larger than N_0 . We denote by k_{ref} , k_{abs} , and k_{tr} , respectively the backscattering, absorption, and transmission coefficients. Figure 1 compares our calculated dependence of k_{tr} on $\Delta z/R_{95}$ for a tissue-equivalent material with experimental data [14] for a tissue-equivalent gas and with calculations [15] for water vapor. At the present time the thickness of a layer $\Delta z = R_{95}$ for which $k_{tr} = 0.05$ is conventionally considered to be equal to the "range" of nonrelativistic electrons. The difference between the experimental and calculated values in Fig. 1 is due both to the approximations in the calculations and to experimental errors. We note that for $\Delta z < 0.3R_{95}$ the value of k_{tr} may be larger than unity because of branching of the electron trajectory.

Figure 2 shows R_{95} as a function of E together with experimental data for a tissue-equivalent gas [14] and for a colloidal film [16]. Our results are in good agreement with data in [16] over the whole energy range investigated, and with data in [14] for $E > 100$ eV. In the modeling of the transmission of electrons through a tissue-equivalent material with a density of 1 g/cm^3 , the concept of a minimum mean free path l_0 [13] of an electron before a collision was used as a parameter approximately taking account of the phase state of the slowing-down medium. Good agreement with data in [16] was obtained for $l_0 = 0.3 \text{ nm}$. For this reason our calculated values of R_{95} for $E < 100$ eV are larger than the experimental values [14] obtained

Translated from *Atomnaya Energiya*, Vol. 56, No. 3, pp. 158-162, March, 1984. Original article submitted July 12, 1983.

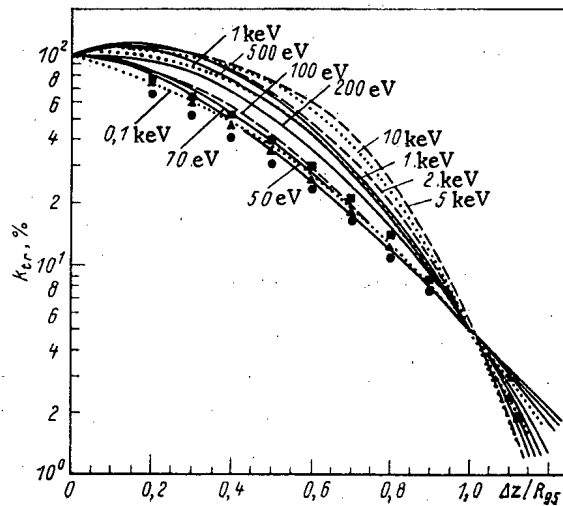


Fig. 1. —) Transmission coefficient k_{tr} as a function of $\Delta z/R_{0.5}$ for electrons of various energies: ●, Δ, ■) data from [14] for a tissue-equivalent gas and $E = 0.1, 0.5$, and 2 keV, respectively; ...) calculated values [15] for water vapor.

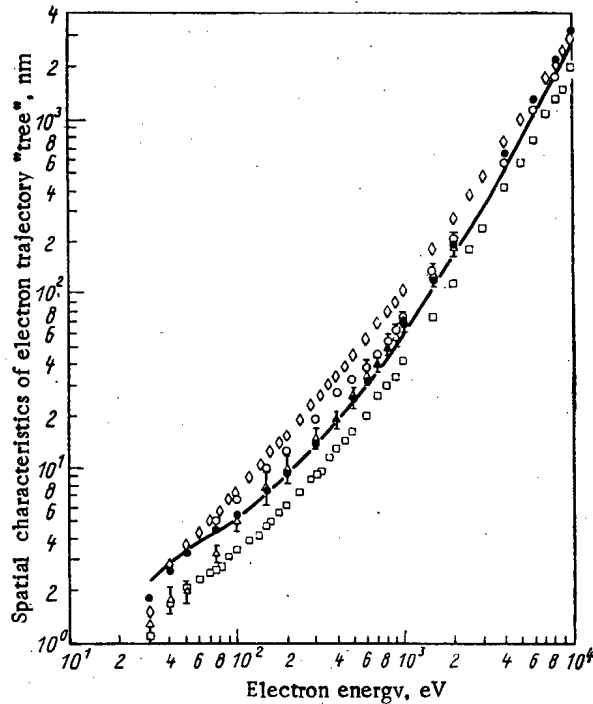


Fig. 2. —) range $R_{0.5}$; ○, mean length of "tree" without "branches"; ◇, mean length of "tree" with "branches"; □) distance between point of entrance into material and point of slowing down to 20 eV as functions of electron energy; Δ, ●) experimental values of $R_{0.5}$ for a tissue-equivalent gas and a colloidal film [14, 16].

in the gaseous phase and formally reduced to a material density of 1 g/cm^3 . Figure 2 also shows the energy dependence of the mean length of a "tree" with "branches" and without "branches," from which it follows that branching is substantial in the range $0.2 < E < 6$ keV. At higher energy the ratio of the mean length of the "branches" to the total length of a "tree" decreases, since the probability of substantial energy transfers in one collision is inversely proportional to the energy transfer. Figure 2 also shows $R_{end}(E)$, the average distance between the point where the electron is created and the point at which it has been slowed down to $E = 20$ eV. The ratio S_{wb}/R_{end} , where S_{wb} is the average length of a

"tree" without "branches" can be taken as a measure of the distortion of the trajectory. For an increase of E to 1 keV, S_{wb}/R_{95} decreases slowly from 2 to 1.8, and then to 1.25 as $E \rightarrow 10$ keV. For $E > 30$ keV the value of S_{wb} is close to R_{95} . Taking this into account, we can assume that for $E > 30$ keV the continuous slowing-down approximation can be used to describe the slowing-down of electrons to ~ 10 keV.

Data on the energy spectra of electrons reflected from a layer and those passing through it, and also on the spectra of the energy absorbed in the layer will be published in another of our papers. Figure 3 shows only data on the average energy of reflected electrons E_{ref}/E , the average absorbed energy E_{abs}/E , and the average energy E_{tr}/E of electrons behind the layer as functions of $\Delta z/R_{95}$ for various E . For small $\Delta z/R_{95}$ the electrons reflected from the layer have experienced mainly only elastic collisions. The ratio E_{ref}/E decreases with increasing energy. It is interesting that for $\Delta z/R_{95} < 0.5$ we can write

$$E_{abs}/E = k(\Delta z/R_{95}), \quad (1)$$

where k is a constant approximately equal to unity.

It is clearly more convenient to calculate E_{abs} by the above relation than by using the concept of average specific energy losses dE/dx . In the first place it was obtained from detailed calculations of E_{abs} , taking account of all the fundamental processes characterizing the slowing down of electrons, and secondly, in Eq. (1) it was not assumed that all the secondary electrons are absorbed at the point where they are created. Conventionally dE/dx is defined as the integral over the differential cross sections for the interaction of charged particles with matter. It is easy to measure dE/dx for heavy charged particles in experiments with thin layers of slowing-down material, since in this case elastic scattering is unimportant over a wide energy range, the particle trajectory is rectilinear, and the layer is thick enough to absorb the δ electrons. It is practically impossible to perform similar measurements correctly for low energy electrons, although dE/dx has been calculated in various approximations in a large number of papers, and values are recommended by the ICRU. To measure dE/dx it is necessary to use a set of slowing-down films no thicker than $0.1R_{95}$, to find the dependence of E_{abs} on Δz , and then to determine dE/dx . Even under these conditions, however, some of the electrons are reflected from the layer, and there is a high probability of a large energy loss even in such thin layers. For $\Delta z/R_{95} \approx 0.1$ the value of k_{ref} reaches 10-15%. The above assumptions are confirmed both experimentally [17] and by the values we obtained in numerical experiments. We note in passing that the experimental values of dE/dx in [16] were found by differentiating the relation $R_{95}(E)$, but no justification was given for their correspondence to the generally accepted definition. We obtained satisfactory agreement of the results of our numerical experiment with the calculated values of dE/dx only by taking account of events with zero energy transfer, not taking account of events in which the energy transfer was more than $0.1E$, and assuming that all the secondary electrons are absorbed in the layer. Thus, the use of the theoretical concept of dE/dx in determining the energy absorption of low-energy electrons in volumes of material with characteristic dimensions 1-1000 nm cannot be considered admissible. Nevertheless, this concept is widely employed in biophysical modeling of the radiation damage of cells and subcellular structures, and in other fields of science.

In view of the large value of k_{ref} ($\max k_{ref} \approx 30\%$), the strong distortion of the trajectories, and the presence of branching, it is inadvisable to use the concept of range (either R_{95} or R_{csda} — the range in the continuous slowing-down approximation) to describe the slowing down of low energy electrons in matter. For $E < 10$ keV the value of R_{95} is unsuitable even for rough estimates of the possibility of an electron reaching one or another point of the medium when its initial direction of motion is known. This same conclusion can be drawn concerning the concept of R_{csda} . It is useful in investigating the slowing down of heavy charged particles and high energy electrons when a characteristic linear dimension of the region of strong distortion of the trajectory is much smaller than R_{csda} .

When an electron is completely stopped in matter, \bar{n}_{ion} ionized atoms and \bar{n}_{ex} excited atoms are formed (\bar{n}_{ion} and \bar{n}_{ex} are random quantities). The average values \bar{n}_{ion} and \bar{n}_{ex} and their variances $(\sigma_{ion}^2, \sigma_{ex}^2)^{1/2}$ are shown in Fig. 4 as functions of the electron energy. For $E > 100$ eV the indicated parameters vary practically linearly with energy. At $E \approx 2$ keV, however, there is a deviation from linearity as a result of the fact that in this range the cross sections for the ionization of the K shells of C, N, and O atoms reach a maximum, and the contribution of Auger electrons is most pronounced, although also insignificant. The Fano factor shown in Fig. 4 is given by the formula

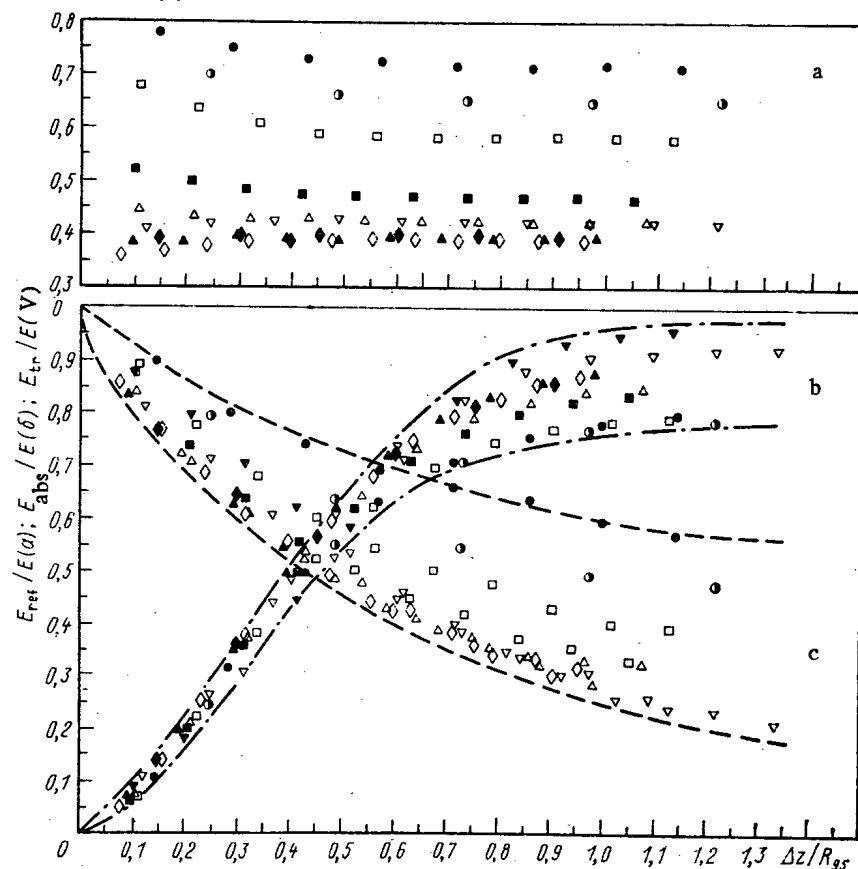


Fig. 3. a) Average energy of electrons reflected from a plane layer of tissue-equivalent material; b) average energy absorbed in layer (bounded by dash-dot curves); c) average energy of electrons behind layer (bounded by dashed curves) as functions of $\Delta z/R_{95}$ for the following electron energies: \bullet) 0.05; \circ) 0.07; \square) 0.1; \blacksquare) 0.2; Δ) 0.3; \blacktriangle) 0.5; \diamond) 0.7; \blacklozenge) 1.0; ∇) 2.0; \blacktriangledown) 5.0 keV.

$$F = \sigma_{\text{ion}}^2 / \bar{n}_{\text{ion}}. \quad (2)$$

The dashed curve represents data from [18] for water vapor obtained by the Monte Carlo method. The Fano factor characterizes the relative fluctuations of the number of ion pairs, and for $E > 200$ eV it is practically independent of energy. It increases at lower energy, but should not be greater than $3/4$ [19], which does not agree with data in [18] for which F approaches unity.

Figure 5 shows our calculated values of $W = W_{\text{ion}} = E/\bar{n}_{\text{ion}}$ and experimental data for a tissue-equivalent gas [14, 20, 21]. The calculated values are in good agreement with data in [14, 20], but differ from the values in [21] for low E . This difference is accounted for by the fact that we used a mixture of noninteracting atoms as a slowing-down medium, while a tissue-equivalent mixture of molecular gases was used in the experiments. The dash-dot curve of Fig. 5 shows the values of W^* , defined as $\langle E/n \rangle$ (average over events in which $n \geq 1$). In this case as E decreases to the ionization potential, W^* approaches zero; at $E \approx 100$ eV it is maximum, and for $E > 500$ eV it practically coincides with W defined in the conventional way (Fano factor is minimum). The dashed curve shows the dependence of the average energy \bar{W}_{ex} expended per excitation of atoms of the medium. For $E > 40$ eV the value of \bar{W}_{ex} is practically constant, and for $E > 300$ eV it is somewhat larger than W . We can write

$$W = \bar{e}_{\text{ion}} + (p_{\text{ex}}/p_{\text{ion}}) \bar{e}_{\text{ex}}; \quad (3)$$

$$W_{\text{ex}} = \bar{e}_{\text{ex}} + (p_{\text{ion}}/p_{\text{ex}}) \bar{e}_{\text{ion}}, \quad (4)$$

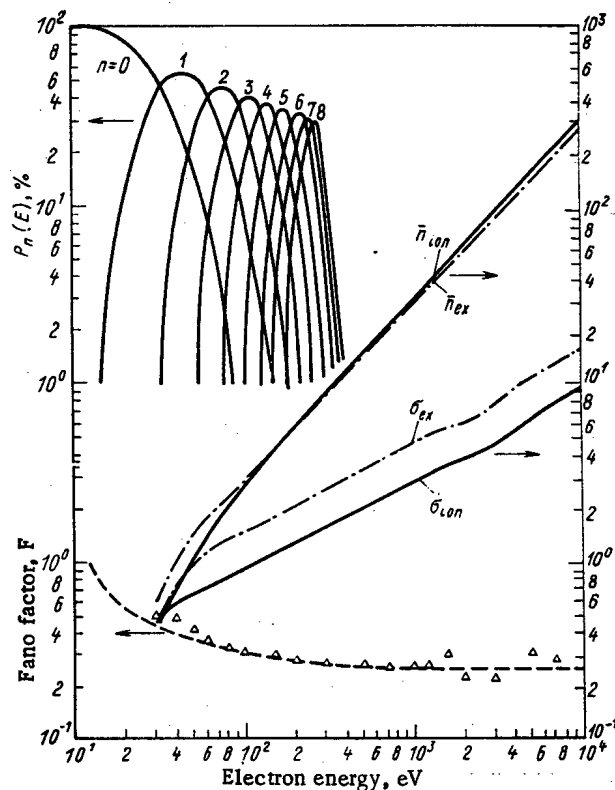


Fig. 4. Average number of ionizations \bar{n}_{ion} and excitations \bar{n}_{ex} and their variances σ_{ion} , σ_{ex} during the complete stopping of an electron in a tissue-equivalent material (right-hand scale); F) Fano factor; Δ) our calculation; -----) data from [18]. The curves in the upper part of the figure show the probability $p_n(E)$ ($n = 1, \dots, 8$) of the formation of n ion pairs when an electron is completely stopped in matter.

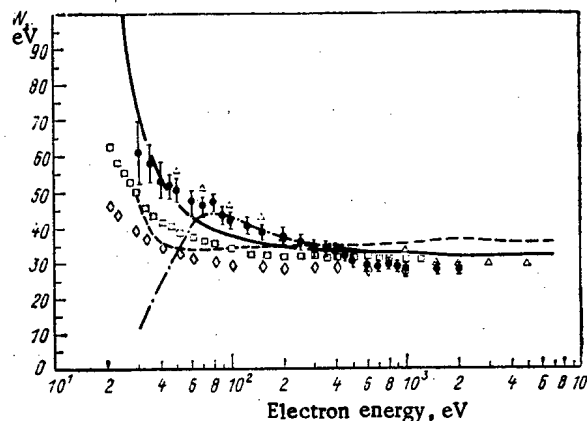


Fig. 5. —) Average energy of ion formation W ; ----) average energy for excitation; -.-) calculated values of $W^* = E/n$; Δ , \bullet) experimental values of W cited in [14, 20] for a tissue-equivalent gas; \square , \diamond) data from [21] for a tissue-equivalent gas based on methane and propane.

where $\bar{\epsilon}_1^{ion}$ and $\bar{\epsilon}_1^{ex}$ are, respectively the average energy expended per ionization and per excitation (19.6 and 13.9 eV in the plateau region); p_{ion} and p_{ex} are the fractions of the total number of inelastic collisions with energy losses $\bar{\epsilon}_1^{ion}$ and $\bar{\epsilon}_1^{ex}$, respectively (0.527 and 0.47 in the plateau region). These relations are useful for analyzing the contributions to W and W_{ex} from various inelastic processes.

The calculated average values of the characteristics of the slowing down of slow electrons and the comparison with experimental data indicate that the modeling algorithm described in [13] is adequate for solving a wide range of radiation physics problems related to the correct description of the transmission of slow electrons. The use of the "range" and "average specific energy loss" concepts in such problems is evidently inadmissible.

LITERATURE CITED

1. J. Bevan, in: Proc. First Symp. on Microdosimetry, Brussels (1968), p. 161.
2. B. Grosswendt, in: Proc. Seventh Symp. on Microdosimetry, Vol. 1, Brussels-Luxembourg (1981), p. 319.
3. B. Grosswendt and E. Waibel, in: Proc. Sixth Symp. on Microdosimetry, Vol. 1, London (1978), p. 311.
4. B. Grosswendt and E. Waibel, Nucl. Instrum. Methods, 155, 145 (1978).
5. M. Terrissol, J. Fourmenty, and J. Potau, in: Proc. Fifth Symp. on Microdosimetry, Vol. 1, Brussels-Luxembourg (1976), p. 393.
6. K. Maeda, Atmos. Terr. Phys., 27, 259 (1965).
7. M. Berger, S. Seltzer, and K. Maeda, *ibid.*, 32, 1015 (1970).
8. M. Berger, S. Seltzer, and K. Maeda, *ibid.*, 36, 59 (1974).
9. M. Berger, in: Proc. Second Symp. on Microdosimetry, Luxembourg (1969), p. 541.
10. M. J. Berger, in: Proc. Fourth Symp. on Microdosimetry, Vol. 2, Luxembourg (1973), p. 695.
11. H. Paretzke, *ibid.*, Vol. 1, p. 141.
12. M. Terrissol and J. Patau, [2], p. 411.
13. V. A. Pitkevich, V. G. Videnskii, and V. V. Duba, At. Energ., 52, 190 (1982).
14. B. Smith and J. Booz, [3], Vol. 2, p. 759.
15. H. Paretzke, G. Leuthold, and W. Wilson, Extended Abstract for the Meeting of European Dosimetry Group, Dundee, April 10-11 (1979).
16. A. Cole, Rad. Res., 38, 7 (1969).
17. H. Iskef, D. Twaites, and D. Watt, [2], Vol. 1, p. 201.
18. H. Paretzke and M. Berger, [3], Vol. 2, p. 749.
19. U. Fano, Phys. Rev., 63, 222 (1946); 70, 20 (1947).
20. A. Waker and J. Booz, in: Proc. Second Symp. on Neutron Dosimetry in Biology and Medicine, Luxembourg, EUR-5452 (1975), p. 455.
21. D. Combecher, Rad. Res., 84, 189 (1980).

MEASUREMENT OF THE RATIO OF THE FISSION CROSS SECTIONS

OF ^{238}U AND ^{235}U FOR NEUTRON ENERGIES IN THE RANGE

5.4-10.4 MeV

A. A. Goverdovskii, B. D. Kuz'minov,
V. F. Mitrofanov, A. I. Sergachev,
S. M. Solov'ev, P. S. Soloshenkov,
and A. K. Gordyushin

UDC 539.185

The main raw material in making nuclear fuel is ^{238}U , so that the nuclear constants of this isotope must be known very reliably. In accordance with the international list of required nuclear data [1], the error in the ratio of the fission cross sections of ^{238}U and ^{235}U nuclei (σ_f^8/σ_f^5) for reactor applications constitutes 2% with a neutron energy of 5-10 MeV. The disagreements in the results of measurements obtained in different laboratories with neutron energies exceeding 5 MeV reach 10-15%. This circumstance makes it necessary to obtain additional independent experimental data on σ_f^8/σ_f^5 .

In this work, we measured the fission cross sections of ^{238}U and ^{235}U nuclei on the ÉGP-OM electrostatic charge-exchange accelerator at the Physical Power Institute, operating in the pulsed mode with a repetition frequency of 5 MHz. The average deuteron current on target

Translated from Atomnaya Énergiya, Vol. 56, No. 3, pp. 162-164, March, 1984. Original article submitted March 15, 1983.

TABLE 1. Isotopic Composition of Uranium Targets (%) and the Results of Measurements of the Ratio of the Fission Cross Sections of ^{238}U and ^{235}U Nuclei with 7.3-MeV Neutrons*

Target number	^{235}U	^{236}U	^{238}U	σ_f^8/σ_f^5
1	$99,992 \pm 0,001$	$0,004 \pm 0,0005$	$0,020 \pm 0,0005$	—
2	$6,864 \pm 0,007$	$0,020 \pm 0,002$	$93,116 \pm 0,007$	$0,583 \pm 0,006$
3	$3,213 \pm 0,010$	$0,007 \pm 0,002$	$96,78 \pm 0,01$	$0,584 \pm 0,006$

*Content of ^{233}U and ^{234}U is negligibly small.

TABLE 2. Results of Measurements of Fission Cross Section of ^{238}U and ^{235}U Nuclei

E_n , MeV	ΔE_n , MeV	σ_f^8/σ_f^5	Error, %	
			statistical	total
5,44	0,15	0,491	0,83	1,56
5,64	0,14	0,521	1,03	1,69
5,89	0,14	0,548	1,00	1,68
6,14	0,13	0,575	0,90	1,59
6,38	0,12	0,597	0,89	1,59
6,50	0,12	0,601	0,80	1,52
6,61	0,11	0,609	1,13	1,72
6,84	0,11	0,620	1,20	1,76
7,07	0,10	0,598	1,20	1,76
7,19	0,10	0,581	0,90	1,57
7,30	0,10	0,584	0,20	0,68
7,52	0,10	0,576	1,21	1,77
7,74	0,09	0,572	0,86	1,55
7,96	0,09	0,570	1,20	1,77
8,17	0,09	0,564	1,16	1,74
8,33	0,08	0,570	0,91	1,58
8,49	0,08	0,562	0,90	1,56
8,65	0,08	0,555	0,80	1,52
8,81	0,08	0,569	0,87	1,56
8,97	0,08	0,565	0,87	1,56
9,12	0,07	0,557	1,30	1,83
9,28	0,07	0,568	0,81	1,53
9,44	0,07	0,556	0,78	1,51
9,59	0,07	0,560	0,80	1,52
9,80	0,07	0,559	1,05	1,67
10,00	0,07	0,578	0,85	1,55
10,41	0,06	0,567	1,05	1,67

was 1.2 μA with a current pulse duration of about 1 nsec. The reaction $\text{D}(\text{d}, \text{n}) {}^3\text{He}$ served as the source of neutrons. A gaseous deuterium target — a cylinder with a diameter of 10 mm and a length of 40 mm — was used. The output window of the target was a molybdenum foil 17 μm thick. A platinum foil with a surface density of 200 $\text{mg}\cdot\text{cm}^{-2}$ was fastened to the bottom of the cylinder. The deuterium pressure in the target was $1.18 \cdot 10^5$ Pa.

The fission fragments were recorded with a fast double ionization chamber. The target foils consisting of the fissioning isotopes were placed orthogonally to the direction of the neutron flow. The chamber was filled with argon with a 10% addition of carbon dioxide gas at a pressure of $1.8 \cdot 10^5$ Pa. The distance between the electrodes in the chamber was 2 mm. The construction of the chamber included the necessity of decreasing the scattering material to a minimum. In the measurements, we used layers of uranium oxide whose thicknesses varied from 200 to 500 $\mu\text{g}\cdot\text{cm}^{-2}$ on thin aluminum substrates.

We simultaneously measured two temporal and two amplitude spectra of the fission fragment pulses. The amplitude spectra of the pulses were used to determine the efficiency with which the fission fragments were recorded. The loss of counts created by the fission fragments in the chamber constituted ~1%. The temporal spectra permitted separating out fission events due to the background neutrons. The ultimate temporal resolution was ~3 nsec. The transit

baseline of the neutrons (50 cm) was chosen so as to achieve a maximum rate of fissioning in the uranium targets while retaining the possibility of separating the primary and background neutron groups. The starting pulses were the current pulses created in the ionization chamber by the fission fragments. The stop signal entered from the output of the master oscillator determining the frequency of the system forming the pulsed ion current.

In the course of the measurements, the ^{238}U and ^{235}U targets were practically in an identical neutron flow. To eliminate the effects due to the finite distance between the ^{238}U and ^{235}U layers and the blocking of one layer by the other, we performed the measurements with two positions of the chamber. In one position, the ^{238}U layer was turned toward the neutron source and in the other the ^{235}U layer was turned toward the source. The results obtained were averaged. In this case, the influence of kinematic effects on the efficiency with which the fission fragments were recorded was likewise eliminated.

We performed the measurements in two stages. The first stage involved the determination of the energy dependence of the ratio of the fission cross sections of ^{238}U and ^{235}U . For this, we used layers with high isotopic purity (99.99%). At the second stage we performed the absolute normalization of the dependence obtained. In this case, the ^{238}U target contained an impurity of ^{235}U nuclei. We determined the ratio of the numbers of ^{235}U and ^{238}U nuclei (η) in the target by a mass spectrometrical method. We determined the ratio of the number of ^{235}U nuclei in the ^{238}U target and the number of nuclei in the pure ^{235}U target from the count of the fission acts in the thermal neutron flow. Taking into account the difference in the efficiency with which the fission fragments were recorded in the two chambers, we can write:

$$\sigma_f^8/\sigma_f^5 = \left[\left(\frac{n_8}{n_5} \right)^f \left(\frac{n_5}{n_8} \right)^t - 1 \right] \eta,$$

where $n_{5,8}$ is the number of fission acts in the ^{235}U and ^{238}U layers in the flow of fast and thermal neutrons.

We performed the normalization with a neutron energy of $E_n = 7.3$ MeV using two ^{238}U targets with different impurity concentrations of ^{235}U nuclei (Table 1).

In analyzing the results of the measurements, we took into account a number of effects, which either distorted the quantity being measured or decreased the reliability of the value of σ_f^8/σ_f^5 obtained: incomplete recording of fission acts due to the finite level of the amplitude discrimination (δ_1) and the total stoppage of some of the fragments in the target itself (δ_2); scattering of neutrons by the substrates of the targets (δ_3); scattering of neutrons by structural parts of the chamber (δ_4); fissioning of impurity isotopes (δ_5); analysis of the peak of basic neutrons on a temporal scale (δ_6); error in normalizing the curve of the energy dependence of σ_f^8/σ_f^5 (δ_7).

We present below the typical corrections (A) introduced into the final results and the errors corresponding to them (B), %:

	A	B
δ_1	1	0.74
δ_2	0.5	0.05
δ_3	0.05	<0.05
δ_4	0.15	<0.15
δ_5	<0.1	<0.1
δ_6	—	0.1
δ_7	—	1.1

The relative fraction of fission events caused by background neutrons, forming as a result of the interaction of deuterons with the structural materials of the gaseous target, was determined experimentally in measurements with an empty target. It turned out to be negligibly small.

The results of measurements of the ratios of the fission cross sections of ^{238}U and ^{235}U nuclei are presented in Table 2.

The results of this work and [2-7] are compared in Fig. 1. In the entire range of E_n investigated, there is good agreement between the data obtained here and in [3, 7], with the exception of some values of σ_f^8/σ_f^5 in the energy range 5.5-6 MeV. The results obtained in this work are lower than the results in [6] and higher than the results in [3] in practically the entire energy range.

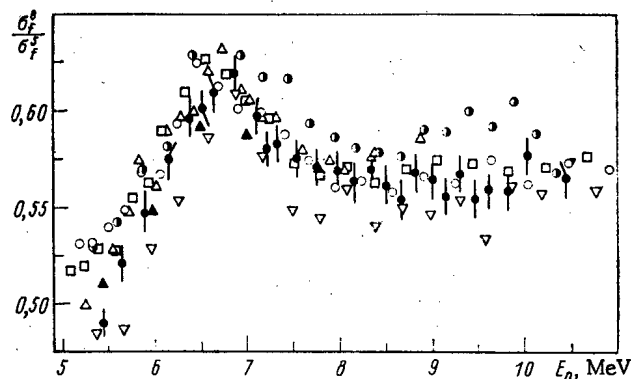


Fig. 1. Energy dependence of the ratio of the fission cross section of ^{238}U and ^{235}U nuclei: Δ) data from [2]; ∇) [3]; \blacktriangle) [4]; \square) [5]; \bullet) [6]; \circ) [7]; \bullet) this study.

The authors are deeply grateful to N. N. Semenova for preparing and adjusting some of the electronic blocks and to N. V. Kornilov and A. M. Trufanov for help in performing the measurements.

LITERATURE CITED

1. WREDA 81/82, World Request List for Nuclear Data, Nuclear Data Section, Vienna, IAEA (1981).
2. C. Nordborg, H. Conde, and L. Stroemberg, in: Proc NEANDC/NEACRP Specialists Meeting on Fast Neutron Fission Cross Sections of ^{233}U , ^{235}U , ^{238}U , and ^{239}Pu , ANL-76, 90, 128 (1976).
3. S. Cierjacks, B. Leungers, and K. Kari, *ibid.*, p. 94.
4. M. Cance and G. Grenier, *ibid.*, p. 141.
5. F. Difilippo and R. Perez, Nucl. Sci. Eng., **68**, No. 1, 43 (1978).
6. J. Meadows, *ibid.*, **58**, No. 2, 255 (1975).
7. J. Behrens and G. Carlson, *ibid.*, **63**, 250 (1977).

MEASUREMENT OF THE FISSION CROSS SECTION OF ^{238}U AND ^{235}U NUCLEI BY 14 MeV NEUTRONS

A. A. Goverdovskii, A. K. Gordyushin,
B. D. Kuz'minov, A. I. Sergachev,
S. M. Solov'ev, and P. S. Soloshenkov

UDC 539.185

Experimental data on the cross section of fissioning of ^{238}U nuclei by neutrons with energies close to 14 MeV are of direct practical significance, and such data are also critical for testing theoretical models, because both equilibrium and nonequilibrium nuclear processes are realized in this energy range. The data obtained by independent methods in different laboratories permit judging objectively the reliability of the experimental results.

In this work, we measured the ratio of the fission cross sections of ^{238}U and ^{235}U nuclei σ_F^8/σ_F^5 in the energy range 13.8–14.7 MeV. The reaction $T(d, n)^4\text{He}$ served as the source of neutrons. We obtained a pulsating beam of deuterons, accelerated to an energy of 250 keV, on the KG-0.3 accelerator. The fission fragments were recorded with a double ionization chamber, in which we positioned the ^{238}U and ^{235}U targets. The total temporal resolution with which the fission fragments were recorded constituted ~ 6 nsec. The background neutrons were distinguished from the main group of neutrons according to their transit time. The distance from the uranium targets up to the neutron source was 15 cm. To change the energy E_n

Translated from *Atomnaya Energiya*, Vol. 56, No. 3, pp. 164–165, March, 1984. Original article submitted March 15, 1983.

TABLE 1. Results of Measurements of the Ratio of the Fission Cross Sections of ^{238}U and ^{235}U Nuclei

E_n , MeV	ΔE_n , MeV	σ_f^8/σ_f^5	Error, %	
			statistical	total
13,82	0,15	0,528	1,0	2,3
14,12	0,13	0,554	0,7	2,2
14,47	0,20	0,559	0,7	2,2
14,64	0,23	0,553	0,7	2,2
14,76	0,19	0,543	0,7	2,2

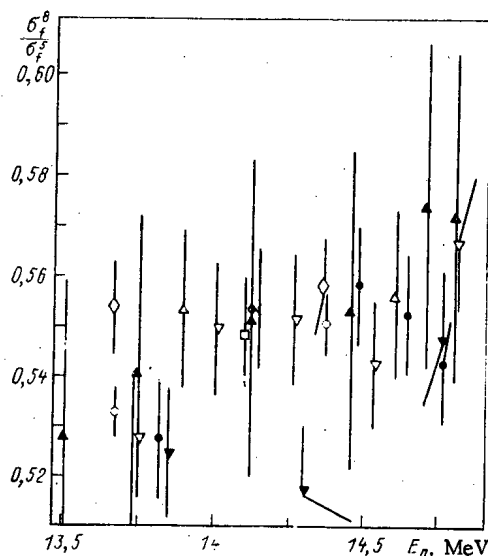


Fig. 1. Ratio of the fission cross sections of ^{238}U and ^{235}U nuclei with neutron energies close to 14 MeV: \blacktriangle) data in [1]; Δ) [2]; \blacktriangledown) [3]; ∇) [4]; \circ) [5]; \diamond) [6]; \square) [7]; \bullet) this study.

of the neutrons producing the fissioning of the nuclei, we performed the measurements at different angles relative to the direction of motion of the deuterons. We constantly monitored the energy spectrum of the neutrons using a time-of-flight spectrometer with a baseline of 6 m. We prepared the ^{235}U target from a material with an isotopic purity of 99.99%; the ^{238}U target had a ^{235}U impurity, whose quantity $\alpha = 7\%$ was determined to within 1%. The thickness of the targets constituted $0.4 \text{ mg} \cdot \text{cm}^{-2}$. We determined the ratio of the numbers of ^{238}U and ^{235}U nuclei by weighing the targets in the flow of thermal neutrons using the data on the isotopic composition of ^{238}U target. We simultaneously measured the temporal and amplitude spectra of the fission fragment counts, which permitted determining the efficiency with which the fission fragments were recorded and the contribution of the background neutrons. In measuring the ratio of the numbers of events involving fissioning of ^{238}U and ^{235}U nuclei, we placed both targets in practically identical neutron flow. Without taking into account the various corrections the ratio of the fission cross sections of ^{238}U and ^{235}U nuclei is determined from the expression

$$\sigma_f^8/\sigma_f^5 = \left[\left(\frac{n_8}{n_5} \right)^f \left(\frac{n_5}{n_8} \right)^t - 1 \right] \frac{\alpha}{1-\alpha},$$

where $n_{8,5}$ is the number of fission events of nuclei in ^{238}U and ^{235}U targets in the fluxes of fast and thermal neutrons.

The results of the measurements, together with a number of corrections, are presented in Table 1. The corrections take into account the following effects: difference in the neutron fluxes on the ^{238}U and ^{235}U targets (δ_1); difference in the efficiencies with which the fission fragments of ^{238}U and ^{235}U nuclei were recorded (δ_2); reliability of the determina-

tion of the ratio of the numbers of ^{238}U and ^{235}U nuclei (δ_3); difference in the absorption of fragments in layers due to angular distributions of fragments and motion of the center of mass (δ_4); scattering of neutrons by the substrates of the targets (δ_5); scattering of neutrons by the structural elements of the chamber (δ_6); error in analyzing the experimental information (δ_7); background from reactions with emission of charged particles (δ_8).

We present below the corrections introduced into the results of the measurements (A) and the errors corresponding to them (B), %:

	A	B
δ_1	4	0.2
δ_2	10	1.4
δ_3	—	1.5
δ_4	0.2	0.02
δ_5	0.04	0.004
δ_6	0.05	0.005
δ_7	—	<0.1
δ_8	<0.01	<0.01

The results of this work and the work of others [1-7] are compared in Fig. 1. The experimental data on the ratios of fission cross sections of ^{238}U and ^{235}U nuclei in the energy range 13.9-14.8 MeV, as a whole, indicate the existence of a plateau at the 0.55 level. In the energy range 13.5-13.9 MeV, most results are concentrated near the value 0.53.

LITERATURE CITED

1. M. Varnagy and J. Csikai, Nucl. Instrum. Methods, 196, 465 (1982).
2. M. Cance and G. Grenier, Nucl. Sci. Eng., 68, 197 (1978).
3. M. Coates, D. Gayther, and N. Pattenden, in: Proc. 4th Conf. on Nuclear Cross Sections and Technology, Washington (1975), Vol. 2, p. 568.
4. S. Cierjacks et al., in: Proc. NENDC/NEACRP Specialists Meeting on Fast Neutron Fission Cross Sections of ^{233}U , ^{235}U , ^{238}U , and ^{239}Pu , ANL-76, 90, 94 (1976).
5. F. Difilippo and R. Perez, Nucl. Sci. Eng., 68, No. 1, 43 (1978).
6. J. Behrens and G. Carlson, ibid., 63, No. 3, 250 (1977).
7. P. White and G. Warner, J. Nucl. Energy, 21, 671 (1967).

"GAS TARGET" IN THE DIVERTOR OF A TOKAMAK

M. Z. Tokar'

UDC 621.039.667

Experiments on the PDX, ASDEX, and D-III tokamaks [1] have shown that the use of a divertor is an effective means of combatting contamination of a plasma with nonhydrogen impurities. In the ASDEX machine [2], for example, discharges were obtained in which the energy lost through radiation by the impurities in the working volume of the tokamak did not exceed 10-15% of the power input into the discharge. Moreover, the main part of the thermal flux moving through the separatrix into the divertor layer is carried into the divertor chamber. In a fusion reactor the α particles and unburnt fuel which appear during the fusion reaction (to maintain the required low concentration of helium ash it is necessary that the fuel input substantially exceed the depletion [3]) will also be directed to the divertor.

If the reactor thermal fluxes are completely removed to neutralization plates, technical difficulties should arise [4]. Hence the great interest in the divertor operating regime realized in the ASDEX tokamak [5] and which has been dubbed a "gas target": On entering the divertor, the thermal flux is substantially dissipated in the gas filling that fills the evacuation chamber.

In this paper we propose a model for the description of processes occurring in the divertor. This model is a development of the one proposed earlier in [6] and permits a satisfactory explanation of the distinctive features of discharge in ASDEX in gas-target regimes.

Translated from Atomnaya Énergiya, Vol. 56, No. 3, pp. 165-172, March, 1984, Original article submitted August 5, 1983.

The model takes account of the broad spectrum of neutrals which enter the plasma from the neutralization plates and from the evacuation chamber, makes allowance for the radiative recombination of ions and electrons, makes a self-consistent determination of the characteristic size of the changes, the average values of the plasma density and temperature in the divertor layer, etc. The calculations carried out in this paper show that such regimes with a gas target can be realized in a reactor under certain conditions. The numerical calculations were based on the divertor scheme given in Fig. 1. The conclusions can be generalized, however, to more complex configurations (with segments with two open surfaces in the evacuation chamber, etc.).

Neutrals. Neutrals, atoms and molecules, have a strong influence on the plasma of the divertor. As shown in [7], the plasma parameters depend essentially on the energy of the atoms entering it. The entire spectrum of neutrals present in the divertor of the tokamak must thus be taken into account. One of the main causes of the neutrals is neutralization of the plasma on the collector plates. The result of the interaction of ions or neutrals possessing an initial energy ϵ with the surface of a solid can be the following: reflection in the form of atoms possessing an energy ϵ' , the probability $R(\epsilon, \epsilon')$ of this process also depending on the angle of incidence and the mass and atomic numbers of the incident particles and the target atoms [8]; adsorption, thermalization, and recombination of atoms and molecules (the probability ρ of a molecule leaving the solid as a result of diffusion depends on the degree of its saturation with gas); and surface ionization of the neutrals and reflection of ions without neutralization. At energy values of interest for consideration the last processes are insignificant.

In the plasma, molecules are ionized and dissociated into Franck-Condon atoms with an energy $\epsilon_F \approx 3-4$ eV. In the case of ionization, molecular ions are formed, their motion in the x direction being damped by the magnetic field. Henceforth, therefore, we assume that the loss of neutral molecules leads directly to the formation of one-nuclear ions and Franck-Condon atoms with isotropic velocity distribution functions. The fraction g of the latter depends on the plasma temperature.

The surface and bulk recombination of charged particles, reflection of neutrals from the neutralization plates and the walls of the evacuation chamber, charge exchange in ions, and molecular decomposition result in a wide spectrum of atoms appearing in the plasma. Each component of this spectrum is characterized by an average energy ϵ . Estimates show that in the divertor plasma collisions between neutrals can be neglected and ϵ does not vary with the passage of atoms and molecules of the plasma layer.

At small angles α between the magnetic field and the plate the behavior of neutrals in the divertor plasma can be described on the basis of one-dimensional kinetic equations for the velocity distribution functions f (the coordinate ξ along the plate is cyclical; $|v_x \frac{\partial f}{\partial x}| \gg |v_y \frac{\partial f}{\partial y}|$, since v_x and v_y are of the same order of magnitude, and the ratio of the characteristic dimensions of the variation of f along y and x is $\sim \alpha$). When integrated over v_y and v_ξ , these equations have the form

$$v_x \frac{\partial f_m}{\partial x} = -(k_1 + k_2) n f_m; \quad (1)$$

$$v_x \frac{\partial f_a(\epsilon)}{\partial x} = -[k_3 + k_4(\epsilon_i + \epsilon)] n f_a(\epsilon) + \varphi_i \frac{n}{2} \left[k_5 n + \sum_{\epsilon'} \int_{-\infty}^{\infty} dv'_x k_4(\epsilon_i + \epsilon') f_a(\epsilon') \right] + (k_1 + k_2) g n \varphi_F n_m, \quad (2)$$

where k_1 and k_2 are the ionization and dissociation coefficients of the neutral molecules, k_3 and k_4 are the ionization and charge-exchange coefficients of the atoms, k_5 is the radiative recombination coefficient, ϵ_i is the average ion energy, and n_m is the molecular density. The distribution functions of the Franck-Condon atoms, formed in the decomposition of molecules, and of the ions are assumed to be two-velocity distribution functions:

$$\varphi_{i,F} = \delta(v_x - V_{i,F}) + \delta(v_x + V_{i,F}); \\ V_\alpha = \sqrt{4\epsilon_\alpha / 3\pi m_\alpha}.$$

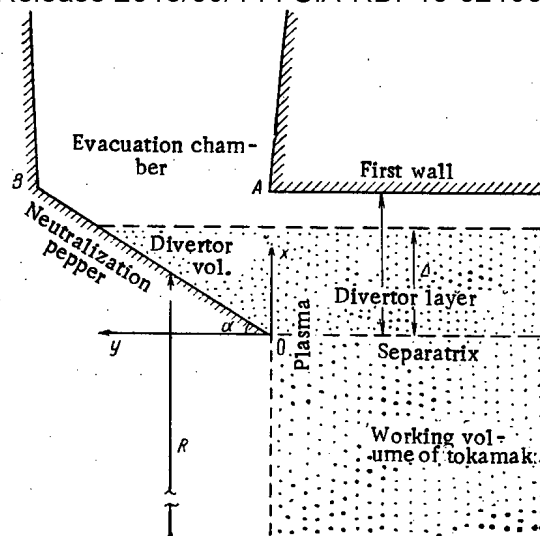


Fig. 1. Divertor scheme.

The validity of this approximation for φ_i was considered in [9]. For atoms and molecules, entering the plasma from the plates from the evacuation chamber, the distribution functions are assumed to be one-velocity functions of v_x . The solution of Eqs. (1) and (2) is sought in the form

$$f_{m,a} = \frac{A_{m,a}^+}{V_{m,a}} \delta(V_{m,a} - v_x) + \frac{A_{m,a}^-}{V_{m,a}} \delta(V_{m,a} + v_x)$$

For atoms formed during charge exchange this approach is applicable if their range $l \approx V_i/n \cdot \sqrt{k_3(k_3 + k_4)}$ [9] is small in comparison with the characteristic size of the change δ_T in the plasma temperature. The system of equations for the coefficients $A_{m,a}$ is given in the Appendix (Sec. 1). The boundary conditions of Eqs. (A1) are determined from the matching of the fluxes of charged and neutral particles on the plate ($x = s = y \tan \alpha$):

$$\begin{aligned} A_a^+(s, \epsilon) &= A_i(s) R(\epsilon_p, \epsilon) + \sum_{\epsilon'} A_a^-(s, \epsilon') R(\epsilon', \epsilon); \\ A_m^+(s) &= \rho_p \left(A_m^-(s) + \frac{1}{2} \left\{ \left[1 - \sum_{\epsilon} R(\epsilon_p, \epsilon) \right] A_i(s) + \sum_{\epsilon} \left[1 - \sum_{\epsilon'} R(\epsilon, \epsilon') \right] A_a^-(s, \epsilon) \right\} \right), \end{aligned} \quad (3)$$

where ρ_p is the desorption coefficient of the molecules for the conditions of the neutralization plate, A_i is the flux of neutrals from the plate which are formed during the neutralization of ions, and $\epsilon_p = \epsilon_i + e\phi$ is the energy of ions interacting with the plate, determined with allowance for the acceleration of the ions under the effect of the floating potential.

In order to formulate the boundary conditions (1) and (2) for $x = \delta$ we consider the behavior of neutrals in the evacuation chamber. Two limiting cases can be distinguished. The first corresponds to the situation in which the density of molecules in the pumping chamber is so high that the range of atoms leaving the plasma is small in comparison with the size of the pumped space. The atoms "disappear" as a result of bulk recombination in the molecule and surface effects can be neglected. In this case the neutrals entering the plasma from the evacuation chamber are represented mainly by molecules, whose density n_m^0 is determined by the balance of particle

$$2\pi R m_0 \int_0^\delta \left[A_m^+(\delta) + \frac{1}{2} \sum_{\epsilon} A_a^+(\delta, \epsilon) \right] ds = n_m^0 \{ V_m [S_l + S_b + S_w (1 - \rho_w)] + \tilde{V} \},$$

where S_l and S_w are the areas of the surface of the plasma layer and the walls of the evacuation chamber, ρ_w is the desorption coefficient of the molecules for the conditions of the walls, and m_0 is the number of divertor chambers. We have also allowed for the fact that gas from the evacuation chamber can also be pumped off by pumps or can enter the discharge chamber of the tokamak if the width of the plasma layer is small in comparison with the width of

the divertor "neck" or if some sort of by-pass channels exist. The effective volume pumping rate by the pumps (with allowance for hydraulic drag) and the cross section of the by-pass channels are denoted by \bar{V} and S_b , respectively.

The boundary conditions (A1) in the given case have the form

$$A_n^-(\delta, \varepsilon) = 0; \quad A_m^-(\delta) = n_m^0 V_m. \quad (4)$$

The opposite limiting case, in which the range of the atoms is large in comparison with the size of the evacuation chamber, is considered in the Appendix (Sec. 2).

Plasma. The plasma is described separately for the divertor volume and the main part of the divertor layer with subsequent joining at the boundary between them. As shown by estimates, in the divertor volume for a large range of parameters cross transfers of heat and plasma particles due to diffusion and thermal condition can be neglected. The hydrodynamic equations for the plasma in this case, on the whole, have the form

$$\sin \psi \frac{\partial}{\partial y} [n(V_{\parallel}^2 + V_s^2)] = - \sum_{\varepsilon \neq \varepsilon_i} k_{\varepsilon} n_{\varepsilon}^e n V_{\parallel} + k_3 n_{\varepsilon}^e n V_{\parallel}; \quad (5)$$

$$\sin \psi \frac{\partial n V_{\parallel}}{\partial y} = n \left[n_m^2 (1 - g) (k_1 + k_2) + k_3 \sum_{\varepsilon} n_{\varepsilon}^e - k_5 n \right]; \quad (6)$$

$$\sin \psi \frac{\partial q_{\parallel}}{\partial y} = n \left[\sum_{\varepsilon} n_{\varepsilon}^e [k_{\varepsilon} (\varepsilon - \varepsilon_i) + k_3 (\varepsilon - I_a)] - n_m [k_2 I_d + k_1 (I_m + I_d^+)] - k_5 (2\varepsilon_i + I_a) n \right] - Q_{im}, \quad (7)$$

where $n_{\varepsilon}^e = \int f_{\varepsilon}(\varepsilon) dv_x$, I_a and I_m are "chains" of ionization (with allowance for excitation) of atoms and molecules, I_d and I_d^+ are the dissociation energies of molecules and molecular ions, respectively, Q_{im} is the specific radiated power of the impurities $q_{\parallel} = -\sin \psi \kappa_{\parallel} \partial T / \partial y$, and ψ is the angle between the magnetic field and the planes $y = \text{const}$. Here and in what follows the plasma is considered to be isothermal and to have the temperature T . In this case the main contribution to κ_{\parallel} is made by the longitudinal electronic thermal conductivity and the speed of ionic sound is $V_s = \sqrt{2T/m_i}$. In the derivation of Eq. (5) we have taken account of the fact that "friction" is absent between the plasma and atoms formed during charge exchange. The boundary conditions of Eqs. (5)-(7) for $x = s$ (at the plate) are determined by the relations [10, 11]

$$V_{\parallel}(s) = V_s; \quad q_{\parallel}(s) = n V_{\parallel}(s) [2.5 (\alpha_e + \alpha_i) T + e\Phi], \quad (8)$$

where the coefficients $\alpha_{e,i}$ take account of a possible anomaly (due to secondary effects) of heat transfer to the surface of the plate.

The fluxes of the heat Q_0 and the plasma particles in the divertor are given,

$$2\pi R m_0 \int_0^{\delta} \frac{n V_{\parallel}}{q_{\parallel}} (y=0) \sin \psi dx = \frac{J_0 + 2S_b n_m^0 V_m}{Q_0}, \quad (9)$$

where J_0 is the flow of gas admitted into the tokamak or of the unburnt fuel in the reactor.

The unidimensionality of Eqs. (5)-(7) means that in the divertor the profiles of the plasma density and temperature in the planes $y = \text{const}$ should be similar to the profiles in the plane $y = 0$ formed by transport processes in the main part of the divertor layer, outside the divertor chamber. In this paper we assume that here the plasma does not significantly interact with the limiters and the first wall and there are no volume sources and drains of heat and charged particles, perhaps with the exception of strongly localized regions of gas influx. In this case the state of the plasma is described by the heat and continuity equations in the form

$$\begin{aligned} \frac{\partial}{\partial x} \left(-\kappa_{\perp} \frac{\partial T}{\partial x} \right) + \frac{\partial}{\partial z} \left(-\kappa_{\parallel} \frac{\partial T}{\partial z} \right) &= 0; \\ \frac{\partial}{\partial x} \left(-D_{\perp} \frac{\partial n}{\partial x} \right) + \frac{\partial n V_{\parallel}}{\partial z} &= 0, \end{aligned} \quad (10)$$

where z is the coordinate along the magnetic field ($z = 0$ corresponds to the symmetry plane and $z = z_0$ corresponds to the divertor "neck" OA). In Eq. (10) we have assumed that the heat transfer along the magnetic field in the main part of the divertor layer occurs mainly as a consequence of heat conduction and that the velocity of plasma flow is small in comparison with the sound velocity. The validity of these assumptions at the reactor parameters was theoretically substantiated in many papers [12, 13, 14]. In present-day machines such regimes are also realized [1, 5, 15]. When $V_{||} \ll V_s$ the equation of plasma motion reduces to the condition that the pressure be constant along the magnetic field,

$$\partial n T / \partial z = 0. \quad (11)$$

In the first approximation the solution of Eqs. (10) and (11) will be sought in the form $n = n_s(z)\theta(x)$; $T = T_s(z)\eta(x)$, where n_s and T_s are the plasma parameters in the separatrix ($x = 0$) and the functions $\theta(x)$ and $\eta(x)$ have the form of "steps": $\theta(x \leq \delta_n) = 1$, $\theta(x > \delta_n) = 0$, $\eta(x \leq \delta_T) = 1$, and $\eta(x > \delta_T) = 0$. The parameters δ_n, δ_T are assigned the meaning of the characteristic dimensions of the changes in the plasma density and temperature across the divertor layer. The boundary condition for the functions $n_s(z)$ and $T_s(z)$ follows from the symmetry conditions for $z = 0$ and the continuity of the plasma parameters for $z = z_0$.

$$\frac{dT_s}{dz}(0) = 0; \quad T_s(z_0) = T_d; \quad n_s(z_0) = n_d,$$

where T_d and n_d are the temperature and density of the plasma in the divertor.

Assuming that the estimates $\partial n / \partial x(0) \approx n_s / \delta_n$ and $\partial T / \partial x(0) \approx T_s / \delta_T$ are valid for the gradients of the parameters of the plasma at the separatrix, we integrate Eqs. (10) and (11) with allowance for Eq. (9). As a result we obtain expressions for T_s , n_s , and δ_n, δ_T :

$$T_s(z) = \left[T_d^{7/2} + \frac{7}{2A\delta_T} \int_z^{z_0} dz' \int_0^{z'} q_{\perp}^s(z'') dz'' \right]^{2/7};$$

$$n_s(z) = \frac{n_d T_d}{T_s(z)}; \quad (12)$$

$$\delta_n = \frac{S_0}{J_0 + 2S_b n_m^0 V_m} \int_0^{z_0} n_s D_{\perp}^s \frac{dz}{z_0};$$

$$\delta_T = \frac{S_0}{Q_0} \int_0^{z_0} T_s \kappa_{\perp}^s \frac{dz}{z_0}, \quad (13)$$

where S_0 is the area of the separatrix magnetic surface, q_{\perp}^s is the specific thermal flux, D_{\perp}^s and κ_{\perp}^s are the coefficients of diffusion and thermal conductivity of plasma across the magnetic field in the separatrix $\kappa_{\perp}^s \equiv \alpha_0 D_{\perp}^s$, $A = 1/\sqrt{m_e} e^4 \Lambda$, Λ is the Coulomb logarithm.

The parameters n_d and T_d should be determined from the solution of Eqs. (5)-(7) in the divertor volume. In this paper we consider the case when the length of the force lines of the magnetic field from the entry into the divertor to the neutralization plates is not very large and the plasma parameters vary little along the field in the divertor. The legitimacy of such assumptions was also confirmed by analytic consideration [12] as well as by numerical calculations [13, 14]. In this case the right-hand and left-hand parts of Eqs. (6) and (7) can be integrated over the volume of the divertor (see Fig. 1); when conditions (8) and (9) are used this gives algebraic equations which relate n_d and T_d to other parameters and unknowns. In view of the cumbersome nature of the expressions, we give only the relation which is obtained by the integration of Eq. (6):

$$J_0 + 2(S_b + S_l) n_m^0 V_m + 2\pi R m_0 \left\{ \sin \psi n_d V_d \Delta - \int_0^{\text{ctg } \alpha \delta} \left[2A_m^+(\delta) + \sum_e A_e^+(\delta, e) \right] dy \right\} = 0,$$

where

$$V_d = \sqrt{2T_d/m_i}, \quad \Delta = \min(\delta_n, \delta_T).$$

Henceforth, in comparing the results of calculation with data from experiments on the ASDEX tokamak we use the parameter $\langle n \rangle$, the mean plasma density in the tokamak. The relation between J_0 and $\langle n \rangle$ is derived in the Appendix (Sec. 3).

Discussion of Results. The model presented was used as the basis to calculate the parameters of divertor plasma in the ASDEX tokamak. The constants of the elementary processes used in the calculations are given in the Appendix (Sec. 4). The following geometric characteristics were adopted [5]: $m_0 = 4$, $R = 1.5$ m, $\psi = 12^\circ$, $S_L = 10$ m², $S_D = 1$ m², $S_W = 50$ m², $S_0 = 26$ m², $z_0 = 9$ m. The estimates show that bulk recombination of atoms in the evacuation chamber is characteristic of ASDEX. Under experimental conditions the degree of recycling of molecules was regulated by a change in the rate of titanium sputtering. The maximum surface pumping rate was 10^6 liters/sec [5], which is in satisfactory agreement with the estimates for ρ on the basis of the mechanism of physical reflection ($\rho_w \geq 0.97$).

Calculations were carried out for $\rho_w = 1$ and $\rho_w = 0.97$. We assumed a uniform distribution of the thermal flux in the separatrix and neglected secondary effects on the plates and impurity radiation in the divertor [2]: $q_1^s(z) \equiv \text{const} = Q_0/S_0$, $\alpha_{e,i} = 1$, $Q_{im} = 0$. The coefficient of plasma diffusion in the main part of the divertor layer is of the Bohm type for a magnetic field of 2.7 T that is characteristic of ASDEX: $D_1 = 2.3 \cdot 10^{-2}$ T (eV) m²/sec, $\alpha_0 = 5$. For the peripheral region of the discharge inside the separatrix, where neutrals are ionized, we took a diffusion coefficient which does not depend on the plasma parameters and is equal to 0.4 m²/sec [5].

Figure 2 gives the plasma parameters in the divertor as a function of the average plasma density in the tokamak for a thermal flux of 2.5 MW through the separatrix, which corresponds to a discharge in ASDEX with neutral injection [15]. The dependence of the distribution of the thermal flux entering the divertor by different channels (into the evacuation chamber and only the neutralization plates) is given in Fig. 3. According to the experimental results of [5, 15] when the values of $\langle n \rangle$ are high enough a gas-target regime is realized in the divertor: The thermal flux is dissipated mainly in the evacuation chamber. Qualitatively, this result can be explained as follows. The range of charge-exchange neutrals ($l = V_1/n\sqrt{k_3(k_3 + k_4)}$) in the ASDEX regime under consideration becomes equal to the width of the divertor when $T_d \approx 7$ eV. With a further decrease in T_d as $\langle n \rangle$ increases l grows sharply since $k_3 \sim \sqrt{T} \exp[-13.6/T \text{ (eV)}]$, and the plasma becomes transparent to atoms. This leads to an abrupt drop in the efficiency of convective heat transfer onto the neutralization plates, owing to the ionization of the recycled neutrals. The main cause of the energy efflux is dissipation, in the molecular gas, of the energy of Franck-Condon atoms formed during the dissociation of molecules for which the plasma is not yet transparent. Energy transfer by neutrals upon interaction with the plates is inefficient since at such a low energy the reflection coefficients are close to unity. With a further increase in $\langle n \rangle$ the value of T_d is lowered to the dissociation energy of the molecules and the rate at which Franck-Condon atoms is created drops abruptly. A further decrease in T_d thus requires a large increase in the flow of incoming gas, which ensures transport of the thermal flux. This, as a rule, leads to the development of the tearing instability [15].

The results of the theory and the experimental data differ substantially for low values of $\langle n \rangle$. This can apparently be attributed to the fact that with a decrease in $\langle n \rangle$ there is a decrease in the fraction of energy of the injected beam of neutrals that is conveyed to the plasma, which was not taken into account in our model. The theoretical dependence of the average plasma temperature at the separatrix and the characteristic transverse size of its change on Q_0 , which was found theoretically, is in agreement with experiment.

In calculations for the divertor of the reactor-tokamak parameters corresponding to the INTOR machine were adopted [3]: $m_0 = 2$, $R = 5.5$ m², $S_0 = 300$ m², $S_L = 20$ m², $z_0 = 40$ m. The diffusion in the divertor layer is of the Bohm type $D_1 = 0.0125$ T (eV) m²/sec, $\rho = 1$. The plasma parameters in the divertor as a function of the flux J_0 are given in Fig. 5 for different values of the evacuation rate \bar{V} ($Q_0 = 100$ MW) of the pumps. Figures 6 and 7 demonstrate the J_0 -dependence of the distribution, over the different channels in the evacuation chamber and on the plates of the thermal flux entering the divertor and the average plasma temperature on the separatrix. In accordance with the results of [6] under certain conditions there exists a region of variation of J_0 in which the plasma parameters are not determined uniquely. This indicates the instability of the divertor operation: An increase in J_0 leads to an abrupt transition of the divertor plasma to a state with a low temperature and high density.

It follows from the calculations that with the reactor parameters as well a gas-target regime is possible in a tokamak divertor. The transition to this regime, however, occurs at a substantially lower plasma temperature in the divertor than for ASDEX. The explanation for this is that the integrated plasma density $\int_0^{\delta} n dx$ in the divertor for the reactor is almost

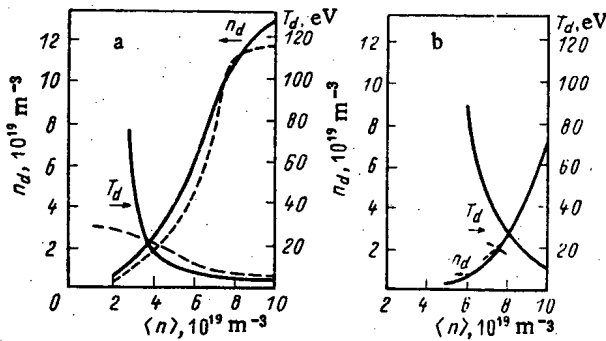


Fig. 2

Fig. 2. Plasma density and temperature in the divertor as a function of the average plasma density during discharge in ASDEX: a) evacuation by pumps; b) gettering of surface of evacuation chamber; —) theory; ----) experiment [5].

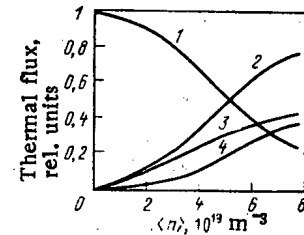


Fig. 3

Fig. 3. Distribution of the thermal flux entering the ASDEX divertor by different channels: 1) convective thermal flux on plate; 2) total energy flux in the evacuation chamber; 3) heat transfer by neutrals into the evacuation chamber; 4) radiation.

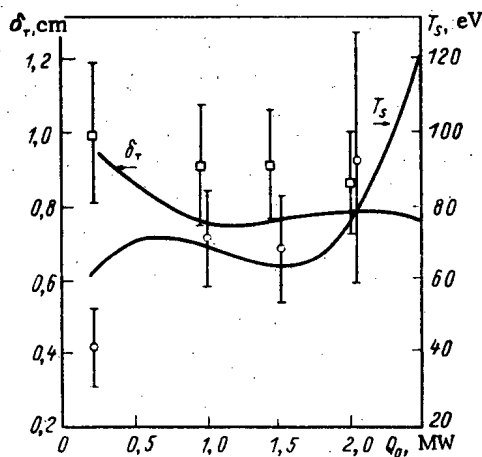


Fig. 4

Fig. 4. Average plasma temperature at the separatrix and width of the temperature profile as a function of the thermal flux and the divertor of the ASDEX tokamak [experiment [5]: \square) δ_r , \circ) T_s].

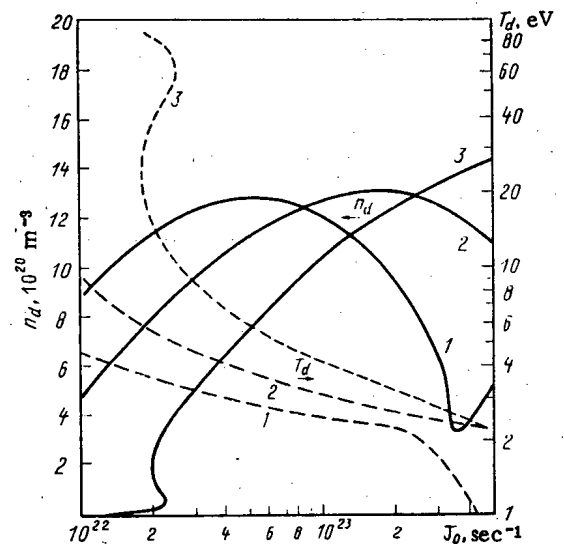


Fig. 5

Fig. 5. Plasma density and temperature in the reactor divertor as a function of J_0 for $\bar{V} = 10^5$ (1), $3 \cdot 10^5$ (2), and 10^6 liters/sec (3).

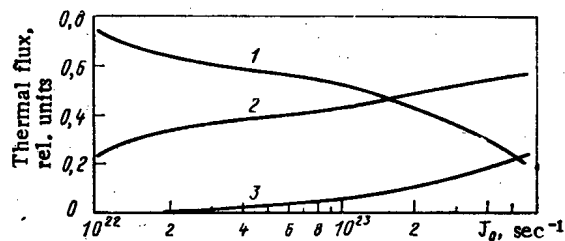


Fig. 6. Distribution of the thermal flux in the reactor divertor: 1) convective heat flow to plate; 2) radiation; 3) heat transfer by neutrals in the evacuation chamber ($\bar{V} = 3 \cdot 10^5$ liters/sec).

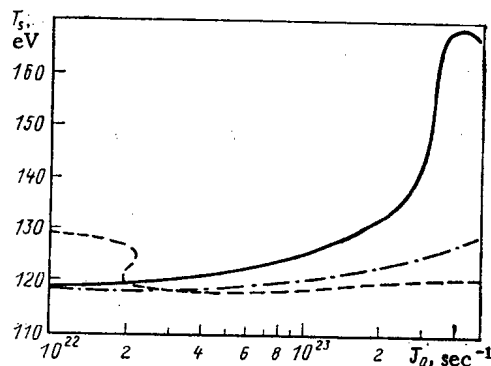


Fig. 7. Average plasma temperature in the reactor at the separatrix as a function of the unburnt fuel and the volume evacuation rate $\tilde{V} = 10^5$ (—), $3 \cdot 10^5$ (---), and 10^6 liters/sec (— · —).

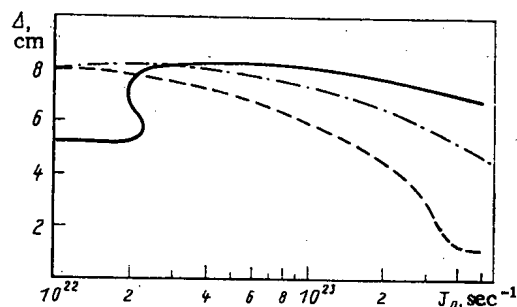


Fig. 8. Width of divertor layer in reactor as a function of J_0 (notation as in Fig. 7).

two orders of magnitude higher than the analogous value for ASDEX and the divertor plasma becomes transparent to atoms when $T_d \leq 1$ eV. We point out that at such a low temperature a significant contribution to the energy balance of the divertor is made by recombination radiation. In the gas-target regime the plasma density in the divertor ($\sim 10^{21} \text{ m}^{-3}$) turns out to be compatible with a medium density at the separatrix ($n_s \leq 6 \cdot 10^{19} \text{ m}^{-3}$) because of the temperature gradient along the magnetic field.

As a result of the calculations carried out we have established that the characteristic width Δ of the divertor layer of plasma is determined mainly by the width δ_T of the temperature profile. This is because the plasma flow velocity (which is small in comparison with the ionic sound velocity) along the magnetic field at the entrance into the divertor is responsible for the characteristic size of the change in the density profile across the field, this change being substantially greater than for $V_{||} \approx V_s$. The last approximation was used earlier in the calculation of the divertor layers [3, 7, 11], which yielded $\delta_n = \sqrt{D_{\perp} z_0 / V_s}$. The dependence of Δ on J_0 is shown in Fig. 8.

Thus, as shown by the calculations carried out in this paper, it is possible in the divertor of a reactor-tokamak to have a gas-target regime in which the thermal flux entering the divertor is dissipated mainly in the evacuation chamber. An increase in the surface of the plasma layer facing the evacuation space apparently should ease the conditions for the realization of such a regime. In this case the inhomogeneity of the plasma parameters in the divertor space along the magnetic field becomes significant and the object of the discussion below is to take this into account.

In conclusion, the author expresses his heartfelt thanks to A. V. Nedospasov for his attention to this paper.

APPENDIX

1. The introduction of the variable $u = \sigma_0 \int_x^\delta n(x') dx'$, where σ_0 is a quantity having the dimension of cross section, and substitution of the adopted form of $\psi_{1,\varphi}$ and $f_{m,\alpha}$ into Eqs. (1) and (2) allows these equations to be reduced to a system of ordinary differential equations in the coefficients $A_{m,\alpha}^\pm$:

$$dA_m^\pm/du = \pm z_m A_m^\pm; \quad (A1)$$

$$dA_a^\pm(e)/du = \pm z_e A_a^\pm(e) \mp \left\{ \sum_{e'} y_{e'} [A_a^+(e') + A_a^-(e')] + V_r n \right\} h(e - e_i) \mp g z_m (A_m^+ + A_m^-) h(e - e_\varphi),$$

where

$$z_m = (k_1 + k_2)/V_m \sigma_0, \quad z_e = (k_3 + k_4)/V_e \sigma_0, \quad y_e = k_4/\nu_e \sigma_0, \quad V_r = k_5/2\sigma_0, \quad h(z \neq 0) = 0, \quad h(0) = 1.$$

2. If the range of the neutrals is large in comparison with the size of the evacuation chamber and if collisions between neutrals can be neglected, molecules and atoms formed during reflection of neutrals from the walls of the evacuated space will enter the plasma. Taking the staged nature of the reflection processes into account, we have

$$A_a^-(\delta, e) = \frac{2\pi R}{S_l + S_w} \int_0^\delta ds \sum_{e'} A_a^+(\delta, e) \left\{ R^w(e', e) + \frac{S_w}{S_l + S_w} \sum_{e''} R^w(e', e'') [\dots] \right\};$$

$$A_m^-(\delta) = \frac{2\pi R \rho_w}{S_l + S_b + S_w (1 - \rho_w) + \tilde{V}/V_m} \int_0^\delta ds \left\{ A_m^+(\delta) + \right.$$

$$\left. + \frac{1}{2} \sum_e A_a^+(\delta, e) \left\{ 1 - \sum_{e'} R^w(e, e') \left(1 - \frac{S_w}{S_l + S_w} \left[1 - \sum_{e''} R^w(e', e'') \dots \right] \right) \right\} \right\}, \quad (A2)$$

where $R^w(e, e')$ is the reflection coefficient for the conditions of the divertor chamber walls.

3. When gas is admitted into the periphery of the discharge only a part of the stream of gas, and not all of it, enters into the separatrix because of ionization in the divertor layer. For a first wall that ideally reflects neutrals we can get

$$f = \exp(-z_m^* u_0) + z_2 [\exp(-z_\varphi^* u_0) - \exp(-z_m^* u_0)] +$$

$$+ z_2 [\tilde{A} \exp(-z_0^* u_0) - \tilde{B} \exp(-z_\varphi^* u_0) + \tilde{C} \exp(-z_m^* u_0)], \quad (A3)$$

where

$$u_0 = \sigma_0 \Delta n_s^*, \quad z_1 = g^* z_m^{*2} / (z_m^{*2} - z_0^{*2}), \quad z_2 =$$

$$= 2z_1 y_\varphi^* z_\varphi^*, \quad z_0^* = \sqrt{z_i^* (z_i^* - y_i^*)}, \quad \tilde{B} = 1/(z_\varphi^{*2} - z_0^{*2}),$$

$$\tilde{C} = 1/(z_m^{*2} - z_0^{*2}), \text{ and } \tilde{A} = \tilde{B}\tilde{C} (z_m^{*2} - z_\varphi^{*2});$$

the asterisk labels plasma parameters at the separatrix after the point of gas entry. To determine the plasma density at the boundary of the totally ionized region inside the separatrix we use the results of [16] in the first approximation. With the notation adopted we have

$$n_0 = \left[\left(\int_0^{z_0} n_s \frac{dz}{z_0} \right)^{2+\beta} + \frac{(2+\beta)(J_0 + 2n_m V_m S_b)}{S_0 A_1 \sigma_0} \left\{ 2 \frac{1-g^*}{z_m^*} \exp(-z_m^* u_0) + \frac{z_1}{z_\varphi^*} \exp(-z_\varphi^* u_0) - \right. \right.$$

$$\left. - \frac{z_1}{z_m^*} \exp(-z_m^* u_0) + z_2 \left(\frac{\tilde{A} \exp(-z_0^* u_0)}{z_0^*} - \frac{\tilde{B} \exp(-z_\varphi^* u_0)}{z_\varphi^*} + \frac{\tilde{C} \exp(-z_m^* u_0)}{z_m^*} \right) \right\} \right]^{1/(2+\beta)} \quad (A4)$$

In the derivation of Eq. (A4) it was assumed that in the region under consideration $D_{\perp} = A_1 n^{\beta}$. We shall find the relation between n_0 and $\langle n \rangle$. In the center of the tokamak discharge the profile of the plasma density is determined by the equality of the particle fluxes owing to anomalous diffusion and pinch effect and has a parabolic form [17]: $n = 3/2 \langle n \rangle (1 - r^2/a^2)$. The radius r_0 of the magnetic surface on which $n \approx n_0$ is determined by the condition $(a - r_0)n_0\sigma \approx 1$, where $\sigma \approx 10^{-18} \text{ m}^2$ is the characteristic cross section for the processes with the participation of neutrals. Bearing in mind that the plasma filament in a tokamak is practically always opaque to neutrals ($n_0\sigma a \gg 1$), we get

$$n_0 \approx \sqrt{3 \langle n \rangle / \sigma a}. \quad (\text{A5})$$

4. The constants of the elementary processes were obtained by approximation of the graphical dependences given in [14]:

$$k_1 = 0.76 \cdot 10^{-14} \frac{\sqrt{T} \exp(-15.4/T)}{1 + 0.005T} \left[\frac{\text{m}^3}{\text{sec}} \right];$$

$$k_2 = 10^{-14} \exp(-4.5/T) \left[\frac{\text{m}^3}{\text{sec}} \right] (T \leq 10 \text{ eV});$$

$$k_3 = 0.73 \cdot 10^{-14} \frac{\sqrt{T} \exp(-13.6/T)}{1 + 0.01T} \left[\frac{\text{m}^3}{\text{sec}} \right];$$

$$k_4 = 0.87 \cdot 10^{-4} (e + e_i)^{1/3} \left[\frac{\text{m}^3}{\text{sec}} \right];$$

$$k_5 = 1.5 \cdot 10^{-18} T^{-1.2} \left[\frac{\text{m}^3}{\text{sec}} \right];$$

$$g = 1 - 0.5 \cdot \exp(-10/T).$$

The combinations with $R(\epsilon, \epsilon')$ appearing in Eqs. (3) and (A2) can be expressed in terms of $R_p(\epsilon) = \sum_{\epsilon'} R(\epsilon, \epsilon')$; $R_E(\epsilon) = \sum_{\epsilon'} R(\epsilon, \epsilon') \epsilon' / \epsilon$. For R_p and R_E the formulas are matched to the data of [8]. In the case of the normal incidence of particles of the surface we have

$$R_p(\epsilon) = 1/[1 + 3.7 (\epsilon/\epsilon_L)^{0.4}],$$

$$R_E(\epsilon) = 1/[1 + 9 (\epsilon/\epsilon_L)^{0.5}],$$

where $\epsilon_L = 30.8(M_1 + M_2) Z_1 Z_2 (Z_1^{2/3} + Z_2^{2/3})^{1/3} / M_2$ (eV), $M_{1,2}$ are the mass numbers, and $Z_{1,2}$ are the atomic numbers of the incident particles and the atoms of the target, respectively.

LITERATURE CITED

1. S. A. Cohen, Nucl. Fusion, 22, No. 8, 1113 (1982).
2. M. Keilhacker, Fiz. Plazmy, 9, No. 1, 90 (1983).
3. INTOR, Phase One (Report of International Tokamak Reactor Workshop), IAEA, Vienna (1982).
4. Y. Shimomura and H. Maeda, J. Nucl. Mater., 76-77, 45 (1978).
5. M. Keilhacker et al., Report on Ninth International Conference on Plasma Physics and Controlled Nuclear Fusion, IAEA, Baltimore (1982), IAEA-CN-41/R-2.
6. A. V. Nedospasov and M. Z. Tokar', Dokl. Akad. Nauk SSSR, 270, No. 6, 1376 (1983).
7. J. Ogden et al., Plasma Sci., PS-9, No. 4, 274 (1981).
8. W. Eckstein and H. Verbeke, Rep. IPP No. 9/32, Garching (1979).
9. S. Rehker and H. Wobig, Plasma Phys., 15, No. 10, 1083 (1973).
10. R. Chodura, Phys. Fluids, 25, No. 9, 1628 (1982).
11. T. F. Volkov and V. D. Kirillov, Preprint No. 3358/8, Institute of Atomic Energy, Moscow (1980).
12. A. V. Nedospasov and M. Z. Tokar', in: Proceedings Tenth European Conference on Controlled Fusion and Plasma Physics, Moscow (1981), Vol. 1, p. G-10.
13. Contribution of the USSR to the INTOR Project (Phase 2A) [in Russian], Institute of Atomic Energy, Moscow (1982).
14. D. Post et al., Report PPPL No. 1913, Princeton, N. J. (1982).
15. Y. Shimomura et al., Report IPP No. III/80, Garching (1982).
16. N. N. Vasil'ev et al., Fiz. Plazmy, 8, No. 1, 37 (1982).
17. J. Strachan et al., Nucl. Fusion, 22, No. 9, 1145 (1982).

LETTERS TO THE EDITOR

 γ RADIATION FIELD GENERATED BY NEUTRONS IN AN UNBOUNDED
UNIFORM AIR MEDIUM

A. V. Zhemerev

UDC 539.122.04

It is well known that the propagation of γ radiation in air is accompanied by various physical effects, for example, glowing of the air [1-3], Compton electron currents [4], oscillating electromagnetic fields [5], and others. The spatial-temporal characteristics of the γ -radiation field are of interest in the investigation of these effects. For pulsed monoenergetic sources of γ radiation these characteristics have been investigated in detail with the help of the Monte Carlo method and interpolated analytically by the dependences in [6]. The absorbed γ -radiation energy and the Compton electron current caused by the γ radiation, which is initiated by neutrons in an unbounded uniform air medium from a point pulsed isotropic monoenergetic source of neutrons with an energy of approximately 10 MeV, are calculated in this paper by the Monte Carlo method.

The absorbed γ -radiation energy and the Compton electron current are related to the neutron distribution function $N(\mathbf{r}, \epsilon, t)$ by the following relationships:

$$I_a(\mathbf{r}, t) = \int d\epsilon \sum_i \int d\mathbf{r}' N(\mathbf{r}', \epsilon, t') \Sigma_i(\epsilon) I_a[E_i(\epsilon), |\mathbf{r} - \mathbf{r}'|, t - t']; \quad (1)$$

$$I_e(\mathbf{r}, t) = \int d\epsilon \sum_i \int d\mathbf{r}' N(\mathbf{r}', \epsilon, t') \Sigma_i(\epsilon) I_e[E_i(\epsilon), |\mathbf{r} - \mathbf{r}'|, t - t'] \cos \Psi, \quad (2)$$

where $t = t' + |\mathbf{r} - \mathbf{r}'|/c$; $\cos \Psi = \mathbf{r}^2 - (\mathbf{r}, \mathbf{r}')/|\mathbf{r}| |\mathbf{r}' - \mathbf{r}|$; v and ϵ are the velocity and energy of the neutrons, $\Sigma_i(\epsilon)$ is the macroscopic cross section of the i -th reaction of a neutron with nuclei of the air atoms leading to the production of a γ quantum with energy $E_i(\epsilon)$, $I_a(E, \mathbf{r}, t)$ and $I_e(E, \mathbf{r}, t)$ are the absorbed energy and the Compton electron current from a point prompt isotropic source of γ quanta with energy E , and t' and \mathbf{r}' are the time and place of production of the γ quantum, respectively. The summation over i in the expressions (1) and (2) runs over all possible reactions. It has been assumed in writing the expressions (1) and (2) that the indicatrix of emergence of a γ -quantum is spherically symmetric.

The values of $\Sigma_i(\epsilon)$ for a neutron energy < 1 MeV depend on the neutron energy according to a $1/v$ law [7], and it has proven possible to calculate analytically the expressions (1) and (2) [8]. At a higher energy (> 4 MeV) various reactions accompanied by γ radiation are possible whose cross sections depend in a complicated way on the neutron energy (the dependence of the mean energy E_γ and the probability of emergence P of a γ quantum upon the collision of a neutron with nuclei of air atoms is shown in Fig. 1 as a function of the neutron energy ϵ); therefore, the expressions (1) and (2) can be calculated only by the Monte Carlo method.

One can describe the quantities $I_a(E, \mathbf{r}, t)$ and $I_e(E, \mathbf{r}, t)$ by the following function:

$$I(E, \mathbf{r}, t) = \frac{A \exp[-r/\lambda(E)]}{4\pi r^2} \{g_1(t - r/c) + f(r) g_2(r, t - r/c)\}, \quad (3)$$

where $\lambda(E)$ is the mean free path of a γ -quantum with energy E until Compton scattering, $g_1(t) = \delta(t)$ is the temporal dependence of the contribution from unscattered γ radiation,

$g_2(r, t)$ is the same thing for scattered radiation with $\int_0^\infty g_2(r, t) dt = 1$, and $f(r)$ is the

contribution from the scattered γ radiation of a steady source. The characteristic time of variation of the function $g_2(r, t)$ is approximately 0.3-0.5 μsec [6]; therefore if one digresses from clarifications of the details of the front of the quantities (1) and (2) with a time less than 1 μsec (the minimal scale of subdivision of the time interval in a calculation

Translated from *Atomnaya Energiya*, Vol. 56, No. 3, pp. 173-175, March, 1984. Original article submitted November 26, 1982.

Declassified and Approved For Release 2013/09/14 : CIA-RDP10-02196R000300040003-5
 by the Monte Carlo method), one can neglect the temporal expansion of the scattered γ radiation and assume that $g_2(r, t) = \delta(t)$. In addition the characteristic time of variation of the distribution function of neutrons which have undergone several collisions is determined by the ratio l/v , where l and v are the mean free path and velocity of the retarded neutron, which amounts to around several μsec , which also justifies the approximation used.

In what follows we shall adopt the following approximate relationships for the functions $I_a(E, r, t)$ and $I_e(E, r, t)$:

$$I_a(E, r, t) = \frac{E \exp(-r/\lambda_{\text{eff}}) \delta(t - r/c)}{4\pi\lambda_{\text{eff}}^2} \quad (4)$$

$$I_e(E, r, t) = \frac{\mu(E) l(E) \exp(-r/\lambda_{\text{eff}}) \delta(t - r/c)}{4\pi\lambda_{\text{eff}}^2} \quad (5)$$

where $\mu(E)$ is the mean cosine of emergence of a Compton electron knocked out by a γ quantum with energy E . $l(E)$ is the shift of a Compton electron with energy E [4]. $\lambda_{\text{eff}} = \lambda(E) E/E_e$ is the effective mean free-path of the γ quantum, and E_e is the mean energy of the knocked-out Compton electron.

The neutron distribution function $N(r, \epsilon, t)$ and the functionals (1) and (2) associated with it were calculated by the Monte Carlo method with account taken of the expressions (4) and (5) for monoenergetic sources of neutrons with the initial energy 6.8, 10, 12, and 14 MeV. The system of neutron constants is taken from [7]. The computation program is written in the FORTRAN language for a BESM-6 computer. Simulation of the history of a neutron was terminated when it reached an energy of 4 MeV. A total of 40,000 histories were considered in each alternative. The probable error did not exceed 5-10% in 3-4 mean free paths μ^{-1} ($\mu^{-1} = 300 \text{ m}$ is the effective mean free path of a γ -quantum with energy 1 MeV for air of normal density) and increased to 15-20% at large distances.

The results of numerical calculations by the Monte Carlo method were represented in the following form:

$$I_a(x, \tau) = \frac{E_\gamma(x) \mu}{4\pi r^2} f_a(x) g_a(x, \tau); \quad (6)$$

$$I_e(x, \tau) = \frac{l_e(x) \mu}{4\pi r^2} f_e(x) g_e(x, \tau), \quad (7)$$

where $x = \mu r$ and $\tau = \mu c(t - r/c)$. The function $f(x)$ describes the characteristics of the γ -radiation field from a steady source, and $g(x, \tau)$ describes the smearing of the pulse in time. The functions $f(x)$ and $g(x, \tau)$ satisfy the normalization conditions

$$\int_0^\infty f(x) dx = 1; \quad (8)$$

$$\int_0^\infty g(x, \tau) d\tau = 1. \quad (9)$$

The calculations have shown that the function $g(x, \tau)$ can be represented with a high degree of accuracy in the form

$$g(x, \tau) = \frac{1}{\langle \tau(x) \rangle} \exp \left[-\frac{\tau}{\langle \tau(x) \rangle} \right], \quad (10)$$

where $\langle \tau(x) \rangle$ is determined by the expression

$$\langle \tau(x) \rangle = \int_0^\infty d\tau \tau g(x, \tau) / \int_0^\infty d\tau g(x, \tau) \quad (11)$$

and is calculated by the Monte Carlo method. The accuracy of the expression (10) is illustrated by Fig. 2, in which the dependence $I_a(\tau) = \int_0^\infty I_a(x, \tau) 4\pi r^2 dr / E_\gamma$ and the function (10)

corresponding to it calculated by the Monte Carlo method are presented for a source of neutrons with an initial energy of 14 MeV ($\langle \tau \rangle = 8.66$).

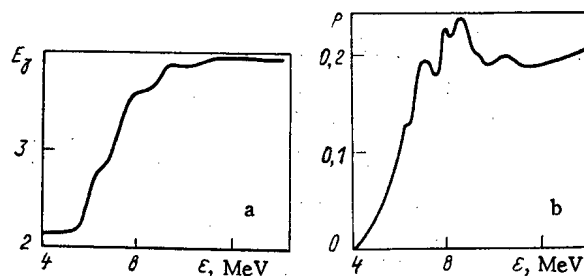


Fig. 1. Dependence on the neutron energy ϵ of (a) the mean energy E_γ and (b) the probability of emergence P of a γ -quantum knocked out upon the collision of a neutron with nuclei of air atoms.

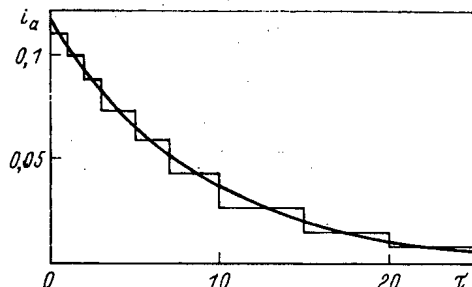


Fig. 2. Dependence of the absorbed energy i_a on time: the histogram denotes the calculation by the Monte Carlo method, and the solid curve denotes the calculation according to formula (10).

TABLE 1. Functions $f_a(x)$ and $f_e(x)$

ϵ , MeV	Interpolation coefficients	Functions	x									
			1	2	3	4	5	6	8	10		
14	$E_\gamma = 3.04$ MeV	f_a	0,242	0,194	0,119	0,0675	0,0369	0,0199	0,00591	0,00180		
	$l_e = 4.99$ m	f_e	0,257	0,233	0,156	0,0939	0,0540	0,0303	0,00939	0,00293		
12	$E_\gamma = 2.67$ MeV	f_a	0,241	0,193	0,119	0,0681	0,0369	0,0201	0,00597	0,00184		
	$l_e = 4.39$ m	f_e	0,258	0,232	0,156	0,0936	0,0540	0,0303	0,00942	0,00298		
10	$E_\gamma = 2.43$ MeV	f_a	0,238	0,193	0,120	0,0684	0,0375	0,0204	0,00600	0,00182		
	$l_e = 3.98$ m	f_e	0,258	0,233	0,156	0,0942	0,0543	0,0306	0,00957	0,00296		
8	$E_\gamma = 1.92$ MeV	f_a	0,267	0,192	0,113	0,0615	0,0327	0,0175	0,00498	0,00148		
	$l_e = 3.23$ m	f_e	0,287	0,232	0,146	0,0837	0,0465	0,0257	0,00771	0,00234		
6	$E_\gamma = 0.55$ MeV	f_a	0,284	0,190	0,103	0,0507	0,0241	0,0113	0,00259	0,000648		
	$l_e = 0.779$ m	f_e	0,321	0,234	0,134	0,0702	0,0351	0,0174	0,00432	0,00111		

TABLE 2. Functions $\langle \tau_a(x) \rangle$ and $\langle \tau_e(x) \rangle$

ϵ , MeV	Mean time	x									
		1	2	3	4	5	6	8	10		
14	$\langle \tau_a \rangle$	4,62	7,74	9,99	11,6	12,4	12,8	12,6	12,1		
	$\langle \tau_e \rangle$	2,87	5,48	7,59	9,31	10,5	11,0	11,5	11,1		
12	$\langle \tau_a \rangle$	4,48	8,05	10,4	12,2	12,9	13,4	13,3	13,1		
	$\langle \tau_e \rangle$	2,97	5,72	7,98	9,66	10,9	11,6	12,1	12,1		
10	$\langle \tau_a \rangle$	4,92	8,30	10,8	12,7	13,7	14,2	14,0	13,0		
	$\langle \tau_e \rangle$	3,05	5,78	8,19	9,98	11,2	12,2	12,7	12,3		
8	$\langle \tau_a \rangle$	4,82	7,93	10,1	11,6	12,3	12,7	11,7	10,5		
	$\langle \tau_e \rangle$	3,11	5,68	7,70	9,07	9,98	10,5	10,7	10,1		
6	$\langle \tau_a \rangle$	5,33	9,23	12,5	14,8	16,1	16,6	15,7	14,7		
	$\langle \tau_e \rangle$	3,36	6,33	8,99	11,1	12,4	13,1	13,3	11,9		

The calculated values of $f_a(x)$, $f_e(x)$, $\langle \tau_a(x) \rangle$, and $\langle \tau_e(x) \rangle$ are presented in Tables 1 and 2 for various x ; $f_a(x)$ and $f_e(x)$ are interpolated in the Bergerov form:

TABLE 3. Interpolation Coefficients for the Absorbed Energy and the Compton Electron Current [formula (12)]

ϵ , MeV	A_a	B_a	C_a	D_a	A_e	B_e	C_e	D_e
14	0,915	0,396	2,622	0,780	0,172	0,396	0,492	0,780
12	0,915	0,396	2,622	0,780	0,172	0,396	0,492	0,780
10	0,953	0,396	2,730	0,780	0,191	0,360	0,516	0,756
8	0,527	0,108	0,660	0,732	0,199	0,432	0,492	0,852
6	0,595	0,144	0,732	0,876	0,258	0,504	0,588	0,948

TABLE 4. Interpolation Coefficients for the Mean Time of the Absorbed Energy and the Compton Electron Current [formula (14)]

ϵ , MeV	a_{1a}	a_{2a}	a_{3a}	a_{4a}	a_{5a}	a_{1e}	a_{2e}	a_{3e}	a_{4e}	a_{5e}
14	0,269	21	0,9	0,30	0,02	0,370	6	0,9	0,05	0,03
12	0,437	12	0,9	0,25	0,03	0,403	6	0,9	0,05	0,03
10	0,433	12	0,9	0,20	0,03	0,440	6	0,9	0,05	0,03
8	0,350	18	0,9	0,35	0,03	0,337	9	0,9	0,15	0,03
6	0,490	12	0,9	0,20	0,03	0,198	18	0,9	0,125	0,015

$$f(x) = A \exp(-Cx) + Bx \exp(-Dx). \quad (12)$$

The interpolation coefficients are selected from the condition of minimization of the function

$$\sigma = \frac{1}{8} \sum_{i=1}^8 [1 - f(x_i)/f_i]^2 \quad (13)$$

and normalization of the expression (8); $\langle \tau_a(x) \rangle$ and $\langle \tau_e(x) \rangle$ are interpolated in the form of a fractional-rational function

$$\langle \tau(x) \rangle = a_1 \frac{1 + a_2 x + a_3 x^2}{1 + a_4 x + a_5 x^2} \quad (14)$$

with the minimization condition (13). The calculated interpolation coefficients are presented in Tables 3 and 4. The accuracy of interpolation of the computational results of the functions (6) and (7) is no worse than the probable error of the calculations by the Monte Carlo method.

We shall compare the results obtained with the results of calculations of the characteristics of the γ -radiation field initiated by a source of neutrons with energy <4 MeV [8]. The mean energy of the γ radiation formed upon the capture of neutrons with energy <4 MeV is equal to 0.43 MeV [9], but the characteristic time during which the emission of a γ quantum occurs is approximately equal to the lifetime of neutrons in air (0.06 sec). Thus the power of the emitted γ radiation is 0.43 MeV/0.06 sec ≈ 7 MeV/sec, which is less by far than the power of the γ radiation resulting from the deceleration of a neutron with energy ~ 10 MeV for example, for a source of neutrons with energy 14 MeV the power of the γ radiation initiated is equal to $(3.04/8.66) \cdot 10^6 \approx 3.5 \cdot 10^5$ MeV/sec].

LITERATURE CITED

1. A. V. Zhemerev and Yu. A. Medvedev, At. Energ., 29, No. 4, 287 (1970).
2. A. V. Zhemerev et al., At. Energ., 35, No. 6, 438 (1973).
3. A. V. Zhemerev, Yu. A. Medvedev, and B. M. Stepanov, At. Energ., 42, No. 3, 230 (1977).
4. A. V. Zhemerev, Yu. A. Medvedev, and B. M. Stepanov, At. Energ., 41, No. 4, 268 (1976).

5. Yu. A. Medvedev, B. M. Stepanov, and G. V. Fedorovich, The Physics of Radiative Excitation of Electromagnetic Fields [in Russian], Atomizdat, Moscow (1980).
6. S. N. Sidneva and A. S. Strelkov, At. Energ., 39, No. 3, 217 (1975).
7. V. M. Kuvshinnikov et al., in: Problems of the Metrology of Ionizing Radiations [in Russian], Atomizdat, Moscow (1975), p. 22.
8. A. V. Zhemerev et al., At. Energ., 38, No. 3, 174 (1975).
9. A. V. Zhemerev, Yu. A. Medvedev, and B. M. Stepanov, At. Energ., 42, No. 5, 407 (1977).

DETERMINING THE DENSITY OF PYROCARBON COATINGS ON MICROPINS BY GASIFICATION IN A GLOW DISCHARGE

A. A. Babad-Zakhryapin and I. S. Alekseeva

UDC 533.924:620.18:661.666

A micropin usually receives several layers of pyrocarbon (PC) differing in density, and each layer is usually stratified. Therefore, one can usually speak only of a certain average density of the coating, which is governed by the density of each component and by the porosity.

The chemical activities of the components are dependent mainly on the lattice disorder. Therefore, gasification (oxidation) can be used to determine the density. Oxygen is activated in the positive column of a glow discharge, and this greatly accelerates the gasification which enables one to measure the densities of pyrocarbon coatings (without intermediate SiC layers) on micropins. The gasification of pyrocarbon in unactivated oxygen at 30-50°C and low pressures has a negligibly small rate, so the presence of deeper pores does not influence the gasification in the glow discharge, where only the porosity of the surface layer is important.

Therefore, one can measure the gasification rate in a glow discharge to determine the densities of PC coating components, as well as the densities of the corresponding layers. This is often made of differences in chemical activity in the components of PC coatings in relation to oxygen to determine the amount of the most disordered component by measuring the change in pH in a water suspension containing a ground specimen of the PC coating [1].

The structural components in a layer of the coating may firstly influence the gasification of the PC coatings, which can be used in identifying them, and secondly it enables one to determine the average density. For this purpose it is sufficient to use a standard method [2] to measure the gasification rate for the PC coating layer without removal from the micropin. In particular, kinetic curves for the mass loss can be used. A single micropin is used in the first case. There is a change in the slope of the kinetic curve on going from one component to another differing in activity. On the whole, the curve takes the form of a kinked line, with each part corresponding to one component.

In the second case, one uses a batch of pins (200-250) with identical layer thicknesses in the PC coating. The mass changes in the various components are averaged, and the slope of the resulting curve will be determined by the averaged activity and the porosity, i.e., one can judge the average density of the corresponding PC layer. If standards with the same structure and a known density are used, one can employ the slope of the gasification curve to determine the absolute density.

This method has been used to determine the density of a one-layer PC coating on model micropins with cores of zirconium carbide of diameter 0.5 mm. Table 1 gives the thickness, density as determined from the poured mass, optical and isotropy coefficient, and deposition conditions. The gasification for a batch of micropins was performed in the positive column of a glow discharge at an air pressure of 150 Pa. The running voltage was 7000 V, while the discharge current was 2 mA. The micropin temperature during gasification did not exceed 50°C. The pins were periodically removed from the discharge chamber for diameter and mass measurement.

Translated from *Atomnaya Energiya*, Vol. 56, No. 3, pp. 175-176, March, 1984. Original article submitted April 15, 1983.

Figure 1 shows kinetic curves for the mass loss, together with the analogous curve 4 for isotropic pyrocarbon of density 2.1 g/cm^3 . The more rapid gasification of the PC coatings indicates that their density was less than 2.1 g/cm^3 . The gasification curves for batches 2 and 3 each consist of two rectilinear parts with different slopes. This indicates a lower density in the peripheral parts of the PC coating, with a density step between one layer and the other. Microstructural examination confirmed that there were zones differing in density (Fig. 2).

The coating in batch 1 was of identical density throughout the thickness. Curves 2 and 3 of Fig. 1 provide information on the relative amounts of the different layers in the PC coatings if the gasification is complete. In that case, the ordinate intercepts corresponding to the straight-line parts define the relative contents of the components. For example, for batch 3 the ratio between the low-density and higher-density components was 1:1.

The equal-density coating on batch 1 was used to find the absolute densities of these PC coatings. The density of this standard was determined from $\rho = P/V$, where P is the mass of the PC coating removed during complete gasification, and V is the volume of the PC coating calculated from the size change: $V = 4/3\pi(r_1^3 - r_2^3)$.

The error in the resulting density is defined by

$$\Delta\rho/\rho = \Delta P/P - 2\Delta r/r,$$

where ΔP is the weighing error, r is radius, and Δr is the error in measuring the radius. With $\Delta P = 0.001 \text{ mg}$ and $\Delta r = 10 \text{ }\mu\text{m}$, the overall error is $\pm 5\%$, i.e., the coating density was $2.0 \pm 0.1 \text{ g/cm}^3$. On the assumption that the slope of the rectilinear part of the gasification curve is linearly related to the PC density, we found the densities for the various layers in batches 2 and 3 (Table 1). It is evident that the densities of the PC coating in batches 2 and 3, as determined from the poured density, somewhat exceed the mean value calculated from the densities of the individual layers.

TABLE 1. Deposition Conditions and Properties of PC Coatings

Batch	Deposition temp., °C (medium heptane)	Coating thickness, μm	Optical anisotropy coefficient	Density, g/cm^3		
				from poured density	from gasification	
					outer layer	inner layer
1	1250	70	1.09	2.0	2.0	—
2	1320	80	1.06	1.5	1.1	1.7
3	1450	250	1.03	1.0	0.8	1.1

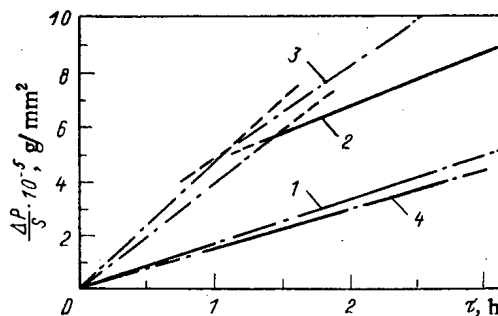


Fig. 1. Micropin mass change as a function of time on gasification in a glow-discharge positive column (the numbers on the curves are the numbers of the batches in Table 1).

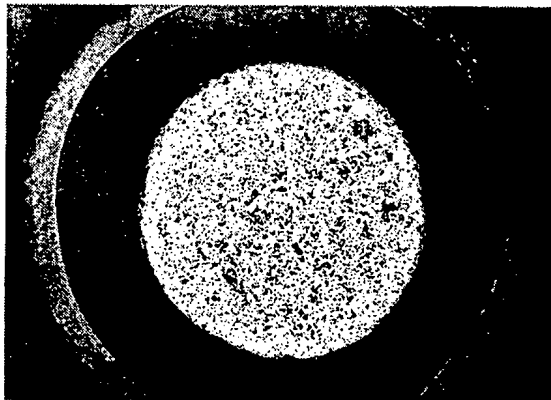


Fig. 2. Photomicrograph of a micropin from batch 3 (Table 1) with PC coating consisting of two zones differing in density ($\times 100$).

The information provided by this method for the density distribution is extremely important and cannot be derived by any other method, since data on the density of each layer can be used to characterize the parts.

LITERATURE CITED

1. E. Wolfrum and H. Nickel, Nucl. Technol., 35, No. 2, 293 (1977).
2. N. S. Alekseeva et al., At. Energ., 52, No. 4, 266 (1982).

GRAPHITE CAPSULES FOR ACCOMMODATING INDICATORS OF THE TEMPERATURE AND THE NEUTRON FLUX IN IRRADIATION UNITS

T. N. Shurshakova, V. V. Gundorov,
and K. V. Grigor'eva

UDC 536.51+621.039+539.2:539.12.04

When samples are irradiated in various irradiation units of reactors, the temperature and the neutron flux must be known. In certain cases the design of irradiation units does not allow external communication or experimental conditions require utilization of sealed tubes so that measurements of temperature with thermocouples are not possible. For these goals temperature determinations with the aid of diamond indicators are most widely employed.

The operation of the indicators is based on the expansion of the crystal lattice of diamond upon neutron irradiation. During isochronous thermal annealing of the irradiated diamond at a temperature below the temperature at irradiation, the crystal lattice parameter does not change. Its restoration begins once the temperature of the irradiation has been exceeded. The inflection point on the linear dependence of the lattice parameter upon the temperature of annealing corresponds to the temperature of irradiation.

Powder of natural diamond with a grain size of 20-14 μm (type AM-20) is used as the indicator. The range of the temperatures which can be measured is 100-1000°C, and the accuracy of the measurements is ± 10 -15°C. The highest admissible heating rate of the indicator is 100 deg/sec. A diamond indicator is a cylindrical capsule (see Fig. 1a) of stainless steel with a length of 5 mm, a diameter of 1 mm, and a wall thickness of 0.4 mm (V. I. Karpukhin and V. A. Nikolaenko, "Temperature Measurements with the Aid of Irradiated Diamond" [in Russian], Atomizdat, Moscow, 1971). The capsule is filled so that the height of the diamond powder column is 3.5 mm. The filled capsule is closed with a metal plug and then roll-forged; then the jacket is squeezed at the point of the probe and welded up.

Such a capsule is not without shortcomings. Among these shortcomings are the complicated manufacture and the possible destruction of the tube (usually at the point of welding) because

Translated from Atomnaya Energiya, Vol. 56, No. 3, p. 177, March, 1984. Original article submitted April 18, 1983; resubmitted October 25, 1983.

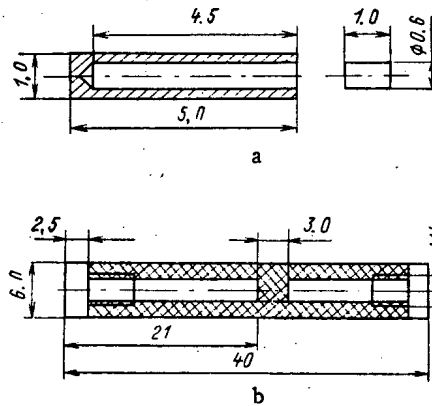


Fig. 1. Design of a capsule for irradiating indicators of a) steel and b) graphite. (Dimensions in mm.)

the steel becomes brittle during prolonged neutron exposure at high temperatures. Furthermore, since the material of the capsule is highly activated after the irradiation, disassembling the capsule requires equipment for shielding the worker from radioactive radiations. The capsules are opened by cutting on a machine tool. This is rather laborious particularly when the cutting is made by remote control in a shielded box.

These shortcomings are overcome when graphite is used for manufacturing the capsules. Since graphite is only activated, the capsules can be disassembled without using remotely controlled instruments and practically without radiation shielding. The dimensions of a graphite capsule correspond to a "standard" sample used in metallurgical irradiation work (diameter 6 mm and length 40 mm). Therefore the capsule can be placed into irradiation units with the gaps used for standard samples. Through the use of fine-grained high-strength graphite (e.g., MPG graphite), the integrity of the capsule can be maintained at high irradiation temperatures and under high neutron fluxes.

The design of a graphite capsule is rather simple (see Fig. 1b) and such a capsule is less laborious to manufacture. The capsule consists of two sections which are separated by a 3-mm-thick connecting portion. The diamond powder for measuring the irradiation temperature is poured into the smaller section. Adequate sealing is obtained by a screwed-in graphite lid. This simplifies the design of the capsule and makes roll forging and welding unnecessary; no machine tool is required for cutting after the irradiation of the capsule. Detectors for measuring the neutron flux can be housed in the second cavity of the capsule with the larger volume. After the irradiation, the samples in the capsule can be easily removed by unscrewing and the temperature and neutron-flux indicators can be taken out.

RADIATION-INDUCED CHANGES IN THE THERMAL CONDUCTIVITY AND THE ELECTRICAL RESISTIVITY OF PYROLYTIC GRAPHITE

Yu. S. Virgil'ev and I. A. Dmitriev

UDC 621.039.532.21

Radiation-induced changes in the physical properties of various brands of Russian construction graphite have been extensively investigated in the last few years. These investigations helped to determine the dependence of the relative change in the thermal conductivity of GMZ graphite upon the neutron flux in the interval of 10^{18} – $2.5 \cdot 10^{22}$ neutrons/cm²* and at an irradiation temperature of 340–1200°K [1]. Since these relative changes are not given by the material but depend upon the neutron flux and the temperature [2], the relative changes apply to various modifications of this graphite which are obtained by varying the number of compacting impregnations by pitch and the temperature of graphitization. This applies also to several other graphites produced with the conventional electrode technology.

We present in this work the results of measurements of the thermal conductivity of another type of carbon material comprised of anisotropic pyrolytic graphite (PG), obtained by precipitation from the gas phase at 2400°K and irradiated at 320–340° and 870–970°K with a flux of up to $4.4 \cdot 10^{21}$ neutrons/cm². The thermal conductivity and the electrical resistivity were measured at $300 \pm 5^\circ\text{K}$ in planes parallel and perpendicular to the direction of precipitation.

The properties of the pyrolytic graphite samples examined before their irradiation are listed below:

density (t/m ³)	2.14–2.17
lattice parameter (nm) in the direction of the c axis	0.6862
size (nm) of the crystallites:	
in the direction of the c axis	13.5
in the direction of the a axis	19.5
thermal conductivity (W/(m·K))	
in parallel direction	89.5
in perpendicular direction	2.2
specific electrical resistivity ($10^{-6} \Omega \cdot \text{m}$)	
in parallel direction	4.7
in perpendicular direction6300

It follows from the above data that the crystal structure of the pyrolytic graphite is quite imperfect and that the properties are highly anisotropic: The anisotropy of the material is 40 with respect to its thermal conductivity and reaches 135 with respect to the electrical resistivity.

The thermal conductivity [1] was measured with the technique of an axial thermal flux on samples with the dimensions $5 \times 5 \times 10$ mm or on cylinders with a diameter of 5–4 mm and a height of 6–10 mm. In this way we could use the samples which are usually employed in radiation testing. The total relative error did not exceed 10% in the measurements of the thermal conductivity and 2% in the temperature measurements. The results of the measurements were used to construct (see Fig. 1) the dependence of the relative thermal resistivity of the pyrographite upon the neutron flux for the irradiation temperature indicated:

$$\Delta K/K = (\lambda_{\text{ini}}/\lambda_{\text{irr}}) - 1,$$

where λ_{ini} and λ_{irr} denote the thermal conductivity before and after the irradiation. We list for comparison the corresponding dependence of GMZ graphite [1]. It follows from Fig. 1 that the relative change in the thermal resistivity of pyrographite in the direction perpendicular to the plane of precipitation (which characterizes the dominant position of the crystals)

*Here and below, the flux is indicated for neutrons with $E \geq 0.18$ MeV.

Translated from *Atomnaya Energiya*, Vol. 56, No. 3, pp. 177–178, March, 1984, Original article submitted April 18, 1983.

TABLE 1. Neutron-Flux Dependence of the Specific Electrical Resistivity of Pyrolytic Graphite in Directions Parallel and Perpendicular to the Plane of Precipitation (irradiation at 870-970°K)

Neutron flux (10^{21} neutrons/cm ²)	$\rho_{\parallel} \cdot 10^{-6} (\Omega \cdot m)$	$\rho_{\perp} \cdot 10^{-6} (\Omega \cdot m)$
0	4,7	6300
0,9	33	3000
2,2	47	3500
3,0	43	3200
3,6	25	4300

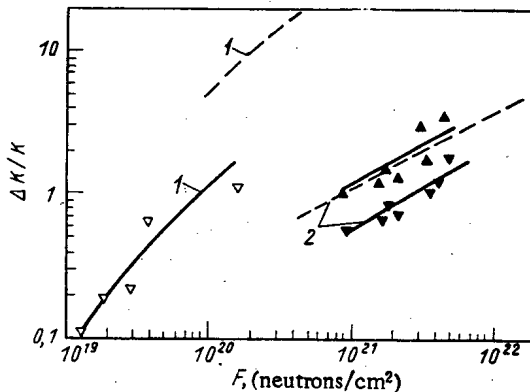


Fig. 1. Neutron-flux dependence of the relative thermal resistance at 300°K of pyrographite samples (obtained at 2400°K) in directions (▲) parallel and (▼, ▽) perpendicular to the plane of precipitation at various irradiation temperatures: 1) 320-340°K (▽), 2) 820-920°K (▼, ▲); ---- indicates data for GMZ graphite at the temperatures indicated [1].

tallographic c axis) increases considerably even at a flux in excess of 10^{19} neutrons/cm² and does not stabilize but increases by a factor of 12 at a flux $>1.6 \cdot 10^{20}$ neutrons/cm². The $\Delta K/K$ values turn out to be smaller than those of reactor graphite irradiated at the same temperature.

At an irradiation temperature of 870-970°K, the thermal resistance of the pyrographite decreases and therefore $\Delta K/K = 1.5-2$ with a flux of $4 \cdot 10^{21}$ neutrons/cm². Also in this case the $\Delta K/K$ value of pyrographite is lower in the plane perpendicular to the direction of precipitation than in reactor graphite. In the direction which is parallel to the plane of precipitation, the $\Delta K/K$ values of pyrographite and GMZ graphite practically coincide. This confirms the previously established fact [2] that the relative change in the thermal conductivity does not depend upon the initial properties of the material irradiated.

Since at increasing temperatures the measurements of the thermal conductivity of nonirradiated graphite lead to lower values but those on irradiated graphite to higher values, we may assume that the thermal conductivity must be practically unchanged in the case of pyrolytic graphite irradiation at temperatures above 1200-1300°K [3].

After measuring the thermal conductivity of pyrolytic graphite samples irradiated at 870-970°K, the samples were used to estimate the specific electrical resistivity (see Table 1). Though owing to the small dimensions and the inhomogeneity of the samples the precision of the measurements was low, an increase in the electric resistivity of pyrolytic graphite can be clearly recognized in the direction which is parallel to the plane of precipitation. This increase substantially exceeds that observed in the case of GMZ graphite because the relative change in the electrical resistivity is inversely proportional to the absolute value of the electrical resistivity of the nonirradiated material [3]. In the direction perpendicular to the plane of precipitation and parallel to the crystallographic c axis, the $\Delta \rho / \rho$

values are negative and reach 0.5-1.1. This decrease in the electrical resistivity was explained in [4] by a partial closing of the Mrozovskii fissures.

LITERATURE CITED

1. Yu. S. Virgil'ev and I. A. Dmitriev, *At. Energ.*, **50**, No. 4, 281 (1980).
2. Yu. S. Virgil'ev et al., *At. Energ.*, **30**, No. 3, 311 (1971).
3. V. V. Goncharov et al., *The Effect of Irradiation upon the Graphite of Nuclear Reactors* [in Russian], Atomizdat, Moscow (1978).
4. Yu. S. Virgil'ev, R. N. Ivanova, and V. G. Makarchenko, in: *Construction Materials on the Basis of Graphite* [in Russian], No. 8, Metallurgiya, Moscow (1974), p. 95.

PRELIMINARY FILTERING OF THE RESULTS OF MEASUREMENTS PERFORMED IN EXPLORATORY GAMMA-LOGGING

I. M. Khaikovich and V. N. Popov

UDC 550.83:539.166.3:681.14

When using digital recordings of gamma logging (GL) data, the choice of the optimum step Δ_1 of depth quantization and the inclusion of the peculiarities of the procedure used to interpret the results of the measurements are important factors. We shall examine these problems from the point of view of increasing the accuracy of the solution of the inverse problem of GL. It is evident that with a small quantization step Δ_1 , which is used in measurements, the results of GL will be strongly affected by statistical fluctuations. Large values of Δ_1 will cause considerable distortion of the starting signal and, as a result, loss of detail in the solution of the inverse problem. As is well known [1], the optimum quantization step Δ for the inverse problem of GL (the "interpretation step") equals 10 cm. Let $J(x)$ be the measured signal. We obtain the following expression for the distribution of the density of elements along the axis of the well:

$$q(x) = \sum_{k=-N}^N B_k j(x + k\Delta), \quad (1)$$

where $j(x) = J(x)/K$; K is the scaling factor; B_k are coefficients determined by the construction of the well and the well instrumentation absorbing and scattering properties of the rock and of the flushing liquid. Here $\sum_{k=-N}^N B_k^2 > 1$ and the variance $q(x)$

$$\sigma_q^2 \leq \sum_{k=-N}^N B_k^2 \sigma_j^2 \quad (2)$$

increases by a factor of $\sum_{k=-N}^N B_k^2$ in comparison with the variance of the measured signal σ_j^2 .

To decrease the effect of noise and to increase the stability of the solution of the inverse problem of GL, the signal $J(x)$ must first be filtered. Since in GL the signal by its nature is discrete, it is natural to use for this purpose a linear discrete filter:

$$m(x) = \sum_{l=-M}^M b_l j(x + \Delta_1 l), \quad (3)$$

where $m(x)$ are the filtered values of the signal $J(x)$ and b_l are the coefficients of the filter.

Translated from *Atomnaya Energiya*, Vol. 56, No. 3, pp. 179-180, March, 1984. Original article submitted March 18, 1983.

Such a filter, as shown in [2], decreases the noise level by a factor of ϵ if its coefficients b_l are determined by the solution of the system of equations

$$\sum_{l=-M}^M b_l(j_l, j_n) + b_n \lambda = (j, j_n), \quad n=0, \pm 1, \dots, \pm M; \quad (4)$$

$$\sum_{l=-M}^M b_l^2 = \epsilon,$$

where

$$(j_l, j_n) = \int_{-\infty}^{\infty} j(x + l\Delta_1) j(x + n\Delta_1) dx,$$

and the parameter λ determines the deviation of $\sum_{l=-M}^M b_l$ from 1.

With a prefiltered signal, instead of expression (1), we obtain the following expression for the density distribution $Q(x)$

$$Q(x) = \sum_{k=-N}^N B_k^{(F)} m(x + k\Delta). \quad (5)$$

It follows from Eqs. (3) and (5) that in this case

$$\sigma_q^2 = \sum_{k=-N}^N (B_k^{(F)})^2 \sum_{l=-M}^M b_l^2 \sigma_j^2. \quad (6)$$

Thus, the quantity

$$B^2 = \sum_{k=-N}^N (B_k^{(F)})^2 \sum_{l=-M}^M b_l^2 \quad (7)$$

can serve as a criterion of the quality of the preliminary filtering of the signal, measured with a quantization step $\Delta_1 < \Delta = 10$ cm. Evidently, the smaller B^2 the more stable the inverse problem of logging will be. By changing the value of λ it is possible to find the solution of the system (4) for which B^2 in Eq. (7) will be minimum.

We shall demonstrate the advantage of the preliminary filtering of the measured signal using Eq. (3) over direct averaging with a quantization step of 10 cm. The values of b_l ($l = 0, 1, 2, \dots, 7$) obtained as indicated, as a result of solving the system (4) for the gamma-anomaly over an ore stratum with a thickness of 10 cm with $\Delta_1 = 2.5$ cm, rock density $\rho = 3$ g/cm³, and well diameter 6 cm equals 0.3371; 0.2689; 0.1197; -0.0058; -0.0474; -0.0232; 0.0078; 0.0114. The value of B^2 in expression (7) for the optimum filter ($B_{\text{opt.f}}^2$) constitutes

1.99 $\left[\sum_{l=-7}^7 b_l^2 = 0.3; \sum_{k=-7}^7 (B_k^{(F)})^2 = 6.79 \right]$. For a filter with a square-shaped characteristic at four

points for which $b_{-2} = b_{-1} = b_0 = b_1 = 0.25 B^2 (B_{\text{st}}^2)$ in expression (7) equals 3.1 $\left[\sum_{l=-2}^2 b_l^2 = 0.25; \sum_{k=-7}^7 (B_k^{(F)})^2 = 12.4 \right]$, i.e., $B_{\text{pf}}^2 / B_{\text{opt.f}}^2 = 1.55$. Calculations with a step of $\Delta_1 = 2.5$ cm show that

when the diameter of the well changes from 6 to 20 cm and the density changes from 1.5 to 3 g/cm³, the ratio $B_{\text{pf}}^2 / B_{\text{opt.f}}^2$ changes by a factor of from 1.5 to 1.8.

Thus the use of optimum filtering with a step size $\Delta_1 = 2.5$ cm decreases the variance of the density $Q(x)$ sought compared with the use of a moving average filter almost by a factor of two, which is also confirmed by data from mathematical modeling. At the same time, as Δ_1 increases up to 5 cm filtering according to Eq. (3) provides practically no advantage.

Aside from the decrease in the average error of the results of interpretation, recording GL data with a step size $\Delta_1 = 2.5$ cm and subsequent optimum filtering permits greatly increasing the accuracy of the interpretation of the ore intervals of small thickness due to the more accurate analysis of the results of measurements. Based on the filtered gamma field, sections are separated out between neighboring minima. The "scaling" is done through

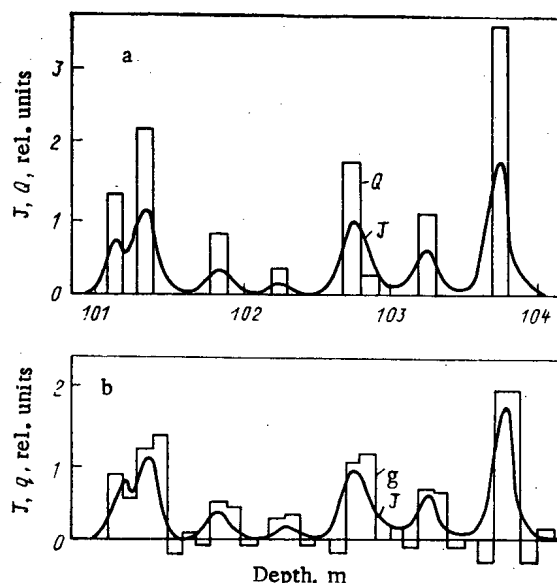


Fig. 1. Results of interpretation of the starting density distribution of radioactive elements 1.3; 2.2; 0.8; 0.4; 1.8; 0.35; 1.1; 3.5 in accordance with the depth of local extrema according to the filtered signal (a) and with a displacement of the "scaling" by $\Delta/2$ from local peaks in the gamma field (b).

the local maximum of each section retaining within each section a quantization step of 10 cm, i.e., in the algorithm (5) the values $m(x_i)$ with a step Δ are used so that one of them coincides with the local maximum of the anomaly of the gamma field in each section. The results of the interpretation according to separate sections are combined. The displacement of the "scaling" within the limits of 10 cm practically does not distort the value of the linear reserve (metropercent).

Experience in using the program realizing the filtering algorithm (3) and the combination of results of the interpretation based on separate sections indicates that this method excludes errors introduced by the variation of the initial position of the well instrumentation, and also decreases by more than an order of magnitude the absolute values of the "negative" contents, arising near the boundaries of the ore body and the enclosing rock. Figure 1 shows an example of the work based on the program realizing optimal filtering and the interpretation with respect to sections between the neighboring minima as well as using the program realizing the algorithm (1), with random "scaling" of the gamma anomaly (not in terms of the local maximum).

The results presented show the undoubted advantage of encoding the GL with a step less by an integer number of times than the quantization step used in the interpretation (10 cm). In addition, a considerable gain is achieved for $\Delta/\Delta_1 \geq 4$. The use of a quantization step $\Delta_1 < 2.5$ cm is not expedient due to the increase in volume of recorded information and due to the difficulty of ensuring adequate accuracy of measurement of small quantization steps.

LITERATURE CITED

1. I. M. Khaikovich and V. N. Yakovlev, *Metody Rudnoi Geofiziki*, No. 11, 87 (1975).
2. I. M. Khaikovich, *Fizika Zemli*, No. 1, 65 (1972).

CALIBRATION OF INDIVIDUAL DOSIMETERS BY THE ABSORBED DOSE OF PHOTON RADIATION

Yu. P. Bakulin, V. P. Bashmakov, E. A. Bogdanov,
T. I. Gimadova, N. I. Muratov, and A. V. Tultaev

UDC 539.1.08

At the present time, in order to obtain an indirect indication of a radiation dose received by personnel, individual dosimeters calibrated in units of the exposure dose are used. The error in these estimates does not satisfy the requirements on the accuracy of measurements of the absorbed dose. It is well known that error in measurement of the absorbed dose by an individual dosimeter at the depth of the maximum or average value of the absorbed dose as well as in some organ of the human body is determined by the calibration error, the class of the apparatus, the dependence of its sensitivity on the energy of the radiation and other parameters. For dosimeters used simultaneously to measure small and large doses of radiation (for example, during gamma therapy or for estimating the ionizing action on personnel in accidents) with doses exceeding 50 rad (1 rad = 0.01 Gy), the error of the measurements must not exceed 10% [1]. This requirement is dictated by the nature of radiation change in tissues, organs, and in the entire human organism [2].

In [3] a method is proposed for calibrating individual dosimeters in units of the absorbed dose. The essence of the method (Fig. 1) is as follows: The individual dosimeter being calibrated is placed on the front surface of a standard tissue-equivalent phantom in a field of a collimated beam of monodirectional and gamma radiation from ^{60}Co . The indications on the dosimeter being calibrated are assigned the value of the absorbed dose measured by a standard dosimeter with a miniature ionization chamber placed at a depth in the phantom where the absorbed dose is maximum.

The proposed method suffers from a significant drawback which has not previously been noted. The absorbed dose in the organ of interest can be measured with the indicated error if the distribution of the dose in the body of the individual is known and if the position of the individual, dosimeter, and source of radiation corresponds exactly to the conditions of calibration (see Fig. 1). In this case, we can talk about a single-valued relation between the indications of the dosimeter and the distribution of the dose in the body. In any other position of the body relative to the direction of radiation propagation, when the dosimeter falls in the "shade" of the radiation (Fig. 2), the uniqueness of the relation between the indications of the dosimeter and the distribution of dosage in the body breaks down, which leads to the appearance of the neglected systematic error in determining the absorbed dose.

The uncertainty, which destroys the uniqueness of the dosage distribution and of the indications of the dosimeter, arises, in particular, due to the barrier effect, which is manifest as a jumplike change in the absorbed dose on the "shaded" surface of the irradiated object. Taking this into account, we compared the indications of different types of individual dosimeters and of a standard VA-J-18 dosimeter (placed on the front and "shaded" surfaces of the tissue-equivalent phantom). We used a VA-J-18 dosimeter with a miniature thimble chamber, whose inner and outer diameters were 6 and 3 mm, respectively. We determined the metrological characteristics with comparative measurements of the absorbed dose with a dosimeter and a standard calorimeter in graphite and tissue-equivalent phantoms. The dependence of the ratios of the indications of the calorimeter and of the VA-J-18 dosimeter on the depth of the phantom irradiated by monodirected radiation from ^{60}Co remains constant to within 3%. The error of the calibration of the chamber according to the calorimeter does not exceed 5% [4].

The indications of the different individual dosimeters were compared with the standard VA-J-18 dosimeter according to the scheme in Fig. 1. We placed individual dosimeters on the front surface of the irradiated muscle tissue-equivalent phantom with dimensions $30 \times 30 \times 20$ cm. The center of the chamber of the standard dosimeter placed in the cavity of the phantom was displaced from its surface by 5 mm. We measured the absorbed dose in fields of radi-

Translated from *Atomnaya Énergiya*, Vol. 56, No. 3, pp. 180-181, March, 1984. Original article submitted June 6, 1983.

TABLE 1. Ratio of Indications of Individuals and Standard Dosimeters on the "Shaded" Surface of the Phantom

Effective energy, keV	Computed values	Type of dosimeter				
		VA-J-18	ID-4	IKS-A	Harshaw (USA, LiF)	(LiF)
^{60}Co ($\sim 1\text{ MeV}$)	0,84 [6,7]	0,85	0,86	0,84	0,85	0,83
^{137}Cs ($\sim 0,5\text{ MeV}$)	0,79 [6,7]	—	—	—	—	—
120	—	0,67	0,65	0,65	0,69	0,70
100	0,60 [7,8]	0,68	0,65	0,63	0,65	0,69
82	—	0,68	0,62	0,60	0,67	0,70
50	—	0,65	0,56	0,58	0,61	0,71
41	—	0,66	—	—	0,70	0,76

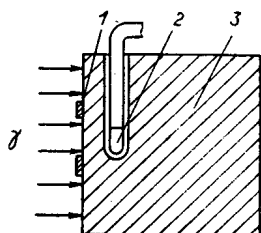


Fig. 1

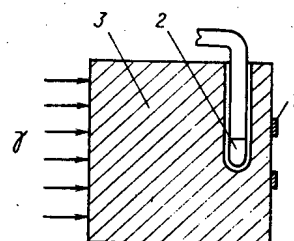


Fig. 2

Fig. 1. Scheme for calibrating individual dosimeters on the front surface of a phantom: 1) individual dosimeter; 2) ionization chamber of standard dosimeter; 3) tissue-equivalent phantom.

Fig. 2. Scheme of comparative measurements of the dose absorbed by individual dosimeters and the standard dosimeter on the "shaded" surface of the phantom: 1) individual dosimeter; 2) ionization chamber of the standard dosimeter; 3) tissue-equivalent phantom.

ation from ^{60}Co and x-ray radiation from the RUM-17 apparatus with different filters and voltages on the tube.

Next, we measured the absorbed dose on the "shaded" surface of the phantom (see Fig. 2). The energy characteristics of the photon radiation were the same as in the first experiment. The thickness of the phantom varied, but constituted not less than two mean free photon path lengths. The ratio of the indications of individual and standard dosimeters remained constant with the indicated thickness of the phantom. The results of the measurements are presented in Table 1. For comparison, the third column shows the ratios of the indications of the standard chamber on the surface of the phantom and inside it. The ratio of the indications of the individual and standard dosimeters with measurements on the front surface of the phantom are adopted as the basic unit. The table also shows the computed values of the coefficients corrected for the barrier effect, obtained starting from the accumulation factor for an infinite or semiinfinite and barrier geometry [5-8].

Comparative control measurements of the dose absorbed by the standard and individual dosimeters in the free (without a phantom) geometry with attachments ensuring electronic equilibrium, taking into account normalization, showed identical dosage values.

The data obtained lead to the following conclusion.

There is a sharp decrease of the absorbed dose on the "shaded" surface of the irradiated phantom (on the side from which the incident radiation exists), confirming the barrier effect and destroying the uniqueness of the dependence of the dosage distribution over the depth of the phantom and the indications of dosimeters with different dependences of the sensitivity on the energy of the radiation.

Taking into account the wide range of the energy spectrum of radiation sources, as well as the uncertainty in the mutual position of the body with individual dosimeters and the direction of propagation of the radiation, the values of the dose absorbed by the body, measured by dosimeters calibrated according to the method proposed in [3], will be systematically underestimated by more than 20-30%.

LITERATURE CITED

1. A. I. Ruderman et al., Remote Gamma Therapy of Malignant Tumors [in Russian], Meditsina, Moscow (1977).
2. S. P. Yarmolenko, Radiobiology of Man and Animals [in Russian], Vysshaya Shkola, Moscow (1977).
3. Yu. I. Bregadze, "Creation and investigation of a complex of standard installations for metrological support of measurements of absorbed and equivalent doses of gamma radiation and fast neutrons," Doctoral Dissertation, VNIIFTRI, Moscow (1978).
4. A. V. Tultaev, "Creation and investigation of standard means for measuring the intensity of the absorbed dose of photon ionizing radiation in muscle-tissue-equivalent material," Candidate's Dissertation, VNIIFTRI, Moscow (1974).
5. M. Berger and J. Dogget, U.S. Res. Nat. Bur. Standards, **56**, 89 (1956).
6. L. R. Kimel', in: Problems of Dosimetry and Radiation Shielding [in Russian], No. 3, Atomizdat, Moscow (1964), p. 16.
7. L. R. Kimel' and V. P. Mashkovich, Protection from Ionizing Radiation [in Russian], Atomizdat, Moscow (1972), p. 94.
8. A. M. Panchenko et al., in: Problems of Dosimetry and Radiation Shielding [in Russian], No. 13, Atomizdat, Moscow (1973), p. 32.

COMPARATIVE INVESTIGATION OF THE PROCESS OF DEFECT FORMATION IN SiO₂ UNDER GAMMA AND GAMMA-NEUTRON IRRADIATION

I. Kh. Abdukadyrova

UDC 666.192:535.342

Earlier [1] we began investigation of the processes of radiation-induced defect formation which occur in SiO₂ with a view to refining and extending the dosimetric capabilities of this material. To solve the problem of reactor dosimetry and to determine the influence of impurities and the form of radiation on the rate at which plates are colored, we chose to investigate two grades of fused SiO₂ (KSG and KI) subjected to the action of ⁶⁰Co γ rays and γ-neutron radiation from a VVR-SM reactor.

Before and after irradiation of the SiO₂ we took the spectra of optical absorption in the ultraviolet region of the spectrum at a wavelength $\lambda = 200-300$ nm. The variation of the reduced optical density $\Delta J/d$ of the KSG plates for $\lambda = 215$ nm after large doses of γ rays ($10^3 < D_\gamma < 2 \cdot 10^8$ Gy) is shown in Fig. 1a. It is seen that in the range $D_\gamma \leq 0.5$ MGy the transparency of the plates changes only slightly. The transparency is observed to decrease appreciably when $D_\gamma \leq 3$ MGy and the specimen is decolorized when $D_\gamma = 100$ MGy. This experiment showed that the rate of defect formation, responsible for absorption at 215 nm, varies with the radiation dose. The dose dependence of the absorption for KI at $\lambda = 215$ nm is characterized by the proportional growth of J up to $D_\gamma = 3$ MGy, after which a tendency for the rate of the process to decrease is observed. Comparison of the $J_{215}(D_\gamma)$ curves shows them not to be identical and to have a kink at a dose of ~ 3 MGy.

The corresponding irradiation of KSG specimens in the core of the VVR-SM reactor led to a substantial decrease in the transparency of the plates at $\lambda \approx 215$ nm. As follows from Fig. 1a (curve 2) at comparatively low doses of γ rays (1 kGy-0.5 MGy) the change in the transparency of the SiO₂ specimen is scarcely noticeable and when $D_\gamma \geq 0.5$ MGy a sharp increase is observed in the optical density of the 215 nm absorption band and this continues up to the maximum dose without a decrease in the rate of generation and without any appreciable

Translated from Atomnaya Énergiya, Vol. 56, No. 3, pp. 182-183, March, 1984. Original article submitted July 21, 1983.

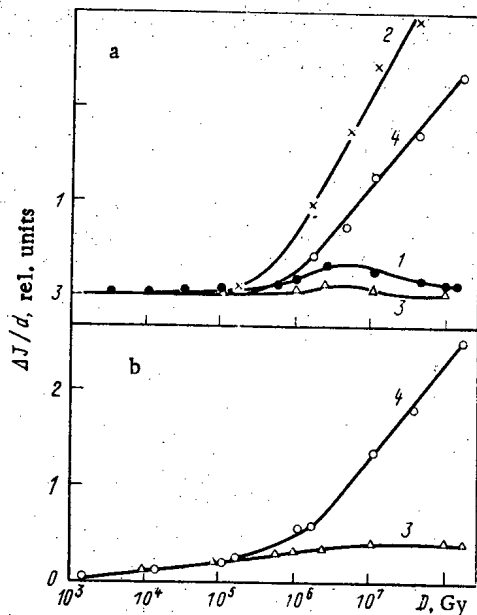


Fig. 1

Fig. 1. Dose dependence of the relative change in the intensity of the absorption bands 215 nm (1, 2) and 245 nm (3, 4) under γ -ray (1, 3) and γ -neutron (2, 4) irradiation of KSG (a) and KI (b) specimens.

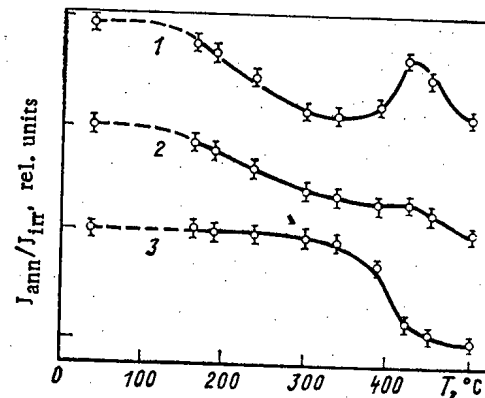


Fig. 2

Fig. 2. Kinetic curves of thermal decoloring of the induced color of fused SiO_2 for $\lambda = 215$ nm (1), 245 nm (2), and 540 nm (3).

saturation. Comparison of the functions $J_{215}^{\text{KSG}}(D_{n,\gamma})$ shows that they are similar and consist of two almost rectilinear segments of curves, whose point of intersection corresponds to a value of 0.1-0.5 MGy. This permits the conclusion that the location of the critical point found does not depend on the presence or absence of a substantial impurity concentration and is due to the onset of the radiation-stimulated formation of defects in the fused SiO_2 . At the same time, the change in the function $J_{215}^{\text{KSG}}(D_{n,\gamma})$ can be explained if it is assumed that additional traps are formed in KSG in the range of doses higher than 0.1 MGy, which is in agreement with the opinion of Boganov et al. [2].

Similar dose dependences were obtained for the second ultraviolet absorption band with $\lambda = 245$ nm. From Fig. 1a (curves 3, 4) it follows that the increase in the optical density of the KSG specimens under the effect of γ rays and reactor radiations has the same tendency as for $\lambda = 215$ nm (see Fig. 1a, curves 1, 2). On the other hand, the shape of the curves of the functions $J_{245}^{\text{KI}}(D_{n,\gamma})$ and $J_{245}^{\text{KSG}}(D_{n,\gamma})$ (see Fig. 1b, curves 3, 4) reproduces the curves obtained earlier for KI specimens for $\lambda = 215$ nm. This correlation of the processes of the radiation kinetics in different forms of SiO_2 (pure and with impurities) indicates the intrinsic nature of the color centers as well as the possibility of their being related. To make this hypothesis more exact and to explain the stability of point defects under external actions, we examined the thermal decoloring of the irradiated specimens as well as the influence of different factors on the intensity of the bands of additional absorption.

The irradiated KI specimens ($D_{\gamma} = 10$ kGy) were heated in stages at $40 < T < 600^\circ\text{C}$ with intermediate measurements of the absorption spectra in the ultraviolet and visible regions. The induced absorption for $\lambda = 215$ nm (Fig. 2, curve 1) begins to weaken markedly at 200°C . Two main stages of annealing were established and an antiannealing stage was observed between them. To ascertain the cause of the kinetics of the 215-nm peak we made a comparison with the thermal stability of the other absorption bands. It turned out that the shape of $J(T_{\text{ann}})$ of the absorption bands is specific. The 245 nm band, for example, is secured in two stages without evident deviations (Fig. 2, curve 2). It is of greatest interest to compare $J_{\text{ann}}^{215}/J_{\text{irr}}^{215}(T_{\text{ann}})$ and $J_{\text{ann}}^{540}/J_{\text{irr}}^{540}(T_{\text{ann}})$ (Fig. 2, curves 1, 3). It is seen that the segment of the curve 3 in the range $360 < T_{\text{ann}} < 430^\circ\text{C}$, which is characteristic of the main stage of intense decoloring of visible color, is a reflection, as it were, of the anomaly of the ultraviolet band. It must be pointed out that intense decoloring of the 215 nm and 245 nm bands in the first stage of the annealing and the 540 nm band in the final stage is observed at 250 and

TABLE 1. Influence of Experimental Conditions on Stability of Optical Density of KSG Specimen from Results of Measurements of the Light Intensity J for $\lambda = 215$ nm and Dose of 1 MGy

P^*	J_1	T, h	J_2	τ, h	J_3	A_4	J_4
Reactor radiation							
$4,0 \cdot 10^{12}$	0,76	360	0,78	0,1	0,78	1	0,76
$8,0 \cdot 10^{12}$	0,80	600	0,74	0,2	0,78	2	0,76
$1,2 \cdot 10^{13}$	0,78	1200	0,80	0,3	0,76	3	0,79
$1,6 \cdot 10^{13}$	0,76	2160	0,78	0,5	0,70	4	0,80
$4,0 \cdot 10^{13}$	0,74	4320	0,74	0,6	0,68	5	0,77
Average	0,768		0,768		0,740		0,776
Error, %	2,3		2,4		3,2		1,6
γ rays							
$5,2 \cdot 10^{-3}$	0,20	24	0,18	0,1	0,21	1	0,21
$2,1 \cdot 10^{-2}$	0,19	48	0,18	0,2	0,20	2	0,20
$2,6 \cdot 10^{-1}$	0,22	720	0,21	0,3	0,18	3	0,18
$7,7 \cdot 10^{-1}$	0,18	1080	0,19	0,5	0,17	4	0,21
$1,0 \cdot 10^0$	0,16	1440	0,20	0,6	0,16	5	0,19
Average	0,190		0,192		0,184		0,200
Error, %	2,4		0,8		1,6		1,5

*The values of P for reactor radiation are given in neutrons/cm²•sec while for γ rays they are in C/kg•sec.

370–430°C, respectively, i.e., at a temperature which is close to the known maxima of the thermoluminescence [2, 3]. This indicates the probable interrelationship of the defects which are responsible for the given peaks and are determined by the presence, for example, of oxygen vacancies or impurity ions. Moreover, it is possible for a center, which absorbs in the 540 nm band, to be transformed into a center which is responsible for absorption at $\lambda = 215$ nm. This indicates that they are closely bound and that the center of the 245 nm band is somewhat independent, and also supports the assumption made in [4] for SiO₂ irradiated in a reactor. If we proceed from the well known [5] model of a center for $\lambda = 215$ nm (an electron localized on the sp^3 orbital of silicon) and 540 nm (an electron trapped by a bridge oxygen vacancy neighboring on an Al³⁺ ion), then conversion is possible at a high temperature, for example, because of electron (impurity) migration.

According to the shape obtained for the $J(T_{ann})$ curves, thermal destruction of the induced color in the ultraviolet region of the spectrum is barely noticeable at a temperature below 180°C and reaches a maximum at approximately 500°C which demonstrates the possibility of multiple dosimetric use of an SiO₂ specimen. The revealed radiation kinetics of the 215 nm and 245 nm bands indicates that as SiO₂ is irradiated the number of oxygen vacancies, which obviously are responsible for the absorption sought, changes at a rate which is determined by the efficiency of displacement of oxygen ions from the lattice sites with the formation of point defects and entrapment of carriers in formed or existing traps. The intensive growth of displaced oxygen atoms begins at a γ -neutron radiation dose of ~ 0.1 – 0.5 MGy and can serve as a measure of the effect of reactor radiation.

The values of reduced optical density $\Delta J/d$ for KSG plates under different irradiation conditions and storage are given in Table 1. The results show that the indications of the system have a low sensitivity to the dose rate P , the holding time T , and the optical illumination τ , and also shows that A_4 is fairly well reproducible (error of no more than 5%). All of this confirms the practicality of building a solid-state dosimeter based on fused SiO₂ for measuring mixed reactor radiation and its separate components. For selective recording of neutron radiation it is preferable to use microplates of KSG which is distinguished by a high degree of purity, and to employ the wavelengths $\lambda = 215$ and 245 nm.

LITERATURE CITED

1. I. Kh. Abdukadyrova, At. Energ., 51, No. 1, 65 (1981).

2. A. G. Boganov et al., in: Radiation-Stimulated Effects in Oxygen-Containing Crystals and Glasses [in Russian], Branch of the Academy of Sciences of the USSR, Tashkent (1978), p. 263.
3. V. V. Zhakhov et al., in: New Inorganic Materials and Coatings Based on Glass and Refractory Compounds [in Russian], Moscow (1973), p. 96.
4. G. Mayer and J. Gueron, Glass Ind., 34, 127 (1952).
5. G. V. Biorganovskaya et al., Effect of Radiation on Inorganic Glasses [in Russian], Atomizdat, Moscow (1968), p. 244.

MEASUREMENT TECHNIQUES*Izmeritel'naya Tekhnika*

Vol. 27, 1984 (12 issues) \$520

MECHANICS OF COMPOSITE MATERIALS*Mekhanika Kompozitnykh Materialov*

Vol. 20, 1984 (6 issues) \$430

METAL SCIENCE AND HEAT TREATMENT*Metallovedenie i Termicheskaya Obrabotka Metallov*

Vol. 26, 1984 (12 issues) \$540

METALLURGIST*Metallurg*

Vol. 28, 1984 (12 issues) \$555

PROBLEMS OF INFORMATION TRANSMISSION*Problemy Peredachi Informatsii*

Vol. 20, 1984 (4 issues) \$420

PROGRAMMING AND COMPUTER SOFTWARE*Programmirovaniye*

Vol. 10, 1984 (6 issues) \$175

PROTECTION OF METALS*Zashchita Metallov*

Vol. 20, 1984 (6 issues) \$480

RADIOPHYSICS AND QUANTUM ELECTRONICS*Izvestiya Vysshikh Uchebnykh Zavedenii, Radiofizika*

Vol. 27, 1984 (12 issues) \$520

REFRACTORIES*Ogneupory*

Vol. 25, 1984 (12 issues) \$480

SIBERIAN MATHEMATICAL JOURNAL*Sibirskii Matematicheskii Zhurnal*

Vol. 25, 1984 (6 issues) \$625

**SOIL MECHANICS AND
FOUNDATION ENGINEERING***Osnovaniya, Fundamenty i Mekhanika Gruntov*

Vol. 21, 1984 (6 issues) \$500

SOLAR SYSTEM RESEARCH*Astronomicheskii Vestnik*

Vol. 18, 1984 (6 issues) \$365

SOVIET APPLIED MECHANICS*Prikladnaya Mekhanika*

Vol. 20, 1984 (12 issues) \$520

SOVIET ATOMIC ENERGY*Atomnaya Energiya*

Vols. 56-57, 1984 (12 issues) \$560

**SOVIET JOURNAL OF GLASS PHYSICS
AND CHEMISTRY***Fizika i Khimiya Stekla*

Vol. 10, 1984 (6 issues) \$235

**SOVIET JOURNAL OF
NONDESTRUCTIVE TESTING***Defektoskopiya*

Vol. 20, 1984 (12 issues) \$615

SOVIET MATERIALS SCIENCE*Fiziko-khimicheskaya Mekhanika Materialov*

Vol. 20, 1984 (6 issues) \$445

SOVIET MICROELECTRONICS*Mikroelektronika*

Vol. 13, 1984 (6 issues) \$255

SOVIET MINING SCIENCE*Fiziko-tekhnicheskie Problemy Razrabotki**Poleznykh Iskopaemykh*

Vol. 20, 1984 (6 issues) \$540

SOVIET PHYSICS JOURNAL*Izvestiya Vysshikh Uchebnykh Zavedenii, Fizika*

Vol. 27, 1984 (12 issues) \$520

**SOVIET POWDER METALLURGY AND
METAL CERAMICS***Poroshkovaya Metallurgiya*

Vol. 23, 1984 (12 issues) \$555

STRENGTH OF MATERIALS*Problemy Prochnosti*

Vol. 16, 1984 (12 issues) \$625

THEORETICAL AND MATHEMATICAL PHYSICS*Teoreticheskaya i Matematicheskaya Fizika*

Vol. 58-61, 1984 (12 issues) \$500

UKRAINIAN MATHEMATICAL JOURNAL*Ukrainskii Matematicheskii Zhurnal*

Vol. 36, 1984 (6 issues) \$500

Send for Your Free Examination Copy**Plenum Publishing Corporation, 233 Spring St., New York, N.Y. 10013****In United Kingdom: 88/90 Middlesex St., London E1 7EZ, England**

Prices slightly higher outside the U.S. Prices subject to change without notice.

RUSSIAN JOURNALS IN THE PHYSICAL AND MATHEMATICAL SCIENCES

AVAILABLE IN ENGLISH TRANSLATION

ALGEBRA AND LOGIC

Algebra i Logika

Vol. 23, 1984 (6 issues) \$360

ASTROPHYSICS

Astrofizika

Vol. 20, 1984 (4 issues) \$420

AUTOMATION AND REMOTE CONTROL

Avtomatika i Telemekhanika

Vol. 45, 1984 (24 issues) \$625

COMBUSTION, EXPLOSION, AND SHOCK WAVES

Fizika Goreniya i Vzryva

Vol. 20, 1984 (6 issues) \$445

COSMIC RESEARCH

Kosmicheskie Issledovaniya

Vol. 22, 1984 (6 issues) \$545

CYBERNETICS

Kibernetika

Vol. 20, 1984 (6 issues) \$445

DIFFERENTIAL EQUATIONS

Differentsial'nye Uravneniya

Vol. 20, 1984 (12 issues) \$505

DOKLADY BIOPHYSICS

Doklady Akademii Nauk SSSR

Vols. 274-279, 1984 (2 issues) \$145

FLUID DYNAMICS

Izvestiya Akademii Nauk SSSR,

Mekhanika Zhidkosti i Gaza

Vol. 19, 1984 (6 issues) \$500

FUNCTIONAL ANALYSIS AND ITS APPLICATIONS

Funktsional'nyi Analiz i Ego Prilozheniya

Vol. 18, 1984 (4 issues) \$410

GLASS AND CERAMICS

Steklo i Keramika

Vol. 41, 1984 (6 issues) \$590

HIGH TEMPERATURE

Teplofizika Vysokikh Temperatur

Vol. 22, 1984 (6 issues) \$520

HYDROTECHNICAL CONSTRUCTION

Gidrotekhnicheskoe Stroitel'stvo

Vol. 18, 1984 (12 issues) \$385

INDUSTRIAL LABORATORY

Zavodskaya Laboratoriya

Vol. 50, 1984 (12 issues) \$520

INSTRUMENTS AND EXPERIMENTAL TECHNIQUES

Pribory i Tekhnika Eksperimenta

Vol. 27, 1984 (12 issues) \$590

JOURNAL OF APPLIED MECHANICS AND TECHNICAL PHYSICS

Zhurnal Prikladnoi Mekhaniki i Tekhnicheskoi Fiziki

Vol. 25, 1984 (6 issues) \$540

JOURNAL OF APPLIED SPECTROSCOPY

Zhurnal Prikladnoi Spektroskopii

Vols. 40-41, 1984 (12 issues) \$540

JOURNAL OF ENGINEERING PHYSICS

Inzhenerno-fizicheskii Zhurnal

Vols. 46-47, 1984 (12 issues) \$540

JOURNAL OF SOVIET LASER RESEARCH

A translation of articles based on the best Soviet research in the field of lasers

Vol. 5, 1984 (6 issues) \$180

JOURNAL OF SOVIET MATHEMATICS

A translation of Itogi Nauki i Tekhniki and Zapiski

Nauchnykh Seminarov Leningradskogo Otdeleniya

Matematicheskogo Instituta im. V. A. Steklova AN SSSR

Vols. 24-27, 1984 (24 issues) \$1035

LITHOLOGY AND MINERAL RESOURCES

Litologiya i Poleznye Iskopaemye

Vol. 19, 1984 (6 issues) \$540

LITHUANIAN MATHEMATICAL JOURNAL

Litovskii Matematicheskii Sbornik

Vol. 24, 1984 (4 issues) \$255

MAGNETOHYDRODYNAMICS

Magnitnaya Gidrodinamika

Vol. 20, 1984 (4 issues) \$415

MATHEMATICAL NOTES

Matematicheskie Zametki

Vols. 35-36, 1984 (12 issues) \$520

continued on inside back cover